

**Joint Atmospheric-Terrestrial Water Balance for the Tana
River Basin of Kenya, East Africa by Coupled Atmospheric-
Hydrological Modeling**

Dissertation
der Fakultät für Angewandte Informatik
Institut für Geographie
der Universität Augsburg
zur Erlangung des Grades eines Doktors
der Naturwissenschaften
(Dr. rer. nat.)

vorgelegt von

Noah Misati Kerandi

M. Tech Meteorology

Augsburg, 2017

Erstgutachter: Prof. Dr. Harald Kunstmann

Zweitgutachter: PD Dr. Andreas Philipp

Tag der mündlichen Prüfung: 30. November 2017

Acknowledgements

To God be the glory, this far you have brought me. Thank you, Lord.

I am full of appreciation and gratitude for a wide range of support, encouragement and prayers from many people towards the completion of this work.

My special thanks to Prof. Dr. Harald Kunstmann for proposing the topic, his candid supervision, advice and support. I also thank PD Dr. Andreas Philipp and PD Dr. Christoph Beck for their interest in this research and for being the second and third referees respectively of my thesis.

I admire the enthusiasm, consistency and advice from Dr. Patrick Laux and Dr. Joel Arnault all through this work. I thank Dr. Arnault for supplying the program for computation of the atmospheric water balance. I am obliged for technical advice from Drs. Sven Wagner, Benjamin Fersch, Heinzeller Dominikus, Gerhard Smiatek, Messrs. Johannes Werhahn and Thomas Rummler in regard to ideas and technicalities in WRF and WRF-Hydro modeling systems. I am thankful to Dr. Benjamin Fersch for encouraging me to work with the R-programming language.

I thank all my student colleagues: Drs. Moussa Waongo, Lorenz Christof and Ganquan Mao, Dang Thinh, Deng Diarra, Brosy Caroline, Cornelia Klein, Mohsen Soltan, Zhenyu Zhang, Cornelius Hald and other students from other groups in KIT/IMK-IFU, Campus Alpin for a very cordial cooperation and motivation in our struggle to make it. Thank you Thinh, Diarra, and Mohsen for all the fun jokes in our lunch breaks for it made a change from lonely time with the computers.

I sincerely thank my daughters Everlyne, Daisy and Miriam for braving my chronic absence from home, my brother Elkanah for fathering my daughters, Hellen for house-keeping and nursing my daughters, my family and mother for their prayers and unceasing support.

This work was funded by the German Academic Exchange Service (DAAD) and the national Commission for Science, Technology and Innovation (NACOSTI) on behalf of the Government of Kenya. In the same regard, I recognize the South Eastern Kenya University for granting me the study leave for this work.

Acknowledgement

Additionally, I am grateful for the following institutions for their input: The Kenya Meteorological Department (KMD), the Water Resource Management Authority (WARMA) of Kenya, the Leibniz Supercomputing Centre (LRZ), the Garmisch-Partekirchen SDA Church and the Adventist Review/Adventist World.

Finally, I am happy for the non-academic staff from the IT and Mechatronics, library, cleaning and security, many of who I only know their appearances but not their names, who made my life meaningful in my stay in the institute.

Abstract

The Tana River basin (TRB) is both vulnerable and prone to hydrological extremes of floods and droughts. Yet, the TRB is an extensive agricultural area that also contributes to more than half of Kenya's hydropower production. The basin is thus a contributor to the population's food security in this region and to Kenya's economy in general. This calls for proper understanding of the basin's hydrometeorology as a means of managing and mitigating the impacts of the extremes mentioned above. This PhD study contributes to a qualified and improved knowledge of the basin's atmospheric-terrestrial water balance. This is achieved through the application of the regional climate model Weather Research and Forecasting (WRF) and the coupled WRF-Hydro modeling system to this area.

The WRF model's ability to reproduce the 4-year (2011-2014) precipitation and temperature basin's climatology is analysed. The simulation results are compared with *Tropical Rainfall Measuring Mission* (TRMM), *Climate Hazards Group Infrared Precipitation with Station* data (CHIRPS), *Climate Research Unit* (CRU), *Global Land Evaporation Amsterdam Model* (GLEAM) and station data. Further, the uncoupled WRF-Hydro model is calibrated in order to identify a set of parameters in which it can mimic the hydroclimatology of the upper TRB. The calibration is based on stream flow data from the Tana Rukanga's river gauge station (RGS) 4BE10 at the outlet of the delineated Mathioya-Sagana subcatchment (3279 km²).

The WRF's model ability to reproduce the TRB's 4-year precipitation and temperature climatology is investigated in two stages: the identification of suitable configuration of set of parameterizations and the better configuration based on the impact of two different land use classifications i.e., the Moderate Resolution Imaging Spectroradiometer (MODIS) and the U.S Geological Survey (USGS) at two horizontal resolutions (50 km and 25 km). The parameterizations investigated are three cumulus convection schemes: Kain-Fritsch (KF), Grell Freitas (GF) and Bett Miller Janjic (BMJ); two microphysics schemes: WRF Single Moment 6-class (WSM6) and Lin *et al.* (LIN) while other schemes are uniform for all the 6 configurations. The KF, WMS6, ACM2 (KWA) configuration provides more reasonable results in simulating the seasonal and annual amounts of precipitation. In case of temperature all the considered six configurations simulate similar results with a cold bias compared to both station and CRU temperature. The land-use impact-based experiments show that all WRF simulations capture

well the annual as well as the interannual and spatial distribution of precipitation in the TRB according to station data and the TRMM estimates. The results show that by increasing the horizontal resolution of the WRF model from 50 km to 25 km, together with the use of the MODIS land use classification, a significant improvement in the precipitation results can be achieved. However, in the case of temperature, there is no discernible difference between the various experiments. In general, the WRF model reproduces reasonably the spatial patterns and seasonal cycle with a systematic cold bias with respect to both station and CRU data. The results from this study thus contribute to the identification of suitable and regionally adapted regional climate models (RCMs) for East Africa.

The WRF and coupled WRF-Hydro simulations focusing on the Mathioya-Sagana subcatchment at 5 km horizontal resolution show good results in terms of precipitation, streamflow and evapotranspiration ET. The simulated precipitation is slightly closer to that derived from CHIRPS than TRMM. For ET, the WRF and coupled WRF-Hydro captures the temporal evolution of GLEAM dataset, although with some underestimation. The coupled WRF-Hydro accumulated discharge (323 mm/yr) is very close to that of observed discharge (333 mm/yr), however with a low but acceptable Nash-Sutcliffe efficiency (NSE) equal to 0.02 and a good ratio of the root mean-square error to the standard deviation of measured data (RSR) of 0.99 at daily time step.

Finally, a method is developed to investigate the joint atmospheric-terrestrial water balance of the Mathioya-Sagana subcatchment based on the WRF and WRF-Hydro simulations. The analysis shows that the coupled WRF-Hydro slightly reduces precipitation, evapotranspiration and the soil water storage, but increases runoff, as compared to WRF. The precipitation recycling and efficiency measures between WRF and coupled WRF-Hydro are very close and comparatively small. This suggests that most of the precipitation in the region comes from moisture advection from the outside of the analysis domain, so that potential land-precipitation feedback mechanisms may have only small impacts in this region.

Zusammenfassung

Das Einzugsgebiet des Flusses Tana (TRB, *Tana River Basin*) ist stark durch hydrometeorologische Extremereignissen wie Fluten und Dürren gefährdet. Das TRB ist ein landwirtschaftlich intensiv genutztes Gebiet und trägt mit über 50% zur Energiegewinnung aus Wasserkraft in Kenia bei. Somit hat das Einzugsgebiet eine entscheidende Rolle für die Ernährungssicherheit in der Region und die Wirtschaftsleistung Kenias. Eine mögliche Minimierung der Auswirkungen hydrometeorologischer Extremereignisse erfordert ein verbessertes hydrometeorologisches Systemverständnis der Region. Diese Doktorarbeit leistet insbesondere einen Beitrag zum verbesserten Kenntnisstand über den atmosphärisch-terrestrischen Wasserhaushalt des TRB. Das wird durch die Anwendung des regionalen Klimamodells (RCM, *Regional Climate Model*) *Weather Research and Forecasting Model* (WRF) und des gekoppelten WRF-Hydro Modellsystems erreicht.

Es wird analysiert, wie gut WRF Niederschlag und Temperatur im Zeitraum von 2011 bis 2014 reproduzieren kann. Die WRF-Simulationen werden mit den Niederschlagsdatensätzen *Tropical Rainfall Measuring Mission* (TRMM), *Climate Hazards Group Infrared Precipitation with Station* (CHIRPS), *Climate Research Unit* (CRU), *Global Land Evaporation Amsterdam Model* (GLEAM) und Stationsdaten verglichen. Des Weiteren wird das ungekoppelte WRF-Hydro Modell kalibriert, um Parameter zu finden, mit denen die hydroklimatologischen Eigenschaften des oberen TRB reproduziert werden können. Die Kalibrierung basiert auf Abflussdaten des Pegels (Pegel-ID 4BE10) in Rukanga, gelegen an der Mündung des Teileinzugsgebietes Mathioya-Sagana (3279 km²).

Die Fähigkeit von WRF, den saisonalen Verlauf von Niederschlag und Temperatur im TRB über einen Zeitraum von vier Jahren zu reproduzieren, wird in zwei Schritten untersucht: Der erste Schritt ist die Identifikation optimaler Modell-Parametrisierungen und der zweite ist die Verbesserung der Konfiguration basierend auf dem Einfluss der beiden unterschiedlichen Landnutzungsklassifikationen *Moderate Resolution Imaging Spectroradiometer* (MODIS) und *U.S. Geological Survey* (USGS) in unterschiedlichen Auflösungen (50 km und 25 km). Die untersuchten Parametrisierungen umfassen drei Ansätze für Konvektion und Kumulusbewölkung: Kain-Fritsch (KF), Grell Freitas (GF) und Betts Miller Janjic (BMJ), und zwei Ansätze für die Mikrophysik: WRF Single Moment 6-class (WSM6) und Lin *et al.* (LIN). Alle anderen Parametrisierungen bleiben

unverändert. Die Konfiguration mit KF, WSM6 und ACM2 (KWA) liefert bessere Ergebnisse bei der Simulation der jahreszeitlichen und jährlichen Niederschlagsmenge. Für die Temperatur liefern alle sechs betrachteten Konfigurationen ähnliche Ergebnisse, wobei sie im Vergleich mit Stationsdaten und dem CRU-Datensatz einen systematischen Fehler hin zu kälteren Temperaturen (*cold bias*) aufweisen. Die Sensitivitätsanalysen zeigen, dass alle WRF-Simulationen die zeitliche (annuell und interannuell) und räumliche Verteilung des Niederschlages im TRB im Vergleich mit Stationsdaten und TRMM gut erfassen. Die Ergebnisse lassen erkennen, dass mit einer Erhöhung der horizontalen Auflösung von WRF von 50 km auf 25 km in Kombination mit der Verwendung der MODIS Landnutzungsklassifikation eine signifikante Verbesserung beim modellierten Niederschlag erreicht werden kann. Bei der Temperatur ist jedoch kein erkennbarer Unterschied zwischen den verschiedenen Experimenten zu sehen. Im Allgemeinen reproduziert WRF die räumlichen Muster und den jahreszeitlichen Verlauf in angemessener Weise, wobei aber ein systematischer Fehler hin zu kälteren Temperaturen festgestellt werden kann (im Vergleich mit Stationsdaten und dem CRU-Datensatz). Die Ergebnisse dieser Untersuchung tragen somit zur Identifikation geeigneter und regional angepasster RCMs für Ostafrika bei.

Die Simulationen mit WRF und dem gekoppelten WRF-Hydro, die das Teileinzugsgebiet Mathioya-Sagana mit einer Gitterweite von 5 km auflösen, zeigen gute Ergebnisse in Bezug auf Niederschlag und Evapotranspiration (ET). Der simulierte Niederschlag liegt näher an den von CHIRPS abgeleiteten Werten als an denen von TRMM. Bezüglich der Evapotranspiration erfassen WRF und das gekoppelte WRF-Hydro den zeitlichen Verlauf der GLEAM-Daten, wobei eine leichte Unterschätzung festzustellen ist. Der akkumulierte Abfluss aus dem gekoppelten WRF-Hydro (ca. 323 mm/a) liegt sehr nahe am beobachteten (ca. 333 mm/a) und zeigt dabei eine niedrige *Nash-Sutcliffe-Efficiency* (NSE) von 0.02 und ein gutes Verhältnis des *Root Mean Squared Error* (RMSE) zur Standardabweichung der gemessenen Daten (*ratio of RMSE to the standard deviation of the observations*, RSR) von 0.99, bei täglicher Betrachtung.

Schließlich wurde eine Methode entwickelt, mit der die gemeinsame atmosphärisch-terrestrische Wasserbilanz des Mathioya-Sagana Teileinzugsgebietes basierend auf Simulationen mit WRF und WRF-Hydro untersucht werden kann. Die Analyse zeigt, dass das gekoppelte WRF-Hydro verglichen mit WRF den Niederschlag, die Evapotranspiration und die Bodenfeuchtigkeit leicht verringert, aber den Abfluss erhöht. Unterschiede im Niederschlagsrecycling sowie die Effizienzmaße zwischen WRF und

dem gekoppelten WRF-Hydro liegen nahe beieinander und sind vergleichsweise klein. Das ist ein Hinweis darauf, dass der größte Teil des Niederschlages in der Region aus der Advektion von Feuchtigkeit von außerhalb des betrachteten Gebietes stammt, so dass potentielle Rückkopplungsmechanismen zwischen Land und Niederschlag nur geringe Auswirkungen haben.

Contents

<u>Acknowledgements</u>	<u>i</u>
<u>Abstract</u>	<u>iii</u>
<u>Zusammenfassung</u>	<u>v</u>
<u>List of Abbreviations</u>	<u>xii</u>
<u>List of Figures</u>	<u>xiii</u>
<u>List of Tables</u>	<u>xx</u>
<u>I Introduction</u>	<u>- 1 -</u>
I.1 MOTIVATION	- 1 -
I.2 RELATED REGIONAL CLIMATE MODELING STUDIES	- 2 -
I.3 OBJECTIVE OF THE STUDY	- 4 -
I.4 INNOVATION	- 6 -
I.5 STUDY AREA	- 6 -
I.5.1 HYDROCLIMATOLOGY OF THE STUDY AREA	- 7 -
I.6 STRUCTURE OF THE THESIS	- 9 -
<u>II Description of the numerical models, datasets and methods</u>	<u>- 11 -</u>
II.1 WRF MODELING SYSTEM	- 11 -
II.2 WRF-HYDRO MODELING SYSTEM	- 12 -
II.3 COUPLING OF WRF AND WRF-HYDRO	- 14 -
II.4 MODEL CONFIGURATIONS/PARAMETERIZATION	- 16 -
II.5 OBSERVATIONAL DATASETS	- 19 -
II.6 UNCOUPLED WRF-HYDRO CALIBRATION	- 21 -
II.7 WATER BALANCE COMPUTATION	- 30 -
<u>III WRF-only: Sensitivity and performance at 50 and 25 km</u>	<u>- 33 -</u>
III.1 INTRODUCTION	- 33 -

III.2 RAINFALL AND TEMPERATURE CLIMATOLOGY OF TANA RIVER BASIN	- 34 -
III.2.1 UPPER TANA	- 34 -
III.2.2 MIDDLE TANA	- 35 -
III.2.3 LOWER TANA	- 36 -
III.3 PRECIPITATION	- 37 -
III.3.1 MODEL RESULTS AT 50 KM HORIZONTAL RESOLUTION VERSUS STATION OBSERVATIONS	- 37 -
III.3.2 MODEL RESULTS AT 50 KM HORIZONTAL RESOLUTION VERSUS TRMM DATA	- 40 -
III.4 TEMPERATURE	- 42 -
III.4.1 MODEL RESULTS AT 50 KM HORIZONTAL RESOLUTION VERSUS STATION TEMPERATURES	- 42 -
III.4.2 MODEL RESULTS AT 50 KM HORIZONTAL RESOLUTION VERSUS CRU TEMPERATURE	- 46 -
III.5 IMPACT OF LAND USE AND HORIZONTAL RESOLUTION ON MODELED PRECIPITATION	- 48 -
III.5.1 LAND USE DISTRIBUTION IN THE TRB	- 48 -
III.5.2 MODEL RESULTS VERSUS STATION DATA	- 49 -
III.5.3 MODEL RESULTS VERSUS GRIDDED DATA	- 52 -
III.6 IMPACT OF LAND USE AND HORIZONTAL RESOLUTION ON MODELED TEMPERATURE	- 60 -
III.6.1 MODEL RESULTS VERSUS STATION TEMPERATURE	- 60 -
III.6.2 MODELED RESULTS VERSUS CRU TEMPERATURE	- 62 -
III.7 SUMMARY AND DISCUSSION	- 63 -
<u>IV WRF and WRF-Hydro: Sensitivity and performance at 5 km</u>	- 65 -
IV.1 INTRODUCTION	- 65 -
IV.1.1 MATHIOYA-SAGANA SUBCATCHMENT (MSS) AREA	- 65 -
IV.2 PRECIPITATION	- 66 -
IV.2.1 MODEL RESULTS VERSUS STATION DATA	- 66 -
IV.2.2 MODEL RESULTS VERSUS GRIDDED DATA	- 68 -
IV.2.3 SEASONAL AND CUMULATIVE TOTALS	- 70 -
IV.2.4 INTERANNUAL VARIABILITY	- 71 -
IV.2.5 SPATIAL PRECIPITATION OVER THE MATHIOYA-SAGANA SUBCATHMENT	- 73 -
IV.3 COUPLED WRF-HYDRO SIMULATED DISCHARGE VERSUS OBSERVED	

DISCHARGE	- 74 -
IV.4 SUMMARY AND DISCUSSION	- 78 -
<u>V Terrestrial Water Balance for Mathioya-Sagana Subcatchment</u>	- 80 -
V.1 INTRODUCTION	- 80 -
V.2 THE GLOBAL LAND EVAPORATION AMSTERDAM MODEL (GLEAM) AND SIMULATED ET	- 81 -
V.2.1 INTERANNUAL VARIABILITY OF ET	- 83 -
V.3 VERIFICATION OF CHANGE IN TERRESTRIAL WATER STORAGE DS/DT	- 84 -
V.4 INTERANNUAL VARIABILITY OF TWB COMPONENTS	- 85 -
V.4.1 RELATIONSHIP BETWEEN WRF-ONLY AND COUPLED WRF-HYDRO COMPONENTS	- 88 -
V.4.2 ANNUAL MEAN OF TERRESTRIAL WATER BALANCE COMPONENTS	- 89 -
V.5 SUMMARY AND DISCUSSION	- 91 -
<u>VI Atmospheric Water Balance for Mathioya-Sagana Subcatchment</u>	- 93 -
VI.1 INTRODUCTION	- 93 -
VI.1.1 SEASONAL AND INTERANNUAL VARIABILITY OF AWB COMPONENTS	- 93 -
VI.2 RELATIONSHIP BETWEEN WRF-ONLY AND COUPLED WRF-HYDRO COMPONENTS	- 95 -
VI.2.1 MEAN ANNUAL CYCLE OF AWB COMPONENTS	- 96 -
VI.2.2 ANNUAL AVERAGES OF THE AWB COMPONENTS	- 99 -
VI.3 RELATIONSHIP BETWEEN MEAN VAPOR CONVERGENCE AND STREAMFLOW	- 100 -
VI.4 LAND-ATMOSPHERIC INTERACTIONS WITHIN THE MATHIOYA-SAGANA SUBCATCHMENT	- 102 -
VI.4.1 RECYCLING RATIO B	- 102 -
VI.4.2 PRECIPITATION EFFICIENCY X	- 104 -
VI.4.3 MEAN ANNUAL AVERAGES OF B AND X	- 104 -
VI.5 FURTHER ESTIMATION OF TERRESTRIAL WATER STORAGE DS/DT	- 105 -
VI.6 SUMMARY AND DISCUSSION	- 108 -
<u>VII Conclusions and outlook</u>	- 110 -
VII.1 CONCLUSIONS	- 110 -

Contents

VII.1.1 PERFORMANCE OF THE WRF RCM	- 110 -
VII.1.2 APPLICATION OF WRF-HYDRO	- 110 -
VII.2 OUTLOOK	- 111 -

<u>Bibliography</u>	- 112 -
----------------------------	----------------

<u>Appendix A: Meteorological forcing data</u>	- 121 -
---	----------------

<u>Appendix B: Statement of the objective criteria and other statistical measures</u>	- 125 -
--	----------------

<u>Appendix C: Computation of the water balance components</u>	- 128 -
---	----------------

List of Abbreviations

ACM2	Asymmetric convective model version 2
AVHRR	Advanced Very High Resolution Radiometer
AWB	Atmospheric water balance
CHIRPS	Climate Hazards Group InfraRed Precipitation with Station data
CORDEX	Coordinated Regional Climate Downscaling Experiment
CRU	Climate Research Unit
ENSO	El Niño–Southern Oscillation
GHA	Greater Horn of Africa
GLEAM	Global Land Evaporation Amsterdam Model dataset
HRLDAS	High Resolution Land Data Assimilation System
ITCZ	Intertropical Convergence Zone
KF	Kain Fritsch
KMD	Kenya Meteorological Department
MODIS	Moderate Resolution Imaging Spectroradiometer
Noah-LSM	Noah Land Surface Model
OND	October–November–December
RCM	Regional circulation model
RRTM	Rapid radiative transfer model
TRB	Tana River basin
TRMM	Tropical Rainfall Measuring Mission data
TWB	Terrestrial water balance
USGS	United States Geological Survey
WARMA	Water Resource Management Authority
WRF	Weather Research and Forecasting modeling system
WSM6	WRF Single Moment 6-class

List of Figures

FIGURE I-1: MAP OF THE STUDY AREA AND LOCATION OF METEOROLOGICAL STATIONS (NYERI, EMBU, MERU, THIKA, GARISSA, MAKINDU, LAMU) MARKED AS RED DOTS. INSET BLACK BOUNDARY MARKS THE TANA RIVER BASIN (TRB), KENYA; BLUE RECTANGULAR SHOWS THE MATHIOYA-SAGANA SUBCATCHMENT (MSS; RED CONTOUR) AND SURROUNDING. THE DOTTED BLACK LINES MARK THE ARBITRARY BOUNDARIES OF UPPER, MIDDLE AND LOWER TRB DEPICTED AS UT, MT AND LT RESPECTIVELY - 7 -

FIGURE I-2: AVERAGE ANNUAL RAINFALL FOR THE TANA RIVER BASIN (TRB) SOURCED FROM WORLD RESOURCE INSTITUTE (GIS) ARCHIVES ([HTTP://WWW.WRI.ORG/RESOURCES/DATA-SETS/KENYA-GIS-DATA](http://www.wri.org/resources/data-sets/kenya-gis-data), DOWNLOADED ON 13TH APRIL, 2016). THE RAINFALL DATA IS AVERAGED FOR 50 YEARS (1950-2000) AT A SPATIAL RESOLUTION OF 1 KM AND IS SOURCED FROM STATION DATA - 9 -

FIGURE II-1: SKETCH OF THE WRF-HYDRO MODELING SYSTEM SHOWING THE VARIOUS COMPONENTS (GOCHIS *ET AL.*, 2015). - 15 -

FIGURE II-2: MODEL DOMAINS AT 25 KM AND 5 KM HORIZONTAL RESOLUTION (D1 IN BLACK; D2 IN PINK). BLUE CONTOUR MARKS THE TRB BOUNDARY AND THE INSET BLACK BOX IN D2 DEFINES PART OF THE MATHIOYA SAGANA SUBCATCHMENT. THE ELEVATION (M) THAT COVERS MOST OF D2 IS PROCESSED FROM THE SHUTTLE RADAR TOPOGRAPHY MISSION (SRTM) AT 3 ARC-SECOND (90-METRES) RESOLUTION; SOURCE: [HTTP://WWW.WRI.ORG/RESOURCES/DATA-SETS/KENYA-GIS-DATA#ELEVATION](http://www.wri.org/resources/data-sets/kenya-gis-data#elevation) - 18 -

FIGURE II-3: TIME SERIES OF DAILY OBSERVED AND SIMULATED DISCHARGE AT TANA RUKANGA’S RGS 4BE10 IN RESPONSE TO VARIATION OF THE SURFACE RUNOFF PARAMETER (REFKDT) FOR 2012..... - 24 -

FIGURE II-4: SIMILAR TO FIGURE II-3 BUT SHOWS SENSITIVITY TO THE RETENTION DEPTH PARAMETER, RETDEPRTFAC..... - 26 -

FIGURE II-5: SIMILAR TO FIGURE II-3 BUT SHOWS SENSITIVITY TO THE SURFACE ROUGHNESS SCALING FACTOR, OVROUGHRTFAC - 27 -

FIGURE II-6: SIMILAR TO FIGURE II-3 BUT FOR THE IMPACT OF THE CHANNEL MANNING’S ROUGHNESS COEFFICIENTS (MANNN) WITH SCALE FACTOR 0.4-1.2 - 28 -

FIGURE II-7: SIMILAR TO FIGURE II-6 BUT FOR THE MANNN SCALE FACTOR 1.4 – 2.0 - 28 -

FIGURE II-8: SUMMARY OF THE OFFLINE (UNCOUPLED) WRF-HYDRO AND OBSERVED DISCHARGE AT TANA RUKANGA’S RGS 4BE10 HYDROGRAPHS AND HYETOGRAPH BASED ON TRMM FOR 2012..... - 29 -

FIGURE III-1: CLIMATE DIAGRAMS FOR THE UT STATIONS AND THE CORRESPONDING ELEVATION MAP FOR THE TRB..... - 35 -

List of Figures

FIGURE III-2: CLIMATE DIAGRAMS FOR THE METEOROLOGICAL STATIONS AND THE CORRESPONDING ELEVATION MAP FOR THE TRB	- 36 -
FIGURE III-3: CLIMATE DIAGRAM FOR THE LT REGION AND THE CORRESPONDING ELEVATION MAP FOR TRB.....	- 37 -
FIGURE III-4: MONTHLY GRIDDED PRODUCTS WHICH ARE MEAN CENTERED FROM THE SIX WRF EXPERIMENTS COMPARED TO RAINFALL DATA FROM SELECTED STATIONS OVER THE TANA RIVER BASIN FOR 2011-2014.....	- 38 -
FIGURE III-5: MEAN SEASONAL (MAM AND OND) PRECIPITATION AS OBSERVED IN THE STATIONS AND SIMULATED OVER DIFFERENT SECTIONS OF TANA RIVER BASIN SHOWN IN BARS. THE MEAN IS COMPUTED FROM THE SEASONAL TOTALS DURING 2011-2014. THE ERROR BARS INDICATE THEIR CORRESPONDING STANDARD DEVIATION	- 40 -
FIGURE III-6: MEAN SEASONAL (MAM AND OND) SPATIALLY AVERAGED PRECIPITATION AS ESTIMATED IN TRMM AND SIMULATED IN THE SIX WRF EXPERIMENTS OVER THE TRB. THE MEAN IS COMPUTED FROM THE SEASONAL TOTALS DURING 2011-2014. THE ERROR BARS INDICATE THEIR CORRESPONDING STANDARD DEVIATION	- 42 -
FIGURE III-7: SCATTER PLOT SHOWING SIMULATED AND OBSERVED (STATION) MEAN CENTERED MONTHLY MEAN TEMPERATURES (MINIMUM, MAXIMUM AND MEAN) FROM THE SIX WRF CONFOGURATIONXS FOR THE PERIOD 2011-2014.....	- 45 -
FIGURE III-8: MONTHLY MEAN TEMPERATURE (MINIMUM, MAXIMUM, AND MEAN) SPATIALLY AVERAGED OVER THE STUDY AREA FOR THE PERIOD 2011-2014, DERIVED FROM CRU AND THE SIX WRF SIMULATIONS	- 47 -
FIGURE III-9: THE DOMINANT LAND USE CATEGORY IN EACH GRID POINT OVER THE TRB: (A) MODIS25, (B) MODIS50, (C) USGS25 AND, (D) USGS50 DURING THE PERIOD 2011-2014 (KERANDI <i>ET AL.</i> , 2016).....	- 49 -
FIGURE III-10: MEAN ANNUAL CYCLE OF PRECIPITATION OVER THE STATIONS IN THE THREE SUB REGIONS OF THE TRB (A) UPPER TRB, (B) MIDDLE TRB, AND (C) LOWER TRB (IN MM/DAY) DERIVED FROM STATION DATA AND WRF SIMULATIONS: MODIS25, MODIS50, USGS25 AND USGS50 FOR 2011-2014	- 50 -
FIGURE III-11: STANDARD DEVIATION OF ANNUAL, SEASONAL (MAM, OND) TOTAL PRECIPITATION DURING THE PERIOD 2011-2014. PRECIPITATION IS DERIVED FROM STATION DATA DISTRIBUTED OVER THE TRB SUB-REGIONS AND THE FOUR WRF CONFIGURATIONS (USGS50, MODIS50, MODIS25, AND USGS25)	- 52 -
FIGURE III-12: ANNUAL CYCLE OF MONTHLY AVERAGED PRECIPITATION (IN MM/DAY) SPATIALLY AVERAGED OVER THE STUDY REGION FOR THE PERIOD 2011-2014, DERIVED FROM TRMM AND THE FOUR WRF EXPERIMENTS.....	- 53 -

List of Figures

FIGURE III-13: TOTAL SEASONAL (MAM, OND) AMOUNT OF OBSERVED AND SIMULATED PRECIPITATION FOR INDIVIDUAL YEARS (2011-2014) SPATIALLY AVERAGED OVER THE STUDY REGION.....	- 54 -
FIGURE III-14: STANDARD DEVIATION OF THE ANNUAL, SEASONAL (MAM, OND), TOTAL PRECIPITATION DURING 2011-2014, SPATIALLY AVERAGED OVER THE STUDY REGION. THE PRECIPITATION IS DERIVED FROM TRMM AND THE FOUR WRF CONFIGURATIONS	- 55 -
FIGURE III-15: PRECIPITATION MAPS OF THE STUDY AREA AVERAGED FOR MAM SEASON FOR THE PERIOD 2011-2014, DERIVED FROM (1 ST ROW) TRMM, (2 ND ROW) MODIS25, (3 RD ROW) MODIS50, (4 TH ROW) USGS25, AND (5 TH ROW) USGS50. THE RED CONTOUR LINE DELINEATES PART OF TRB BOUNDARY	- 56 -
FIGURE III-16: PRECIPITATION MAPS OF THE STUDY AREA AVERAGED FOR OND FOR THE PERIOD 2011-2014, DERIVED FROM (1 ST ROW) TRMM, (2 ND ROW) MODIS25, (3 RD ROW) MODIS50, (4 TH ROW) USGS25, AND (5 TH ROW) USGS50. THE RED CONTOUR DELINEATES PART OF TRB BOUNDARY	- 57 -
FIGURE III-17: NORMALIZED PATTERN STATISTICS DURING THE MAM SEASON DERIVED THE FOUR WRF EXPERIMENTS: MODIS50, USGS50, MODIS25, AND USGS25. THE REFERENCE DATA (OBS. PRECIP) IS DERIVED FROM TRMM FOR THE PERIOD 2011-2014.....	- 59 -
FIGURE III-18: NORMALIZED PATTERN STATISTICS DURING THE OND SEASON DERIVED FROM THE FOUR WRF EXPERIMENTS: MODIS50, USGS50, MODIS25, AND USGS25. THE REFERENCE DATA (OBS. PRECIP) IS DERIVED FROM TRMM FOR THE PERIOD 2011-2014.....	- 59 -
FIGURE III-19: NORMALIZED PATTERN STATISTICS SHOWING THE MONTHLY MEAN OVER ALL MARCH-MAY (MAM) AND OCTOBER-DECEMBER (OND) DERIVED FROM THE FOUR WRF EXPERIMENTS: MODIS50, USGS50, MODIS25, USGS25 IN REFERENCE TO TRMM DATA (OBS. PRECIP) FOR THE PERIOD 2011-2014.....	- 60 -
FIGURE III-20: STANDARD DEVIATION OF ANNUAL, SEASONAL (MAM, OND) MEAN TEMPERATURE OVER SELECTED STATIONS IN TRB DURING THE PERIOD 2011-2014.....	- 61 -
FIGURE III-21: NORMALIZED STATISTICAL COMPARISON OF THE SPATIALLY AVERAGED MEAN TEMPERATURE DURING MAM SEASON OVER THE STUDY AREA FOR THE PERIOD 2011-2014.....	- 62 -

List of Figures

FIGURE III-22: NORMALIZED STATISTICAL COMPARISON OF SPATIALLY AVERAGED MEAN TEMPERATURE DURING OND SEASON OVER THE STUDY AREA FOR THE PERIOD 2011-2014.....	- 63 -
FIGURE IV-1: MATHIOYA-SAGANA SUBCATCHMENT (MSS; MARKED BY RED CONTOUR) AND SURROUNDING SHOWING: (A) DOMINANT LAND USE CLASSES BASED ON MODIS, AND (B) THE DIGITAL ELEVATION MODEL (DEM), 90-M, 3 ARC-SECOND DATASET. ONE METEOROLOGICAL STATION (NYERI), TWO RAIN STATIONS (SAGANA, MURANG'A), TANA RUKANGA'S RGS 4BE10 AND RIVER NETWORK IN THE MSS.....	- 66 -
FIGURE IV-2: SCATTER PLOT SHOWING MEAN CENTERED SIMULATED (WRF-ONLY, COUPLED WRF-HYDRO) AND STATIONS (NYERI, MURANGA, SAGANA) PRECIPITATION DATA OVER MSS FOR 2011-2014	- 67 -
FIGURE IV-3: SEASONAL TOTALS (MAM, OND) AMOUNT OF OBSERVED (STATION DATA) AND SIMULATED (WRF-ONLY, COUPLED WRF-HYDRO) FOR INDIVIDUAL YEARS DURING 2011 TO 2014	- 68 -
FIGURE IV-4: TIME SERIES OF MONTHLY PRECIPITATION (IN MM/DAY) SPATIALLY AVERAGED OVER MSS AND ITS SURROUNDING (SEE FIG. 4.1) FOR THE PERIOD 2011-2014 DERIVED FROM TRMM, CHIRPS, WRF-ONLY AND COUPLED WRF-HYDRO.....	- 69 -
FIGURE IV-5: (TOP) TOTAL SEASONAL (MAM + OND), AND (BOTTOM) CUMULATIVE TOTAL PRECIPITATION DERIVED FROM TRMM AND CHIRPS AND SIMULATED IN WRF-ONLY/COUPLED WRF-HYDRO DURING 2011 TO 2014.....	- 71 -
FIGURE IV-6: TAYLOR DIAGRAM SHOWING PATTERN CORRELATION R , NORMALIZED STANDARD DEVIATION Σ AND NORMALIZED ROOT MEAN SQUARE ERROR $RMSE$ FOR MONTHLY MEAN PRECIPITATION SIMULATED IN WRF-ONLY AND COUPLED WRF-HYDRO COMPARED TO CHIRPS (OBSERVED PRECIPITATION) DURING MAM SEASON FOR INDIVIDUAL YEARS.....	- 72 -
FIGURE IV-7: TAYLOR DIAGRAM SHOWING PATTERN CORRELATION R , NORMALIZED STANDARD DEVIATION Σ AND NORMALIZED ROOT MEAN SQUARE ERROR $RMSE$ FOR MONTHLY MEAN PRECIPITATION SIMULATED IN WRF-ONLY AND COUPLED WRF-HYDRO COMPARED TO CHIRPS (OBSERVED PRECIPITATION) DURING OND SEASON FOR INDIVIDUAL YEARS.....	- 73 -
FIGURE IV-8: PRECIPITATION MAPS OF MSS REGION AVERAGED FOR ALL MAM AND OND SEASONS DURING 2011-2014: (A-C) MAM (D-F) OND. THE FIRST COLUMN REPRESENTS CHIRPS, 2 ND COLUMN REPRESENTS WRF-ONLY, AND 3 RD COLUMN REPRESENTS COUPLED WRF-HYDRO	- 74 -

List of Figures

FIGURE IV-9: OBSERVED AND SIMULATED (COUPLED WRF-HYDRO) HYDROGRAPHS AND HYETOGRAPH IN THE MSS FOR THE PERIOD 2011 TO 2014 AT 4E10 GAUGE STATION.....	- 75 -
FIGURE IV-10: SCATTER PLOT SHOWING COMPARISON OF SIMULATED AND OBSERVED DISCHARGE (A) DAILY TIME STEP (B) MONTHLY FLOW FOR THE PERIOD 2011-2014 AT TANA RUKANGA'S RGS 4BE10. THE BLUE LINE IS THE 1:1 LINE WHOSE INTERCEPT IS SET AT 0.0.....	- 76 -
FIGURE IV-11: SCATTER PLOT SHOWING COMPARISON OF SIMULATED AND OBSERVED DISCHARGE IN THE YEAR 2013 AT TANA RUKANGA'S RGS 4BE10. THE BLUE LINE IS THE 1:1 LINE WHOSE INTERCEPT IS SET AT 0.0.....	- 77 -
FIGURE IV-12: CUMULATIVE TOTALS OF SIMULATED AND OBSERVED DISCHARGE AT TANA RUKANGA'S RGS 4BE10 FOR THE PERIOD 2011-2014	- 78 -
FIGURE V-1: EVAPOTRANSPIRATION MAPS SPATIALLY AVERAGED OVER THE INNER DOMAIN (D2) FOR THE PERIOD 2011-2014, DERIVED FROM THE GLEAM DATASETS (ROW 1) AND SIMULATED IN WRF-ONLY AND COUPLED WRF-HYDRO (ROW 2). THE RED CONTOUR DELINEATES PORTION OF THE TRB	- 81 -
FIGURE V-2: NORMALIZED PATTERN STATISTICS OF COMPARISON OF TIME AVERAGED <i>ET</i> BETWEEN THAT DERIVED FROM GLEAM DATASETS AND SIMULATED BY WRF-ONLY AND COUPLED WRF-HYDRO FOR THE INNER DOMAIN DURING 2011-2014	- 82 -
FIGURE V-3: SCATTER PLOT OF THE MEAN CENTERED MONTHLY SUM OF <i>ET</i> DERIVED FROM GLEAM DATASETS (GLEAM_v3.0A, GLEAM_v3.0B AND GLEAM_v3.0C) COMPARED TO THAT SIMULATED IN WRF-ONLY AND COUPLED WRF-HYDRO SPATIALLY AVERAGED OVER MSS AND ITS SURROUNDING FOR THE PERIOD 2011 TO 2014.....	- 83 -
FIGURE V-4: MONTHLY AND INTERANNUAL VARIATION OF <i>ET</i> AS DERIVED FROM GLEAM_v3.0B DATASET AND SIMULATED IN WRF-ONLY AND COUPLED WRF-HYDRO OVER MSS AND SURROUNDING FOR 2011-2014.....	- 84 -
FIGURE V-5: MONTHLY AND INTERANNUAL VARIATION OF "ADAPTED OBSERVATIONS SHOWN IN RED" AND SIMULATED (WRF-ONLY SHOWN IN GREEN; COUPLED WRF-HYDRO SHOWN IN BLUE) dS/dt OVER MSS DURING 2011 TO 2014.....	- 85 -
FIGURE V-6: MONTHLY TWB COMPONENTS AS SIMULATED IN WRF-ONLY (TOP) AND COUPLED WRF-HYDRO (BOTTOM), SPATIALLY AVERAGED OVER MSS AND ITS SURROUNDING FOR THE PERIOD 2011-2014.....	- 86 -
FIGURE V-7: STANDARD DEVIATION OF MEAN ANNUAL, SEASONAL (MAM, OND) DISCHARGE AVERAGED DURING THE PERIOD 2011-2014	- 87 -

List of Figures

FIGURE V-8: MONTHLY DIFFERENCES (COUPLED WRF-HYDRO MINUS WRF-ONLY) OF TWB COMPONENTS (IN MM/DAY) FOR THE PERIOD 2011-2014 - 88 -

FIGURE V-9: MEAN ANNUAL TWB COMPONENTS AS OBSERVED AND SIMULATED FOR MSS FOR THE PERIOD 2011-2014 - 90 -

FIGURE VI-1: MONTHLY AWB COMPONENTS AS SIMULATED IN WRF-ONLY (TOP) AND COUPLED WRF-HYDRO (BOTTOM) FOR THE MSS AND SURROUNDING DURING 2011-2014: PRECIPITATION P , BLUE LINE; EVAPORATION ET , GREEN LINE; ATMOSPHERIC WATER VAPOR CONVERGENCE C , RED LINE; CHANGE IN ATMOSPHERIC WATER STORAGE dW/dt , MAGENTA LINE - 94 -

FIGURE VI-2: MONTHLY DIFFERENCES (COUPLED WRF-HYDRO MINUS WRF-ONLY) OF AWB COMPONENTS SHOWN IN FIGURE VI-1 FOR THE PERIOD 2011 TO 2014..... - 95 -

FIGURE VI-3: MEAN ANNUAL CYCLE OF AWB COMPONENTS AVERAGED DURING 2011 TO 2014 AS SIMULATED IN (TOP) WRF-ONLY AND (BOTTOM) COUPLED WRF-HYDRO FOR THE MSS AND ITS SURROUNDING..... - 97 -

FIGURE VI-4: MONTHLY TIMESERIES OF DISCHARGE AND ATMOSPHERIC CONVERGENCE AS SIMULATED BY WRF-ONLY AND COUPLED WRF-HYDRO DURING 2011 TO 2014 FOR MATHIOYA-SAGANA SUBCATCHMENT. OBSERVED DISCHARGE FOR MATHIOYA-SAGANA BASIN IS ALSO INCLUDED (RED LINE) - 100 -

FIGURE VI-5: MONTHLY TIME SERIES OF SIMULATED R AND dS/dt AND CORRESPONDING C OVER MSS FOR THE PERIOD 2011-2014 - 102 -

FIGURE VI-6: MONTHLY VARIATION OF THE RECYCLING RATIO FOR THE YEARS 2011 TO 2014 AS SIMULATED IN WRF-ONLY AND COUPLED WRF-HYDRO FOR THE MATHIOYA SAGANA SUBCATCHMENT - 103 -

FIGURE VI-7: MONTHLY VARIATION OF PRECIPITATION EFFICIENCY FOR THE YEARS 2011 TO 2014 FOR MATHIOYA-SAGANA SUBCATCHMENT AS SIMULATED IN WRF-ONLY AND COUPLED WRF-HYDRO..... - 104 -

FIGURE VI-8: MONTHLY AND INTERANNUAL VARIATION OF ESTIMATED dS/dt (TOPLEFT) BASED ON TWB COMPONENTS. THE RED LINE REPRESENT OBSERVATIONS, BLUE LINE REPRESENT THOSE FROM COUPLED WRF-HYDRO SIMULATIONS; GREEN LINE ARE FOR WRF-ONLY SIMULATIONS - 106 -

FIGURE VI-9: MONTHLY AND INTERANNUAL VARIATION OF ESTIMATED dS/dt BASED ON AWB AND MEASURED DISCHARGE R . THE RED LINE REPRESENT OBSERVATIONS, BLUE LINE REPRESENT THOSE FROM COUPLED WRF-HYDRO SIMULATIONS; GREEN LINE ARE FOR WRF-ONLY SIMULATIONS - 107 -

List of Figures

FIGURE VI-10: MONTHLY AND INTERANNUAL VARIATION OF ESTIMATED dS/dt BASED ON SIMULATED SOIL MOISTURE AND UNDERGROUND WATER. THE RED LINE REPRESENT OBSERVATIONS, BLUE LINE REPRESENT THOSE FROM COUPLED WRF-HYDRO SIMULATIONS; GREEN LINE ARE FOR WRF-ONLY SIMULATIONS..... - 107 -

FIGURE VI-11: SCATTER PLOT SHOWING THE MONTHLY ESTIMATED dS/dt TIMESERIS SHOWN IN FIGURE VI-8, FIGURE VI-9 AND FIGURE VI-10. THE DIFFERENT APPROACHES OF ESTIMATING dS/dt ARE COMPARED TO THE "OBSERVED dS/dt " - 108 -

List of Tables

TABLE II-1: SELECTED OBJECTIVE CRITERIA (NASH-SUTCLIFFE EFFICIENCY NSE AND RMSE-OBSERVATIONS STANDARD DEVIATION RSR) BETWEEN SIMULATED AND OBSERVED DISCHARGE AT TANA RUKANGA’S RGS 4BE10 BASED ON THE INFILTRATION-RUNOFF PARAMETER REFKDT, RETENTION FACTOR RETDEPRTFAC, OVERLAND FLOW ROUGHNESS SCALING FACTOR OVROUGHTFAC AND THE MANNING’S ROUGHNESS COEFFICIENTS MANNN. EXPERIMENTS IN ITALICS BOLD SHOW THE SELECTED PARAMETERS’ VALUE AND THE BEST NSE AND RSR AFTER CALIBRATION	- 25 -
TABLE III-1: THE ACRONYMS OF THE WRF SENSITIVITY EXPERIMENTS AT 50 KM HORIZONTAL RESOLUTION.....	- 33 -
TABLE III-2: MEAN ANNUAL AMOUNT OF PRECIPITATION (MAM + OND) SIMULATED BY THE SIX WRF CONFIGURATIONS AND DERIVED FROM TRMM SPATIALLY AVERAGED OVER STUDY AREA FOR 2011-2014.....	- 41 -
TABLE III-3: THE MEAN ANNUAL TEMPERATURE (MINIMUM, MAXIMUM, MEAN) DURING THE PERIOD 2011-2014 AS RECORDED IN THE STATIONS (NYERI, MERU, THIKA AND LAMU) AND THAT DERIVED FROM THE 6 WRF CONFIGURATIONS. THE ELEVATION M.A.S.L. OF EACH OF THE STATIONS IS INDICATED	- 44 -
TABLE III-4: THE CORRELATION COEFFICIENT, R AND MEAN ABSOLUTE ERROR, MAE BETWEEN MONTHLY MEAN TEMPERATURE (MINIMUM, MAXIMUM AND MEAN) DERIVED FROM CRU AND THE SIX WRF CONFIGURATIONS FOR 2011-2014	- 47 -
TABLE III-5: MEAN SEASONAL AND ANNUAL PRECIPITATION AVERAGED OVER STATIONS IN UPPER, MIDDLE AND LOWER TRB DURING 2011-2014	- 51 -
TABLE IV-1: SELECTED STATISTICS (MEAN ABSOLUTE ERROR, MAE, IN MM/DAY; ROOT MEAN SQUARE ERROR, RMSE, IN MM/DAY; CORRELATION COEFFICIENT, R; COEFFICIENT OF VARIATION, CV, IN % AND SKILL SCORE, SS) FOR SPATIALLY AVERAGED PRECIPITATION TIME SERIES SHOWN IN FIGURE IV-4. THE STATISTICS IN REFERENCE TO CHIRPS (C) ARE INDICATED IN BLUE, WHILE THOSE IN REFERENCE TO TRMM (T) ARE IN BLACK-	70 -
TABLE IV-2: SELECTED STATISTICS (NASH-SUTCLIFFE EFFICIENCY, NSE AND THE RMSE-OBSERVATIONS STANDARD DEVIATION RATIO, RSR) BETWEEN DISCHARGE IN COUPLED WRF-HYDRO AND OBSERVED AT 4BE10 GAUGE DURING THE PERIOD 2011-2014	- 76 -
TABLE V-1: THE 4-YEAR MEAN OF TWB COMPONENTS: <i>P</i> , <i>ET</i> , <i>R</i> AND <i>dS/dT</i> FOR THE MSS AND ITS SURROUNDING FOR THE PERIOD 2011 TO 2014	- 90 -
TABLE VI-1: ANNUAL DIFFERENCES BETWEEN COUPLED WRF-HYDRO AND WRF-ONLY AWB COMPONENTS SHOWN IN FIGURE VI-2. ALL VALUES ARE IN MM/DAY	- 96 -

List of Tables

TABLE VI-2: MEAN ANNUAL CYCLE OF AWB COMPONENTS SHOWING MONTHLY STANDARD DEVIATION. VALUES IN BOLD SHOW THE MONTH (S) WITH HIGHEST VARIABILITY FOR MAM AND OND SEASON	- 98 -
TABLE VI-3: ANNUAL AVERAGES OF THE AWB COMPONENTS AS SIMULATED IN WRF-ONLY AND COUPLED WRF-HYDRO DURING 2011 TO 2014 FOR MATHIOYA-SAGANA SUBCATCHMENT.....	- 99 -
TABLE VI-4: THE 4-YEAR MEAN OF THE ATMOSPHERIC VAPOR CONVERGENCE, C AND DISCHARGE, R AND THE DIFFERENCE BETWEEN THE TWO	- 101 -
TABLE VI-5: ANNUAL AVERAGES OF THE RECYCLING RATIO AND THE PRECIPITATION EFFICIENCY FOR MATHIOYA-SAGANA SUBCATCHMENT DURING 2011 TO 2014	- 105 -

I Introduction

I.1 Motivation

Understanding the variability of hydrometeorological variables in water-stressed environments like East Africa is fundamental in addressing water challenges, especially in the context of climate change and land use change. The understanding of hydrometeorological variability requires improved knowledge of the interaction between the atmospheric and terrestrial branches of the hydrological cycle. Regional climate modeling allows investigating the dependency of hydrometeorological variables to land use and land surface properties (Ge *et al.*, 2007). The validation of regional climate models (RCMs) requires observational data of several components of the water cycle, e.g., precipitation, evapotranspiration, runoff, soil moisture. These are typically difficult to obtain in a data-scarce region like Kenya, East Africa. It is only precipitation and runoff data which are sometimes available in this data-scarce region.

RCMs with their enhanced resolutions are known to permit adequate representation of land surface-atmospheric interactions, especially when coupled to appropriate land surface or hydrological models (Small *et al.*, 1999). Prior to this coupling, it is important to test the given RCM's capability to mimic the hydrometeorology of the study region. This is particularly important if the given RCM is being applied to the given region for the first time and also, if the purpose of the study is different from that of previous studies. This is done through carrying out sensitivity experiments based on the inherent parameters that govern RCM simulations which include physical parameterizations, such as atmospheric convection, cloud microphysics, planetary boundary layer, land-surface model, radiation schemes and other factors, such as land-use categories and horizontal and vertical resolutions (Pohl *et al.*, 2011). The importance of the parameterizations cannot be overemphasized as they take care of the important physical processes that cannot be resolved directly by a numerical model, yet being essential for the prediction of virtually all dependent variables (Stensrud, 2007; Warner, 2011).

It is emerging in the modeling community that coupled atmospheric-hydrological modeling is well placed for representation of water and energy fluxes and their related feedback mechanisms. Studies in water balance are an area that links all compartments of the climate system i.e., the atmosphere, cryosphere, lithosphere, biosphere and the

hydrosphere. These spheres are summarized in two branches of the water cycle: the terrestrial and the atmospheric branches. A number of studies (e.g., Eltahir and Bras, 1996; Shelton, 2009) have called for a holistic approach to study these two branches of the water cycle. This is because doing so is crucial in recognizing the coupled roles of the two branches along with their inherent non-linear feedbacks. However, many studies of water balance are skewed towards the terrestrial branch (Eltahir and Bras, 1996) which might not provide a comprehensive understanding of the variability of the hydro-meteorological variables of a given region of study like that of Tana River basin (TRB).

Changes in soil moisture (water storage) is one of the hydrometeorological variables considered to be of great importance for water resources, climate, agriculture and ecosystems (Yeh and Famiglietti, 2008). A number of studies (e.g., Findell and Eltahir 2003; Koster *et al.*, 2004; Anyah *et al.*, 2008) have argued that the influence of local soil moisture changes on precipitation is largest in arid and semi-arid regions dominated by convective precipitation, like Kenya. These soil moisture-precipitation interactions have been studied with the concept of precipitation recycling ratio and precipitation efficiency (Eltahir and Bras, 1996; Schär *et al.*, 1999; Kunstmann and Jung, 2007), which emphasize the significance of evapotranspiration on local precipitation. At river basin scale, both advection and evapotranspiration contribute to precipitation (Trenberth, 1999). The precipitation recycling analysis allows the quantification of the interaction between the atmospheric and terrestrial water balance components.

Studies investigating these interactions are limited due to lack of in-situ observations of hydrometeorological data such as humidity, wind, radiation, air pressure, soil moisture, evapotranspiration and runoff. Kenya and East Africa, in general, are lacking of in-situ observations. The lack of data can be mitigated by the use of RCMs' data for atmospheric-terrestrial water balance studies (e.g., Kunstmann and Jung, 2007; Music and Caya 2007; Roberts and Snelgrove, 2015).

I.2 Related regional climate modeling studies

The application of RCMs as a means of understanding the local climate in regions that have complex topography such as the TRB and East Africa in general is crucial (Endris *et al.*, 2013). In this context, there have been various investigations on the variability of various aspects of the climate for larger East Africa (Anyah *et al.*, 2006; Cook and Vizy,

2012; Endris *et al.*, 2013; Pohl *et al.*, 2011; Riddle and Cook, 2008; Segele *et al.*, 2009; Song *et al.*, 2002; Song *et al.*, 2004; Sun *et al.*, 1999). However, most of these studies only use a stand-alone version of the respective RCMs with only a few of them applying coupled modeling approaches. Anyah *et al.* (2006) used a fully coupled regional climate-three-dimensional lake modeling system, i.e., the Princeton Ocean Model (RegCM3-POM) to investigate the physical mechanisms associated with multiscale variability of the Lake Victoria basin. They showed the capability of the model to reproduce the basin rainfall climatology consistent with *Tropical Rainfall Measuring Mission* (TRMM) estimates. Further, they observed that the basin's precipitation was much influenced by large scale external moisture advection enhanced by the prevailing easterly trade winds. On their part, Cook and Vizy (2012) used the WRF model to investigate the impact of climate change on the mid-twenty first century growing season in Africa. They noted the wide variation of growing seasons in different regions was associated with changes in precipitation and evapotranspiration. Endris *et al.* (2013) recently, used the WRF model together with 9 different RCMs at 50 km horizontal resolution in the Coordinated Regional Climate Downscaling Experiment (CORDEX) to simulate the characteristics of rainfall patterns over East Africa. The CORDEX results indicated that WRF based on the Kain Fritsch (KF) cumulus convection, WRF Single-Moment 5-class (WSM5) microphysics, Yonsei University (YSU) planetary boundary, Dudhia short wave radiation and Rapid Radiative Transfer Mode (RRTM) long wave radiation schemes overestimated rainfall far above all the other RCMs assessed. Pohl *et al.* (2011) tested a number of WRF model settings, i.e., physical parameterization, land use categories, domain size and number of vertical levels in simulating the seasonal water cycle over the Equatorial East Africa for 1999. In their study, they found WRF simulations of spatial resolution of 36 km were closest to that from the *Global Precipitation Climatology Project daily* (GPCP-1dd) gridded rainfall product, when combining the Kain Fritsch (KF) cumulus scheme with the WRF Single-Moment 6-class (WSM6) microphysics, Asymmetric Convective Model version 2 (ACM2) planetary boundary layer, Dudhia short wave radiation, and the Rapid Radiative Transfer Model (RRTM) long wave radiation scheme. Riddle and Cook (2008) using the predecessor of WRF model, the PSU/NCAR Mesoscale Model (MM5) examined the yearly occurrence of a monsoon jump of approximately 20° latitude during the boreal spring and summer rainy season over the Greater Horn of Africa (GHA) forming a basis then for an understanding of the precipitation cycle over the region. In spite of the aforementioned, RCM stud-

ies in East Africa are still scarce as well as the prediction of its climate variability do remain challenging (Vera *et al.*, 2013).

In previous studies, there has been large sensitivity of the WRF model results following the choice of physics parameterizations. Within this context and towards contributing to a suitable configuration for the WRF model that reproduce the East Africa's, and in particular the TRB hydroclimatology, this thesis extend the work of Endris *et al.* (2013) and Pohl *et al.* (2011) in terms of the impact of the model horizontal resolution and land use data.

As stated by Kunstmann and Stadler (2005), the application of RCMs coupled with hydrological models are gaining scientific attention as it enhances the description of soil processes involved in the terrestrial water balance. Studies that have applied a fully coupled modeling system with emphasis on the atmospheric-terrestrial interactions (e.g., Maxwell *et al.*, 2011; Senatore *et al.*, 2015; Wagner *et al.*, 2016; Arnault *et al.*, 2016) exploit the advantage of inclusion of the soil moisture redistribution feedback in the lower boundary conditions of atmospheric models. This can lead to an improved representation of water and energy fluxes between land and atmosphere, which is not available in a one-way coupled modeling system.

The coupled WRF-Hydro, a combination of the atmospheric Weather Research and Forecasting (WRF) model and a hydrological module referred to as uncoupled WRF-Hydro (Skamarock *et al.*, 2008; Gochis *et al.*, 2015) provides such a coupling approach. This coupled modeling system is a recent development designed to provide more accurate information related to the spatial redistribution of surface, subsurface and channel waters across land surfaces and more importantly as an enhancement to coupling of hydrologic models with atmospheric models. Both coupled and uncoupled WRF-Hydro have been applied only for few studies so far (Yucel *et al.*, 2015; Senatore *et al.*, 2015; Arnault *et al.*, 2016; Givati *et al.*, 2016).

I.3 Objective of the study

The Tana River basin (TRB) is both vulnerable and prone to hydrological extremes like droughts and floods. These two extremes which eventually affect water availability are aggravated by climate change induced small changes of the prevailing seasonal precipitation pattern characteristic of semiarid to arid regions (e.g., Lutz *et al.*, 2012). Yet,

TRB is an extensive agricultural area that also contributes to more than half of Kenya's hydropower production. The basin is thus a contributor to the population's food security in this region and the Kenya's economy in general. This calls for proper understanding of the basin's hydrometeorology as a mean's of managing and mitigating the impacts of the extremes mentioned above.

The study aims to apply the coupled WRF-Hydro modeling system in order to characterize the atmospheric-terrestrial water balance components for the Mathioya-Sagana subcatchment and its surrounding. The main objective of this thesis is to improve the understanding of hydrometeorological processes in the study region. The Mathioya-Sagana is located at the northwest of upper TRB. The research questions of this study include:

1. Does the coupled atmospheric-hydrological model improve the representation of the joint atmospheric-terrestrial water balance, in comparison to the stand-alone atmospheric model?
2. How critical are land-precipitation feedback mechanisms over the Mathioya-Sagana subcatchment?

These questions will be addressed through the following research tasks:

1. Identification of a suitable configuration of the Weather Research and Forecast modeling system WRF (Skamarock *et al.*, 2008) for the TRB following earlier studies (Pohl *et al.*, 2011). The WRF model is the tool selected as an atmospheric part of the coupled modeling system. Details of the model are presented in Section II.1.
2. Identification of a suitable set up of the uncoupled WRF-Hydro (Gochis *et al.*, 2015) for the Mathioya-Sagana subcatchment. WRF-Hydro constitutes the hydrological part of the coupled modeling system. The description of the model is in Section II.2.
3. Applying the coupled WRF-Hydro modeling system to the Mathioya-Sagana subcatchment and its surrounding and derivation of the atmospheric and terrestrial water balance components.
4. Describing the land-precipitation feedback measures for the Mathioya-Sagana subcatchment and its surrounding.

I.4 Innovation

The innovations of this PhD dissertation are as follows:

- Besides the available physical parameterizations schemes in the WRF model, this PhD study provides an extension of the work of (e.g., Pohl *et al.*, 2011; Endris *et al.*, 2013) in terms of the impact of land-use data and the model's horizontal resolution in reproducing precipitation and temperature in the TRB. It is the first time the WRF model is applied for the TRB and evaluated using both gridded and station data.
- Successful calibration of the uncoupled WRF-Hydro model for a subcatchment in the upper TRB. Further application of the WRF and coupled WRF-Hydro in simulating the joint atmospheric-terrestrial water balance. The coupled modeling system is applied for a relatively long period of 4 years in this region for the first time.
- Development, implementation and application of a tool to analyze the atmospheric water balance from the model output.

I.5 Study area

This study focuses on the Tana River basin (TRB) of East Africa. The basin lies between the latitudes 0° 0' 53" S and 3° 0' 00" S and between the longitudes 37°00' 00" E and 41° 00' 00" E (see Figure I-1) with a total catchment area of about 126,000 km² (Knoop *et al.*, 2012). It is the third largest out of five drainage basins in Kenya and transverses more than ten of Kenya's administrative counties. It is characterized by a diverse network of meteorological stations (shown in red dots in Figure I-1).

According to Knoop *et al.* (2012), the TRB is divided into three parts: the upper, middle and lower, with precipitation characteristics primarily influenced by topography. The areas around the upper TRB, middle TRB and lower TRB are marked as UT, MT and LT respectively (Kerandi *et al.*, 2016).

The outer boundary of the study area, which encompasses the whole TRB, is used for analysis towards achieving the first objective of this study. The small blue rectangle circumscribes the delineated boundaries of Mathioya-Sagana subcatchment (MSS) marked by the red contour. The MSS and surrounding are utilized for analysis of results towards achieving objectives 2 to 4. More specific details for this region will be presented in Chapter IV.

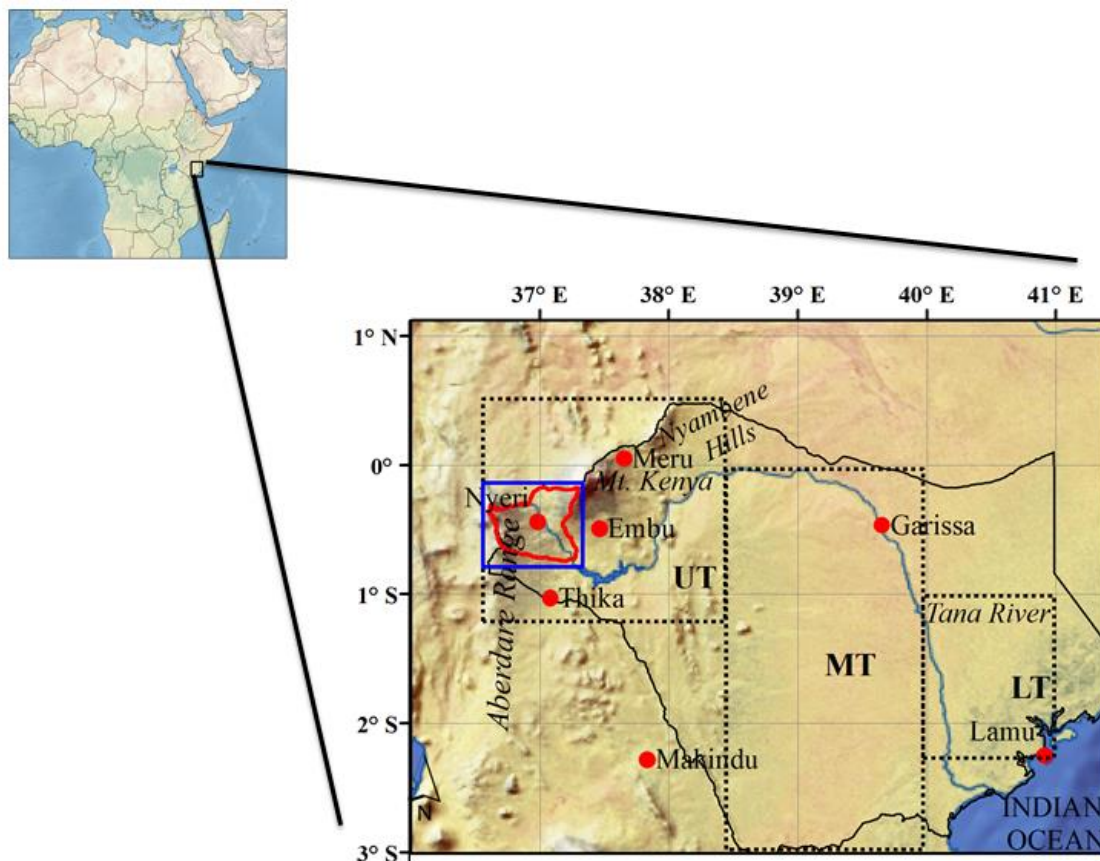


Figure I-1: Map of the study area and location of meteorological stations (Nyeri, Embu, Meru, Thika, Garissa, Makindu, Lamu) marked as red dots. Inset black boundary marks the Tana River basin (TRB), Kenya; blue rectangular shows the Mathioya-Sagana subcatchment (MSS; red contour) and surrounding. The dotted black lines mark the arbitrary boundaries of upper, middle and lower TRB depicted as UT, MT and LT respectively

The TRB hosts Mount Kenya whose altitude is approximately 5200 m.a.s.l., the Aberdare Ranges which is about 4000 m.a.s.l. and the Nyambene Hills which is approximately 2500 m.a.s.l. among the high elevated regions. There is also the Tana River, the longest river in Kenya (approximately 1014 km). The river has its source in the foot hills of Mount Kenya and the Aberdare Ranges and traverses the entire TRB before discharging to the Indian Ocean.

1.5.1 Hydroclimatology of the study area

Hydroclimatology is viewed as an intersection of climatology and hydrology, dealing with energy and moisture exchanges between the atmosphere and the Earth's surface and energy and moisture transport by the atmosphere (Shelton, 2009). This section

focuses on precipitation and discharge as examples of elements used to define the hydroclimatology of the study area.

The topographic features highlighted in Section I.5, the Tana River and also the Indian Ocean influence the basin's hydroclimatology (Kitheka *et al.*, 2005; Schmocker *et al.*, 2015). Like most areas in East Africa, the TRB experiences a bimodal rainfall seasonal pattern (Kitheka *et al.*, 2005; Oludhe *et al.*, 2013). The first season, locally known as the "long rains", falls during the months of March to May (MAM), while the second season, locally known as "short rains", falls during the months of October to December (OND). As the Equator straddles Kenya, these seasons result from the north-south oscillation of the Inter-Tropical Convergence Zone (ITCZ) (e.g., Indeje *et al.*, 2000; Nicholson, 1996, 2014; Ogallo, 1988). During the time when ITCZ is located in the south of the equator, it is associated with the OND season and, when north of the equator, it occurs during the MAM season. The movement of the ITCZ is considered to be as a response in variation of the Indian Ocean sea-surface temperatures (SSTs) which is characterized by either El Niño Southern Oscillation (ENSO; greater than average rainfall) or La Niña (drier than average rainfall) events (McSweeney *et al.*, 2010). As the TRB is characterized by complex terrain, it has its climate changing over short distances (Nicholson, 1996). Other than the aforementioned features, there are further factors that control the precipitation and hence climatology of this region that are also global than necessarily local (Nicholson, 1996; Indeje *et al.*, 2000; Schreck and Semazzi, 2004). The annual average precipitation lies between as low as 300 mm and 1300 mm though it can be more especially in the locality of the Aberdare Ranges and Mount Kenya which are high elevated areas (Kerandi *et al.*, 2016). This is also confirmed in Figure I-2 in which the distinct spatial pattern of average annual precipitation over the TRB is shown. Elevation-rainfall relationships do not apply to the areas around the coastal regions (area around Lamu), which are seen to receive rainfall amounts similar to that of areas around Thika. In general however, the precipitation in the entire basin is associated with elevation (Knoop *et al.*, 2012), defining clear areas with particular amounts of precipitation. Details specific to the individual TRB stations' precipitation and temperature climatology are presented later in Section III.2.

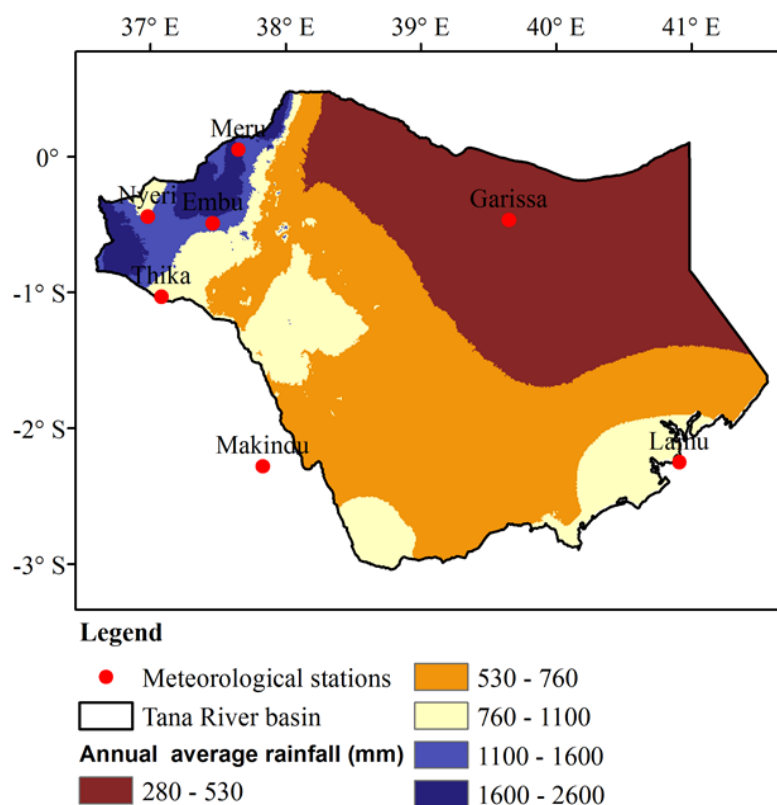


Figure I-2: Average annual rainfall for the Tana River basin (TRB) sourced from World Resource Institute (GIS) archives (<http://www.wri.org/resources/data-sets/Kenya-gis-data>, downloaded on 13th April, 2016). The rainfall data is averaged for 50 years (1950-2000) at a spatial resolution of 1 km and is sourced from station data

In terms of river discharge, the TRB experiences two high river flows during the year that occur in the months of April to June (AMJ) and October to December (OND) separated by two low flows in the remainder of the other months (Oludhe *et al.*, 2013). The peak flows occur in the months of May and November, respectively (Kitheka *et al.*, 2005). This shows that the stream flow pattern has a direct response to the rainfall storms in this region. Besides, the seasonal distribution of rainfall leads to seasonal river flows. All factors that influence precipitation in this region directly or indirectly impact on stream flow.

I.6 Structure of the thesis

This thesis is organized into seven major chapters. Chapter I provides the general introduction, the basics of the study area, related RCMs studies in respect to this study, the objective (s) and innovation. Chapter II presents the methodology and observational datasets. Here the WRF-only and coupled WRF-modeling systems are defined to-

gether with the parameterizations selected for this study. Further, the observational datasets, both the station and global datasets, are presented. Before discussing the water balance computation techniques, the calibration procedure and results of the uncoupled WRF-Hydro model is provided. Chapter III presents the WRF-only sensitivity and performance results for the outer domain D1, at 25 km and 50 km horizontal resolution. In Chapter IV, the WRF-only and coupled WRF-Hydro performance results for the inner domain D2 at 5 km horizontal resolution are provided focusing on precipitation and discharge. The terrestrial water balance (TWB) and atmospheric water balance (AWB) results are elaborated in Chapters V and VI respectively. Besides, in Chapter VI the land-atmospheric interaction is provided. Last but not least, major conclusions for this thesis along with the outlook are featured.

II Description of the numerical models, datasets and methods

The model-based findings of this thesis are obtained from the WRF stand-alone and the coupled WRF-Hydro modeling systems. A brief theoretical background on these models, experimental details, evaluation datasets and methodology are described in the following sections.

II.1 WRF modeling system

The WRF model is a non-hydrostatic, mesoscale numerical weather prediction and atmospheric simulation system. It is designed with a flexible code and offers several physical options (parameterizations) to choose from.

The parameterizations are majorly classified into microphysics (*mp_physics*), cumulus or convection (*cu_physics*), surface layer (*sf_sfclay_physics*), land surface (*sf_surface_physics*), planetary boundary layer (*pbl_physics*) and atmospheric longwave/shortwave radiations (*ra_lw_physics/ra_sw_physics*). As indicated earlier, the parameterizations take care of the subgrid physical processes and are known to work interactively besides each playing its own role (Warner, 2011). Details of these parameterizations are available e.g., in Skamarock *et al.*, 2008; Fersch, 2011; Warner, 2011. An overview is given below.

The *mp_physics* describes all the cloud processes and the hydrometeors that lead to the generation of various forms of precipitation. The *cu_physics* schemes are responsible for subgrid scale effects of convective and/or shallow clouds. They define convection in the right place, and at the right time and with the correct evolution and intensity. They are ignored when a model can resolve the convective processes itself preferably at ≤ 5 km grid. Planetary boundary layer processes influence the free atmosphere above. The *pbl_physics* are 1-dimensional and are considered to determine the flux profiles within a well-mixed boundary layer and the stable layer. They eventually provide atmospheric tendencies of temperature, moisture, and horizontal momentum in the entire atmospheric column. The *ra_lw_physics* and *ra_sw_physics* are responsible for atmospheric heating due to radiative fluxes and surface downward longwave and shortwave radiation, respectively for the ground heat budget. The sun is the main driver of all atmospheric processes. The interaction of this energy and the atmosphere or surface is at molecular level and too complex to simulate explicitly.

The *sf_sfclay_physics* and the *sf_surface_physics* provide no tendencies, only the stability-dependent information about the surface layer for the land-surface and the *pbl_physics*. The *sf_sfclay_physics* determine friction velocities and exchange coefficients that enable the calculation of the surface heat and moisture fluxes by the LSMs and surface stress in the *pbl_physics*. The LSMs provide heat and moisture fluxes over land points and sea-ice points after utilizing information from the other schemes. They update the land's state variables: ground (skin) temperature, soil temperature profile, soil moisture profile, snow cover, and canopy properties.

Besides the above highlighted parameterizations, the WRF model also offers an option of selecting between two land use categories or classifications: the *U.S Geological Survey* (USGS, 24 classes; Anderson *et al.*, 1976) and the *Moderate Resolution Imaging Spectroradiometer* (MODIS, 20 classes; Friedl *et al.*, 2002). The USGS based land use dataset was developed using the global 1-km resolution Advanced Very High Resolution Radiometer (AVHRR) satellite sensor from April 1992 to March 1993 (Anderson *et al.*, 1976; Liang *et al.*, 2005). The MODIS based land use dataset is also at 1-km resolution but uses the *International Geosphere-Biosphere Program* (IGBP) classification and was defined in 2001-2002 (Friedl *et al.*, 2002).

II.2 WRF-Hydro modeling system

The WRF hydrological modeling extension package (WRF-Hydro; Gochis *et al.*, 2015) is a development of the 1-dimensional Noah LSM of WRF, purposed to account for land surface states and fluxes and to provide physically consistent land surface fluxes and stream channel discharge information for hydro-meteorological applications. One particular enhancement of the WRF-Hydro system is the routing of both infiltration capacity excess and saturated subsurface water. This forms the basis of its physical process options (routing processes), which include surface overland, subsurface, channel and conceptual baseflow (bucket model).

The details of the routing processes are available in Gochis *et al.* (2015). A brief statement for each is provided here.

Subsurface lateral flow is described as exfiltration from a supersaturated soil column. The soil column is said to be supersaturated when it possesses a positive subsurface moisture flux, which when added to the existing soil water content is in excess of the total soil water holding capacity of the entire soil column. In this state, it is added to

infiltration excess from the land surface model, which has to update the value of surface heads before routing of overland flow.

Overland flow is represented using a fully-unsteady, explicit, finite-difference, diffusive wave formulation with either a two dimensional or a steepest descent approach. The continuity equation for an overland flood wave is combined with the diffusive wave formulation (the diffusive wave formulation accounts for backwater effects hence allowing flow on adverse slopes) of the momentum equation.

The **channel routing** processes result as overland flow pass a portion of the surface water in excess of the local ponded water retention depth (“RETDEPRT”). It allows the one-dimensional, distributed routing of streamflow across the domain on a pixel-to-pixel basis. The channel network has a trapezoidal geometry defined by side slope, depth of water in the channel, bottom width and roughness coefficients (which are part of the Strahler stream order functions). The stream order increases towards the basin outlet. The bottom width and the initial depth of water of the channel increases with increase in stream order, while the side slope and the Manning’s roughness’s coefficients decrease with increase in stream order (Gochis *et al.*, 2015; Givati *et al.*, 2016). The channel routing is input to the high resolution terrain routing grid file. Currently no over-bank flow is simulated which means that the channel flow is accomplished through a 1-dimensional, variable time stepping wave formulation (Gochis *et al.*, 2015; Senatore *et al.*, 2015). There are two options in which channel flow routing can be implemented, i.e., 2-dimensional (CAS2CD) and 1-dimensional (steepest descent or “D8”). The diffusive wave channel routing formulation in CASC2D simulates backwater effects and is relevant in streams with very flat or adverse slopes (Julien, Saghafian and Ogden, 1995).

The WRF-Hydro system also contains a simple **lake or reservoir routing** process. This is achieved through a simple mass balance, which allows for an estimate of the inline impact of small and large reservoirs on hydrologic response. In WRF-Hydro, lakes and reservoirs are differentiated conceptually, i.e., reservoirs contain both orifice and weir outlets for reservoir discharge, while lakes only contain weirs. Fluxes into a lake/reservoir object occur through the channel network and when surface overland flow intersects a lake object.

The **baseflow** parameterization, which is useful for long-term streamflow simulations, is linked to WRF-Hydro through the discharge of “deep drainage” from the land surface

soil column. It uses spatially-aggregated drainage from the soil profile as recharge to a conceptual ground water reservoir. The unit of spatial aggregation is often taken to be that of a catchment or sub-basin within a watershed where streamflow data is available for the sub-basin. Each sub-basin has a groundwater reservoir (“bucket”) with a conceptual depth and associated volumetric capacity. WRF-Hydro uses either a direct output-input relationship or an exponential storage-discharge function for estimating the bucket discharge as a function of a conceptual depth of water in the bucket. In our case, we have the delineated catchment hypothesized as one. Estimated baseflow discharge from the bucket model is then combined with lateral inflow from overland flow and is input directly into the stream networks as “stream inflow”. The total basin baseflow flux to the stream network is equally distributed among all channel pixels within a basin.

The model can be used both in an uncoupled (stand-alone or offline) mode as well as in a coupled mode to an atmospheric model (in present case, the WRF model). In uncoupled mode i.e., no online interaction with WRF atmospheric model, but the Noah-LSM acts like any land surface hydrological modeling system. In the event that all the above routing processes are activated, it is considered a moderately computationally intensive modeling system with respect to other physics-based environmental modeling system that may include weather, climate, catchment hydrology and other geophysical fluid dynamics models (Gochis *et al.*, 2015). In this mode, the model requires meteorological forcing data prepared externally and provided as gridded data to drive the simulations. Details of forcing data for the uncoupled WRF-Hydro are presented in Section II.6.

II.3 Coupling of WRF and WRF-Hydro

The coupling of an atmospheric and a hydrological model is considered to take advantage of the nesting capabilities of the atmospheric model which can be nested into a global model to allow large-scale integration (Bronstert *et al.*, 2005). The nesting enables the hydrological model to account for the spatial heterogeneity of hydrology and atmospheric processes. Atmospheric-hydrological coupling can be achieved through one-way, two-way or integrated (integrative) modeling (Bronstert *et al.*, 2005). The one-way coupling is the most basic of these in which the coupling drives the hydrological models by outputs of atmospheric models. It can be considered as two LSMs describing the same land surface processes differently, where the modeling system does not

allow feedback between the atmospheric and the hydrological model (Zabel and Mauser, 2013). In a two-way coupling, the feedback is allowed which leads to production of subgrid scale land-surface fluxes, and generally an improvement of model simulations (Zabel and Mauser, 2013).

Figure II-1 summarizes the various WRF-Hydro components and the coupling to the WRF model. The hydrological component, WRF-Hydro, is called directly from WRF in the WRF surface driver module. This is accomplished at the coupling interface by the WRF-Hydro coupling interface module. The interface serves to pass data, grid and time information between WRF and WRF-Hydro. The WRF-Hydro components map data and sub-component routing processes (e.g., land and channel routing). Upon completion of these processes the data is remapped back to the WRF-model (by the WRF-Hydro driver) through the coupling interface. The routing time step is set in accordance with the routing grid spacing (Gochis *et al.*, 2015).

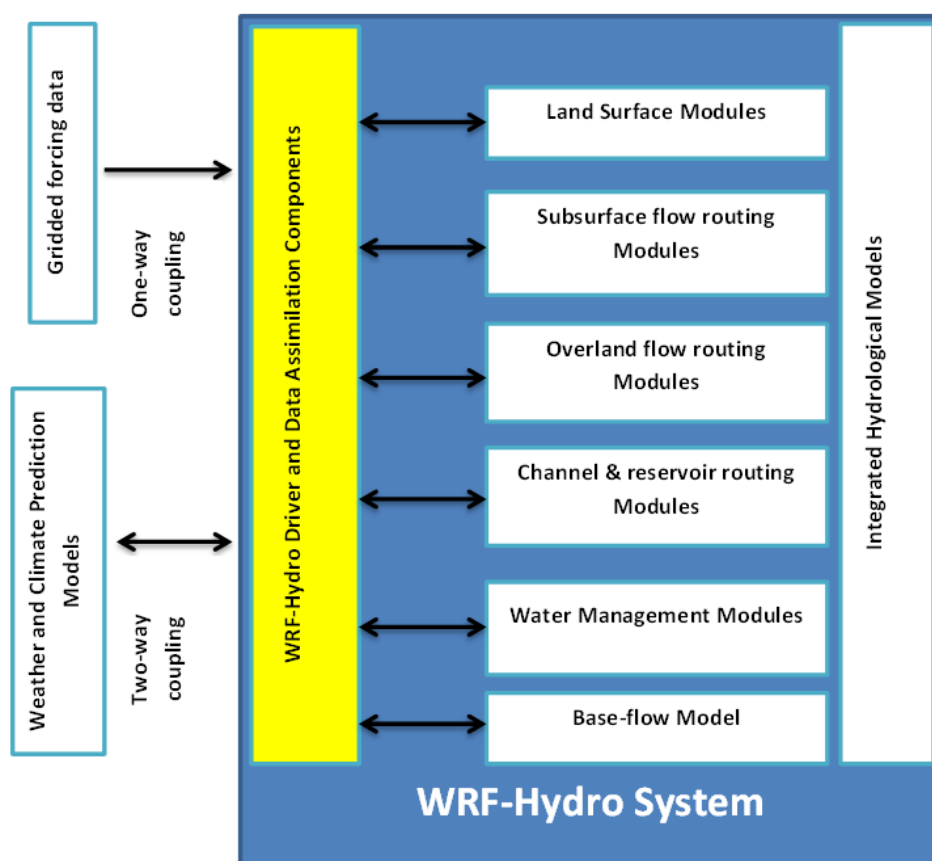


Figure II-1: Sketch of the WRF-Hydro modeling system showing the various components (Gochis *et al.*, 2015).

In its coupled mode, WRF-Hydro generally leads to an improved simulation of the full water cycle with its capability of permitting atmospheric, land surface and hydrological processes from available physics options. The physics options are discussed in Section II.2.

II.4 Model configurations/parameterization

Model configuration is depended on the geographical location and the purpose of the study. This involves designing the correct model domains at the WRF preprocessing stage (e.g., identifying the resolution (horizontal and vertical), the parameterizations, etc.). In this section, the model domain details for the WRF-only which are also common to the coupled WRF-Hydro are discussed. The details specific to the WRF-Hydro part of the modeling system are highlighted.

Model domains and experimental details

Two one-way nest domains with the outer domain D1, at 25 (50) km and inner domain D2, at 5 km horizontal resolution are considered for this study. D1 is defined with 140×120 (70×60) grid points in east-west and north-south directions extending 12°S - 13°N ; 22° - 53°E whereas D2 is defined with 121×121 grid points in east-west and north-south directions covering an area ($3^{\circ}3'\text{S}$ - $2^{\circ}17'\text{N}$; $34^{\circ}33'$ - $39^{\circ}54'\text{E}$). D1 covers the whole of East Africa while D2 encompasses the whole of upper TRB (Figure II-2). For purposes of hydrometeorological simulations, D2 is additionally coupled with routing process at 500 m resolution with 1200×1200 grid points in east-west and north-south directions. The domain details specific to D2 are explained in Section II.4.

Different parameterizations are applied to D1 at 50 km horizontal resolution in order to select the suitable combinations for both D1 at also 25 km horizontal resolution. The Kain-Fritsch (KF; Kain, 2004), Grell Freitas (GF; Grell and Freitas, 2014) and Bett Miller Janjic (BMJ; Janjic *et al.*, 2000; Janjić, 1994) are the *cu_physics* selected for testing in first set of sensitivity experiments. The KF has been used in several studies in East Africa studies (e.g. Endris *et al.*, 2013; Pohl *et al.*, 2011; Riddle and Cook, 2008). The BMJ, which is a column moist adjustment scheme, has a discernable behavior and can easily be evaluated compared to other convective schemes (Stensrud, 2007). The GF, an improvement of the Grell-Devenyi ensemble scheme, is considered for its capability of cloud resolving scales. Two *mp_physics* i.e., WRF Single Moment 6-class (WSM6; Hong *et al.*, 2006) and Lin *et al.* scheme (Lin *et al.*, 1983) are also selected for compar-

ison. WSM6 and Lin *et al.* schemes are considered suitable for high resolution simulations and have the same processes capabilities for ice, snow and graupel. The Asymmetric Convective Model version 2 (ACM2; Pleim, 2007), is the only *pbl_physics* that completes the set of major parameterizations. It is applied for the subgrid-scale vertical mixing. ACM2 is characterized by non-local upward and local downward mixing and performs well for meteorological parameters investigated. The *ra_sw_* and *ra_lw_physics* are implemented by the New Goddard scheme, which is efficient and has multiple bands and ozone from climatology (Chou and Suarez, 1999). The Noah LSM (Chen and Dudhia, 2001) is used for the land surface processes. A total of six configurations (or experiments) were carried out on D1 at 50-km horizontal resolution as a preliminary step in order to identify which among them reproduces the observed precipitation and temperature best. Details are described in Section III.1. The suitable configuration is selected for further sensitivity experiments to investigate the impact of MODIS and USGS land use classifications and increasing horizontal resolution from 50 km to 25 km on simulated precipitation and temperature.

All experiments stated in preceding paragraphs and in all subsequent experiments use 40 vertical levels up to 20 hPa (approximately 26 km vertical height above the surface). The model integration is 200 (100) seconds for D1 at 50 (25) km horizontal resolution. The ERA-Interim reanalyses data from the European Centre for Medium-Range Weather Forecasts (ECMWF) provide the initial and lateral boundary conditions (Dee *et al.*, 2011) for the WRF simulations which are archived after every 24 hours.

The simulations are initialized on November 1st, 2010 and ran continuously till December 31st, 2014. The first two months are considered as spin-up and are excluded from the evaluation. Nesting and domain sizes and corresponding elevations are shown in Figure II-2.

D1 is further utilized for WRF stand-alone sensitivity experiments based on the best selected combinations of parameterizations at two horizontal resolution (50 km and 25 km) and two land use representations (MODIS and USGS). Details are provided in Sections III.4 and III.5.

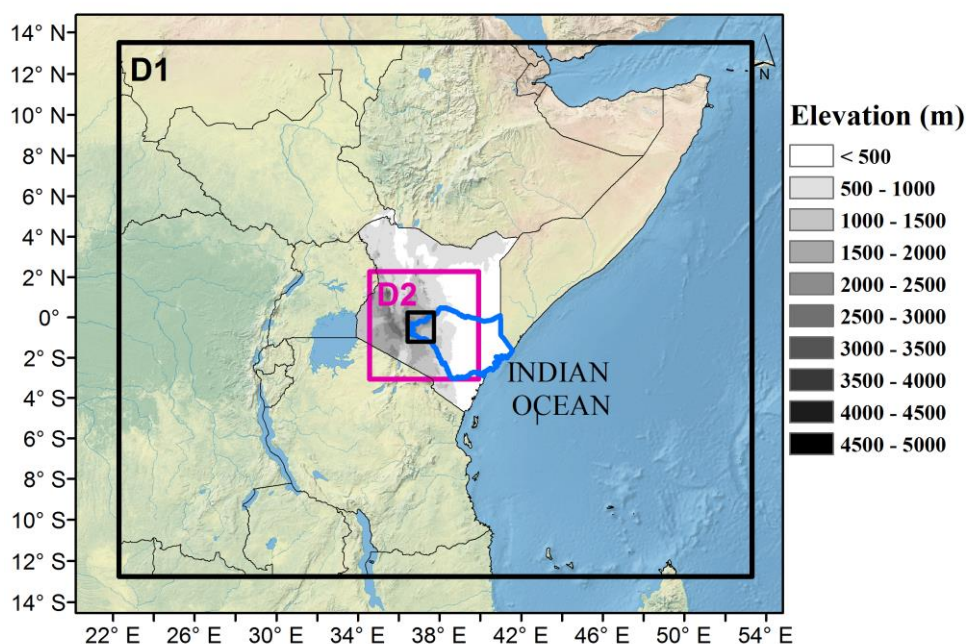


Figure II-2: Model domains at 25 km and 5 km horizontal resolution (D1 in black; D2 in pink). Blue contour marks the TRB boundary and the inset black box in D2 defines part of the Mathi-o-ya Sagana subcatchment. The elevation (m) that covers most of D2 is processed from the Shuttle Radar Topography Mission (SRTM) at 3 arc-second (90-metres) resolution; Source: <http://www.wri.org/resources/data-sets/kenya-gis-data#elevation>

Domain details specific to WRF-Hydro

Both WRF-Hydro and WRF components of the coupled modeling system share the same physics parameterizations. D2 is configured with additional settings specific for the hydrological simulations at a high resolution terrain grid.

The aggregation factor (AGGFACTR), one important option that determines how the model state and flux variables are passed to/from the LSM grid (i.e. the 5 km WRF model grid) to the high resolution terrain grid (for this study 500 m) via a disaggregation/aggregation scheme, is set to 10. Details about AGGFACTR are described in Gochis and Chen (2003). The AGGFACTR links onto the routing routines. The state variables involved in the disaggregation include maximum soil moisture content for each soil type, infiltration excess, lateral saturated hydraulic conductivity for each soil type and soil moisture content for each soil layer. To preserve the structure of the spatial variability of soil moisture content on the sub-grid from one model time step to the next, simple, linear sub-grid weighting factors are assigned. These values indicate the

fraction of the of total land surface model grid value that is partitioned to each sub-grid pixel (Gochis and Chen, 2003; Gochis, *et al.*, 2015; Senatore *et al.*, 2015).

II.5 Observational datasets

This section highlights the different datasets that are used for calibration, evaluation and validation of the simulation results at various stages of the study. They include station data for rainfall, discharge and temperature and satellite and gridded datasets for precipitation, temperature and evaporation.

Station observed and gridded rainfall data

The **station rainfall** data is obtained from the Kenya Meteorological Department (KMD) and the Water Resource Management Authority (WRMA). The KMD data is for the stations Nyeri, Meru, Embu, Thika, Garissa and Lamu spread unevenly over the TRB (see Figure I-1). Two WRMA stations' data (Murang'a and Sagana), located in upper TRB, is also used in this study (see Section IV.2.1). The two WRMA stations and Nyeri are the only stations located in the Mathioya Sagana sub catchment.

The **satellite estimates of Tropical Rainfall Measuring Mission** (TRMM, 3B42 v7 derived daily at 0.25° horizontal resolution, 1998-2015; Huffman *et al.*, 2007), is used in this study for model evaluation, both spatially and temporally. The daily accumulated TRMM product (beginning at 00Z and ending 21Z; unit: mm) is derived from the 3-hourly product that has a spatial coverage of a latitude band 50°S to 50°N. It is prepared and distributed by the NASA GES DISC, as a value added product. The source and details of its preparation is available at http://disc.sci.gsfc.nasa.gov/datacollection/TRMM_3B42_daily_V7.html. TRMM 3-hourly 0.25° is used in the calibration of the uncoupled WRF-Hydro as highlighted in Section II.6.

The **Climate Hazards Group Infrared Precipitation with Stations** (CHIRPS; chirps-v2.0 at 0.05° horizontal resolution; 1981-near present; Funk *et al.*, 2015), a recent global dataset and like TRMM has a spatial coverage spanning 50°S-50°N (and all longitudes). It is based on satellite imagery with in-situ station data and has a temporal resolution of daily, pentad and monthly. It is designed as a suitable alternative for data sparse regions that depend on convective rainfall. Details of this dataset is available at: <http://chg.geog.ucsb.edu/data/chirps/>

The **gridded Climate Research Unit** (CRU v3.23, monthly at 0.5° horizontal resolution, 1901-2014; Harris *et al.*, 2014) spans for the period 1901 to 2014 and supersedes all other previous versions. The dataset is prepared at the University of East Anglia and is based on an archive of monthly mean temperatures provided by more than 4000 weather stations distributed all over the world. This product undergoes routine updates using monthly climate archives from the World Meteorological Organization (WMO) in collaboration with the US National Oceanographic and Atmospheric Administration (NOAA, via its National Climatic Data Center, NCDC). It is widely used for climate studies and consists of a number of variables that include cloud cover, diurnal temperature range, frost day frequency, precipitation, daily mean temperature, monthly average daily maximum and minimum temperature, vapour pressure, potential evapotranspiration and wet day frequency. In the present study, CRU temperature data is also used for model evaluation. Details and source of this data is available at:

<http://catalogue.ceda.ac.uk/uuid/3f8944800cc48e1cbc29a5ee12d8542d>.

Station temperature and gridded temperature data: Observed station temperature with complete records is available for only four of the meteorological stations (named in Section 2.5) i.e., Nyeri, Meru, Thika and Lamu. The data is provided in daily resolution of both minimum and maximum temperature.

The CRU gridded monthly mean, minimum and maximum temperature at horizontal resolution (0.5 x 0.5 degree) grids is used to evaluate the model simulations. The details of CRU are outlined in the previous paragraph.

Discharge data

Hydrological data is not readily available in most river basins of the country because of many challenges that include poor collection methods, theft of the gauges and insecurity. The daily discharge records available for this study is obtained from the Tana Rukanga's RGS 4BE10. It spans for the entire period of study (2011-2014), however with two months missing data in 2013.

Evaporation data

The ***Global Land Evaporation Amsterdam Model*** datasets version 3 (GLEAM v3.0; horizontal resolution, 0.25°; Miralles *et al.*, 2011) is additionally used to validate the simulated evaporation. GLEAM v3.0 estimates different components of terrestrial evapotranspiration based on satellite observations: transpiration, interception loss, bare-soil evaporation, snow sublimation, and open water evaporation. It is available in three datasets of different forcing and spatio-temporal coverage. All cover the years 2011-2014 which is the focus period for this study. Details of GLEAM are available at: www.gleam.eu.

II.6 Uncoupled WRF-Hydro calibration

This section focuses on the forcing data, procedure and parameter selection related to the calibration of the uncoupled WRF-Hydro. The calibration results are also discussed. The calibration forms the first step before application of the coupled WRF-Hydro modeling system for the region of the study.

Forcing data/Atmospheric model data

The following forcing data options are available for the uncoupled WRF-Hydro: High-Resolution Land Data Assimilation System (HRLDAS) hourly, hourly with specified precipitation and minute format input files, WRF model output and WRF model output with specified precipitation, the idealized and idealized with specified precipitation. Details of preparation of these data formats or options are available at Gochis *et al.* (2015). An overview is presented here.

The HRLDAS options uses a combination of observed and analyzed meteorological forcing (precipitation, solar and longwave radiation, and surface wind, moisture, temperature) to drive a land-surface model to simulate the evolution of land surface states (e.g., soil moisture, temperature, snow, etc.). The options must satisfy specific attributes including the correct name and correct units. In the present work the HRLDAS-hourly option is chosen.

The forcing data to drive the uncoupled WRF-Hydro include the hourly incoming shortwave radiation (SWDOWN) and longwave radiation (LDOWN) measured in W/m², specific humidity (Q2D) in kg/kg, air temperature (T2D) in K, surface pressure (PSFC)

in Pa, near surface wind: u- (U2D) and v- (V2D) in m/s. In the present study, these datasets are extracted from WRF model output runs. The precipitation (RAINRATE) in mm/s is processed from TRMM 3-hourly precipitation dataset using Climate data and netCDF operators (CDO and NCO) algorithms to distribute and duplicate it equally for each hour in the 3 hours interval. This is necessary as all variables are intended to be of 1-hourly temporal resolution in this study. The RAINRATE is then regridded to the WRF grid in order to be similar with other variables extracted from WRF output. A sample of the file header showing these variables and associated details is provided in Appendix A: Meteorological forcing data .

Parameters selection

There are a number of parameters in the Noah LSM which are associated with large uncertainties that impact hydrological model outputs. In view of this, model calibration is necessary before its application (Gochis *et al.*, 2015). As an illustration, there are the general or miscellaneous parameters like *refdk* which is used to compute the runoff parameter *kdt*, the surface runoff parameter *refkdt*, the soil heat capacity *csoil* etc. which all are associated with the whole model domain. There are also the vegetation parameters that are associated with land use or land cover, whereas the soil parameters describe the various soil physical characteristics.

There are further parameters which are besides either the general, vegetation or soil parameters which are associated with the high-resolution terrain grid development. These include the scaling parameters, i.e. the overland flow roughness (OVROUGHRTFAC) and the surface retention depth (RETDEPRTFAC).

In this study, four parameters (REFKDT, OVROUGHRTFAC, Manning's roughness coefficient associated with the channel (MannN), and RETDEPRTFAC) are selected in order to analyze their sensitivity to the simulated discharge. The REFKDT has a feasible range of between 0.1 and 10 with a default value 3.0, while the RETDEPRTFAC has its default value of 1.0 (Rosero *et al.*, 2009; Gochis *et al.*, 2015). These two control the amount of runoff which is reflected in the hydrograph volume. On the other hand, the OVROUGHRTFAC has its default value of 1.0. Together with the MannN, they are associated with controlling the overland flow and hence the hydrograph shape (Yucel *et al.*, 2015).

Calibration procedure

The procedure adapted for calibration of uncoupled WRF-Hydro is motivated by the work of Yucel *et al.* (2015), which is otherwise referred to as “stepwise approach”. It is a manual calibration approach that is considered to minimize the number of model runs and cut down excessive computational time which may otherwise be encountered with automatic calibration. The calibration period for the uncoupled WRF-Hydro is based for the whole of 2012. One year calibration is considered long enough to evaluate the basic parameter sensitivities (Senatore *et al.*, 2015).

In a stepwise approach, one parameter is varied at regular interval while the others are held constant until its optimal value is obtained based on the preferred objective criteria, the appearance and shape of the hydrograph. In this work, the Nash-Sutcliffe efficiency (NSE) and RMSE-observations standard deviation ratio (RSR) objective criteria are selected. NSE is one of the traditional measures that check the correspondence between modeled and observed discharge. It can be used to indicate how well the plot of observed versus the modeled discharge fits the 1:1 line (Moriasi *et al.*, 2007). It ranges from $-\infty$ to 1 whereby values between 0 and 1 show an acceptable performance, while values ≤ 0 shows that the mean of observed data is a better predictor than the modeled thus the results are considered unacceptable (Moriasi *et al.*, 2007). RSR standardizes the root mean square error (RMSE) using the observations standard deviation incorporating an error index statistics and a scaling/normalization factor. The optimal value is 0 and low values mean low RMSE and thus better model simulation performance (Moriasi *et al.*, 2007). A statement of the formulae of these objective criteria is presented in Appendix B: Statement of the objective criteria and other statistical measures.

REFKDT is calibrated first with its values chosen between 0.6 and 6.0 within the feasible range and at a regular interval, followed by RETDEPRTFAC values between 0.0 and 5.0. The OVROUGHRTFAC and the MANN then follow in that order. The OVROUGHRTFAC is evaluated for values within the range of 0.0 to 1.0 by an increment of 0.2. The range 0 to 1 is considered modest as it is neither high nor low to maintain the Manning’s roughness’s equation performance stable for solving surface runoff (Yucel *et al.*, 2015). Besides, it is recommended that values less than the default value be considered during calibration for the stability of the model. The default Manning’s roughness coefficients can be amplified by a constant scaling factor through addition,

multiplication or division by a constant scaling factor that applies to all coefficients of all stream orders. In this study multiplication is considered in which case the scaling factor is considered as the calibration values or parameters (Yucel *et al.*, 2015). The MANN is varied within the range of 0.4 and 2.0 with an increment of 0.2.

Calibration results

The resulting hydrographs from variation of the REFKDT is as shown in Figure II-3. The highest peaks are observed for REFKDT = 1.0 followed by those of REFKDT = 2.0 with REFKDT = 6.0 having the smallest peaks. The volume of the modeled discharge is a manifestation of change in REFKDT and more so at the daily resolution.

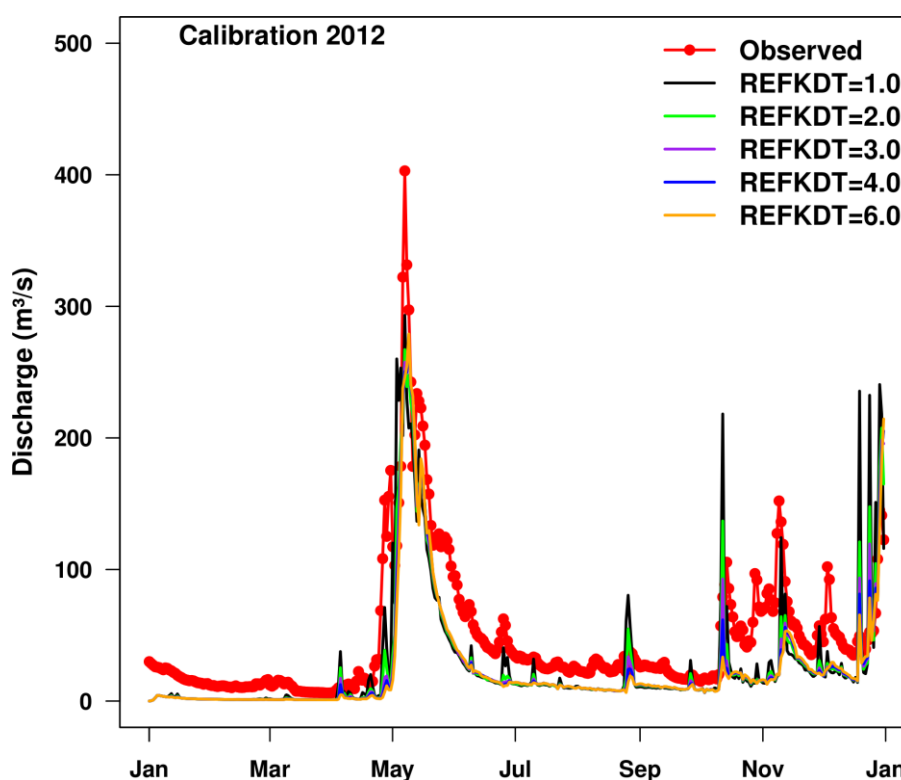


Figure II-3: Time series of daily observed and simulated discharge at Tana Rukanga's RGS 4BE10 in response to variation of the surface runoff parameter (REFKDT) for 2012

The annual mean of modeled discharge for the year 2012 at each change of the REFKDT show a decrease with increase in REFKDT. For instance, at REFKDT = 1.0 the annual mean discharge modeled is 28.0 m³/s, REFKDT = 3.0 with 24.6 m³/s and that corresponding to REFKDT = 6.0 which is 23.7 m³/s. However, based on the computed statistics, as shown in Table II-1, the REFKDT = 1.0 does not post better statis-

tics compared to either REFKDT = 2.0 or REFKDT = 3.0 (default). Based on the NSE and RSR, REFKDT = 2.0 is considered the better option and is held constant for the evaluation of the RETDEPRTFAC parameter.

Table II-1: Selected objective criteria (Nash-Sutcliffe efficiency NSE and RMSE-observations standard deviation RSR) between simulated and observed discharge at Tana Rukanga's RGS 4BE10 based on the infiltration-runoff parameter REFKDT, retention factor RETDEPRTFAC, overland flow roughness scaling factor OVROUGHTFAC and the Manning's roughness coefficients MannN. Experiments in *italics bold* show the selected parameters' value and the best NSE and RSR after calibration

<u>REFKDT</u>									
Range	0.6	0.8	1.0	2.0	3.0	4.0	6.0		
RSR	0.86	0.76	0.71	0.65	0.65	0.65	0.66		
NSE	0.25	0.41	0.49	0.58	0.58	0.57	0.56		
<u>RETDEPRTFAC</u>									
Range	0.0	1.0	2.0	3.0	4.0	5.0			
RSR	0.65	0.65	0.650	0.65	0.95	0.65			
NSE	0.58	0.58	0.58	0.58	0.58	0.58			
<u>OVROUGHTFAC</u>									
Range	0.1	0.2	0.4	0.6	0.8	1.0			
RSR	0.70	0.69	0.64	0.64	0.65	0.65			
NSE	0.51	0.53	0.59	0.58	0.58	0.58			
<u>MannN</u>									
Range	0.4	0.6	0.8	1.0	1.2	1.4	1.6	1.8	2.0
RSR	0.80	0.68	0.65	0.64	0.64	0.63	0.62	0.62	0.62
NSE	0.37	0.54	0.58	0.59	0.59	0.60	0.61	0.62	0.61

Figure II-4 shows the response of the hydrographs on variation of the RETDEPRTFAC scaling parameter. The hydrographs are all similar which makes it difficult to distinguish which of the retention scaling factor has a more or less impact on the hydrograph vol-

ume. Thus the modeled discharge remains the same regardless of change in RETDEPRTFAC scaling factor.

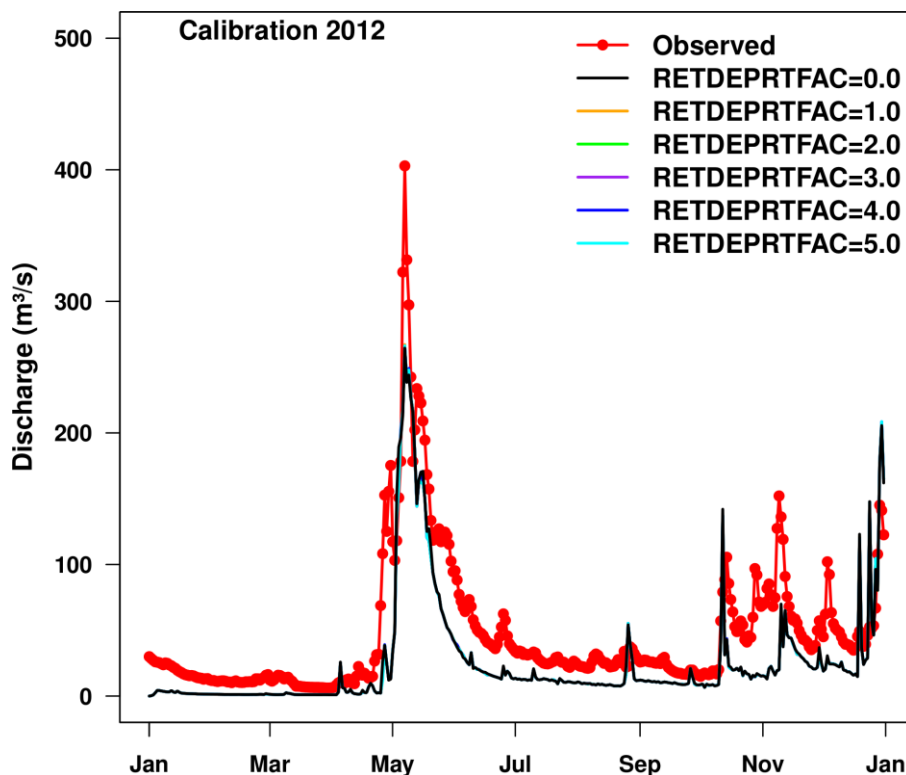


Figure II-4: Similar to Figure II-3 but shows sensitivity to the retention depth parameter, RETDEPRTFAC

The statistics corresponding to different values of RETDEPRTFAC (Table II-1) are in agreement with the graph output as the scores are very close to each other. However RETDEPRTFAC = 0.0 give slightly better results with NSE= 0.58 and RSR = 0.65 and is thus chosen for the next evaluation. This is in agreement with Yucel *et al.* (2015) who suggested that a value of zero is ideal for steep slopes like that of MSS as there are no noticeable accumulation. Increases in the RETDEPRTFAC on channel pixels can encourage more local infiltration near the river channel leading to wetter soils (Gochis *et al.*, 2015). This will not be necessary associated with the present case, since this will reduce surface runoff further reducing the hydrograph volumes.

The calibration of the OVROUGHRTFAC scaling factor results into the hydrograph shown in Figure II-5. Based on the resulting hydrograph and the selected statistics,

reasonable results are obtained at OVROUGHRTFAC = 0.4. At this point, maintaining the three parameters at their best value as determined, the model simulates yields an annual mean flow of 27.5 m³/s compared to that observed (47.4 m³/s) with an improvement of the objective criteria i.e., NSE = 0.59, RSR = 0.64 (Table II-1).

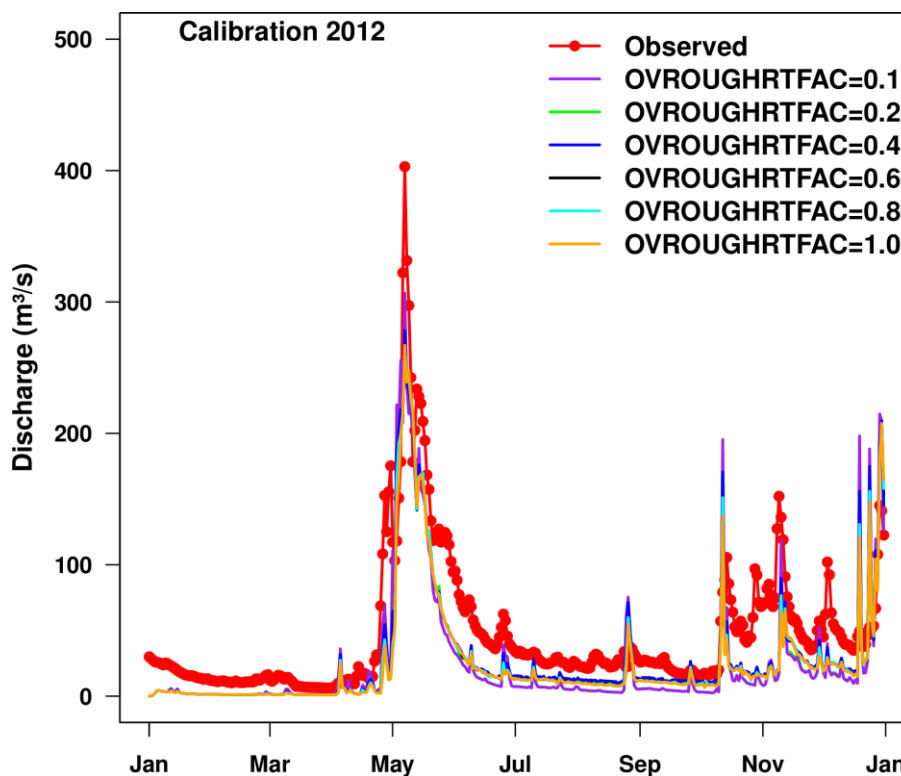


Figure II-5: Similar to Figure II-3 but shows sensitivity to the surface roughness scaling factor, OVROUGHRTFAC

With already calibrated parameters REFKDT, RETDEPRTFAC and OVROUGHRTFAC, the channel parameter Manning's roughness coefficient (MannN) is processed accordingly. Figure II-6 and Figure II-7 show the impact of the variation of the MannN on modeled discharge.

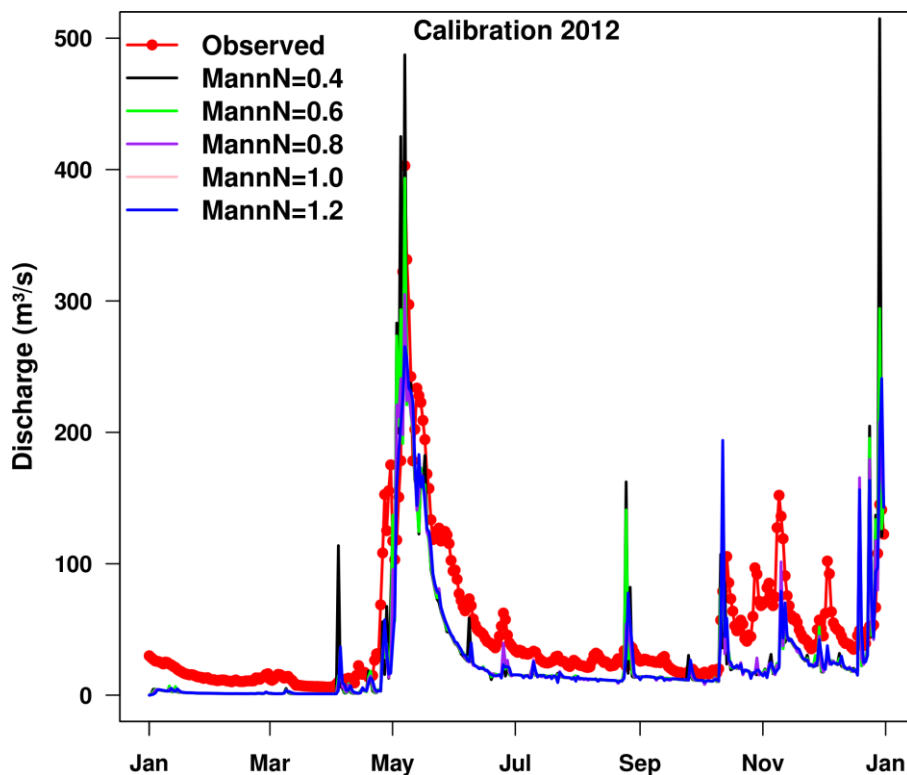


Figure II-6: Similar to Figure II-3 but for the impact of the channel Manning's roughness coefficients (MannN) with scale factor 0.4-1.2

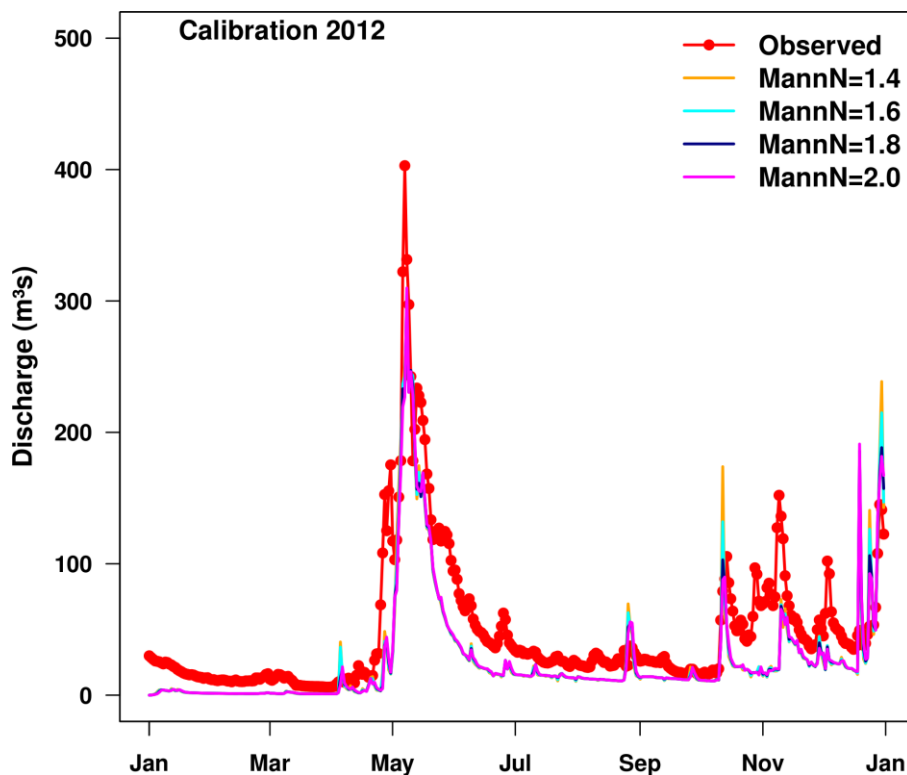


Figure II-7: Similar to Figure II-6 but for the MannN scale factor 1.4 – 2.0

At lower values of the MannN scaling factor, exaggerated high peaks during the months of May and December are noticed. Also the resulting statistics (NSE and RSR; Table II-1) become lower and higher respectively with decrease in MannN scaling factor. The MannN scaling factor of 1.8 gives the reasonable channel roughness that range between 0.99 and 0.02 with respect to the ten stream orders for MSS during the year 2012.

The summary of the four determined values of the calibrated parameters is shown in Figure II-8.

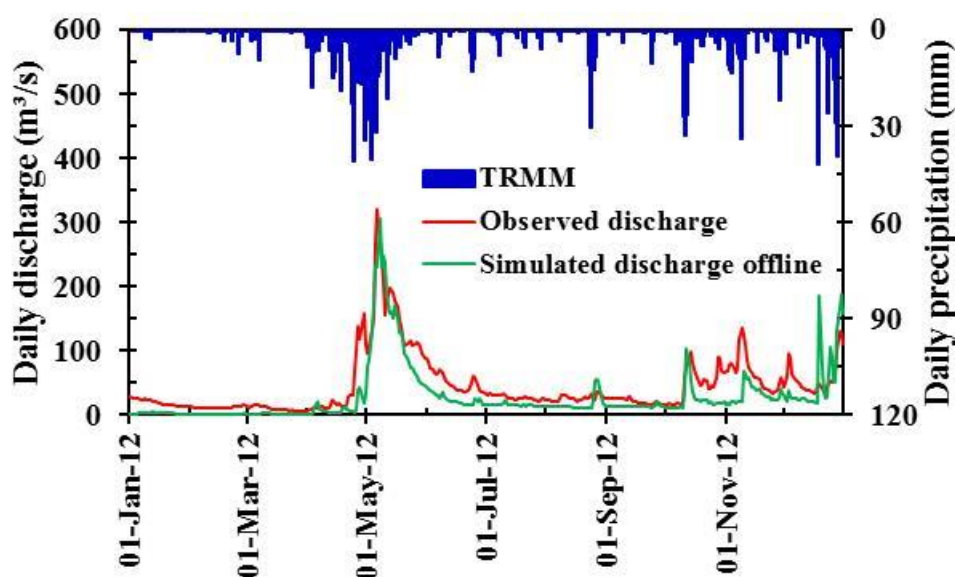


Figure II-8: Summary of the offline (uncoupled) WRF-Hydro and observed discharge at Tana Rukanga's RGS 4BE10 hydrographs and hyetograph based on TRMM for 2012

Based on the REFKDT = 2.0, RETDEPRTFAC = 0.0, OVROUGHRTFAC = 0.4 and MannN scale factor = 1.8, the resulting hydrograph show good temporal evolution in agreement with observations, it translates to a high correlation coefficient ($r > 0.9$) and reasonable NSE (= 0.62) and RSR (= 0.62). Table II-1 shows the values of the NSE and RSR at every stage of the calibration process. The uncoupled WRF-Hydro model shows more sensitivity in response to REFKDT and MannN consistent with earlier studies (Yucel *et al.*, 2015; Givati *et al.*, 2016), but not in RETDEPRTFAC and OVROUGHRTFAC. In general, the model was able to simulate only 60% of the observed discharge at the 4BE10 gauge. In general the offline (uncoupled) WRF-Hydro was able to capture reasonably the dynamics of the hydrological regime of the MSS streamflow.

In all subsequent simulations in this study, the above calibrated parameters are held as such.

II.7 Water balance computation

At the land-atmosphere interface the loss or “output” of water from the earth’s surface through evaporation and evapotranspiration is the input for the atmospheric branch, whereas precipitation, the atmospheric output, is considered an input or the gain of the terrestrial branch (Peixoto and Oort, 1992). Details of the water balance computation are available in many textbooks as in (Peixoto and Oort, 1992).

This section describes the atmospheric and terrestrial water balance computation from the WRF-only and coupled WRF-Hydro output.

Terrestrial water balance (TWB) calculation

The terrestrial water balance (TWB) can be written as:

$$\frac{dS}{dt} = R_{in} - R_{out} - ET + P = -R - ET + P, \quad \text{II-1}$$

where S (in mm) is the terrestrial water storage, R (mm/day) is the net outflow from the boundaries of MSS which is the difference of the outflow, R_{out} and inflow, R_{in} of surface and subsurface runoff (Oki *et al.*, 1995), ET (mm/day) is evapotranspiration, P (mm/day) is precipitation over MSS and t is time. It is noted that each term in Equation II-1 is spatially averaged over the area that encompasses MSS (see Figure I-1; blue rectangle). In Equation II-1, R is taken as the discharge from the Tana Rukanga’s river gauge station (RGS) 4BE10.

Atmospheric water balance (AWB) calculation

The atmospheric water balance (AWB) components are related as:

$$\frac{dW}{dt} = IN - OUT + ET - P - \varepsilon_A = -\vec{\nabla} \cdot \vec{Q} + ET - P - \varepsilon_A, \quad \text{II-2}$$

where W (in mm) is the precipitable water content of the atmosphere above MSS, IN and OUT are the inflow and outflow of water vapor flux of the MSS, $IN - OUT = -\vec{\nabla} \cdot \vec{Q}$ is mean convergence of lateral atmospheric vapor flux in mm/day. The atmospheric vapor flux is computed from vertically integrated moisture fluxes taking note on the horizontal water vapor fluxes; specific humidity winds (meridional and zonal) and surface pressure (Roberts and Snelgrove, 2015). ε_A in Equation II-2 is the atmospheric water balance residue or imbalance. Details of the processing of the AWB components from the model output are presented in Appendix C: Computation of the water balance components.

Schär *et al.*, (1999) noted that ε_A can be distributed equally among the atmospheric fluxes as follows: $IN^{corr} = IN - \varepsilon_A/2$ and $OUT^{corr} = OUT + \varepsilon_A/2$ in order for the atmospheric fluxes to satisfy the budget constraints.

Therefore,

$$-\vec{\nabla} \cdot \vec{Q}^{corr} = IN^{corr} - OUT^{corr}, \quad \text{II-3}$$

where the superscript “*corr*” means corrected fluxes.

Letting $C = -\vec{\nabla} \cdot \vec{Q}^{corr}$ as in (e.g., Yeh and Famiglietti 2008), Equation II-2 thus becomes:

$$\frac{dW}{dt} = C + ET - P. \quad \text{II-4}$$

In some literature (e.g., Oki *et al.*, 1995; Marengo, 2005; Yeh and Famiglietti, 2008) it is argued that for longer periods, preferably months and beyond, dS/dt and dW/dt approximately equal to zero and can be assumed to be negligible and Equations II-1 and II-4 can be combined to as

$$C - \frac{dW}{dt} = P - ET = R + \frac{dS}{dt}. \quad \text{II-5}$$

Therefore based on the aforementioned assumptions, Equation II-5 can be written as

$$C = P - ET = R. \quad \text{II-6}$$

Equation II-6 is valid on a longer timescale if the water balance is closed (Marengo, 2005; Yeh and Famiglietti, 2008). It is considered a good criterion of evaluating the agreement between atmospheric and hydrological datasets (Yeh and Famiglietti, 2008). Further modification of the above equations can be used to determine the variables that are not measured at the MSS e.g. the change in basin water storage and evapotranspiration.

Two atmospheric water balance measures, which is, the precipitation efficiency, χ and recycling ratio, β showing the land-atmospheric interactions relating P , ET and IN are defined in Equations II-7 and II-8. The equations are presented as derived by Schär *et al.* (1999) and mentioned in e.g., Kunstmann and Jung (2007) and Asharaf *et al.* (2012) as

$$\beta = \frac{ET}{IN+ET} \quad \text{II-7}$$

and

$$\chi = \frac{P}{IN+ET} \quad \text{II-8}$$

β is the fraction of precipitation in the study area that originates from evapotranspiration from the study area. χ represents the fraction of water that enters our study area either by evapotranspiration or atmospheric transport and subsequently falls as precipitation. β and χ are also referred to as bulk properties of the regional water cycle and are based on a number of assumptions key being that the water vapor transported across the boundary or evapotranspiration within the region is well mixed. The local recycling ratio delineates the source of mass of water in precipitation between local and remote geographic sources. It can be used to characterize and quantify the regional intensity of the water cycle (Eltahir and Bras, 1996). The magnitude of either of these measures shows their contribution the precipitation within the domain.

III WRF-only: Sensitivity and performance at 50 and 25 km

III.1 Introduction

In Chapter II, details of different parameterizations for sensitivity experiments selected for this thesis are provided. In this chapter, two sensitivity experiments' results for the WRF-only model, based on the outer domain D1 at 50 and 25 km horizontal resolution are described. Table III-1 presents the combinations of the different parameterizations and hence acronyms of the first set of these experiments at 50 km horizontal resolution. The second set of experiments' results is presented from Section III.5 onward, representing work which has been published in Kerandi *et al.* (2016).

Table III-1: The acronyms of the WRF sensitivity experiments at 50 km horizontal resolution

		Microphysics		
		*ACM2	Lin (Purdue)	WSM6
Cumulus convection	BMJ		BLA	BWA
	GF		GLA	GWA
	KF		KLA	KWA

* Planetary boundary layer scheme ACM2, is common for all experiments

As a recap, the precipitation and temperature climatology of different sections of TRB i.e., upper Tana UT, middle Tana MT, and lower Tana LT (refer Figure I-1) represented by the stations therein, is summarized in climate diagrams (*Walter-Lieth diagrams*) shown in Section III.2. Climate diagrams summarize trends in temperature and precipitation for at least 30 years thus providing the relationship between these two variables and the resulting seasons of the target region. When the precipitation curve undercuts the temperature curve, the area in between is dotted, indicating a dry season, while a wet (moist) season is shown by vertical lines which are plotted for each month. When the precipitation curve exceeds 100 mm, this is associated to a period of excess water described by blue shading. Other details in the diagram include: the elevation above sea level in meters, mean annual temperature in degrees Celsius, precipitation in millimeters, and the maximum and minimum temperature placed on the left of the temper-

ature axis. Fersch (2011) used similar diagrams to characterize 6 different climatic and hydrologic regions using gridded observations. In the present study, real station values are used for all cases of precipitation while CRU temperature gridded dataset is used in place of few missing station values.

III.2 Rainfall and temperature climatology of Tana River basin

In this section, each part of the TRB is considered separately to give a picture of the two variable's climatology. This will form a basis of comparison of model simulations along with the station and gridded datasets.

III.2.1 Upper Tana

Figure III-1 is consistent with the climate characteristics of the UT as outlined in Chapter I. The two rainy seasons (i.e., MAM and OND) and the dry months of June to September (JJAS) are well depicted. The annual precipitation ranges between 930 and 1302 mm with Meru, which is north of the Equator, receiving the highest amount. The annual mean temperature lies between 17 and 20 °C while the minimum and maximum monthly mean temperature lies within the range 10 and 13 °C and 27 and 28.5 °C respectively. The stations in the UT are only 100s of kilometers away from each other. It is therefore expected that they experience more or less similar equatorial climate. This is evidenced from the climate diagrams shown in Figure III-1, which further shows that there is a period excess of water in each of the four stations especially during the MAM season.

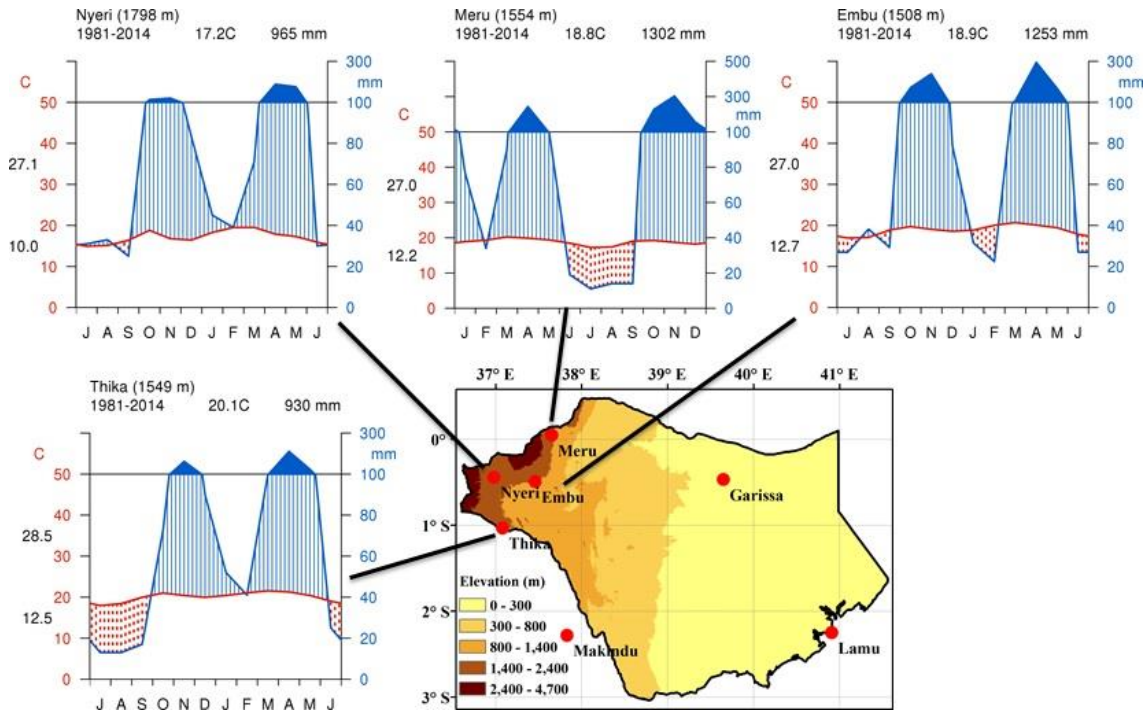


Figure III-1: Climate diagrams for the UT stations and the corresponding elevation map for the TRB

III.2.2 Middle Tana

The MT is characteristic of most of Kenya, which is classified as 75 % semi-arid or arid with very little rainfall even during the two major rainy seasons of MAM and OND. Figure III-2 shows the climatology of the two stations (Garissa and Makindu) that represent the MT. Here, the dry seasons are more pronounced than in any other part of the TRB. The region experiences the longest dry season of 5 months i.e., May to September with higher temperatures than any other part of TRB. In this region, the OND season is slightly wetter than the MAM season contrary to expectations.

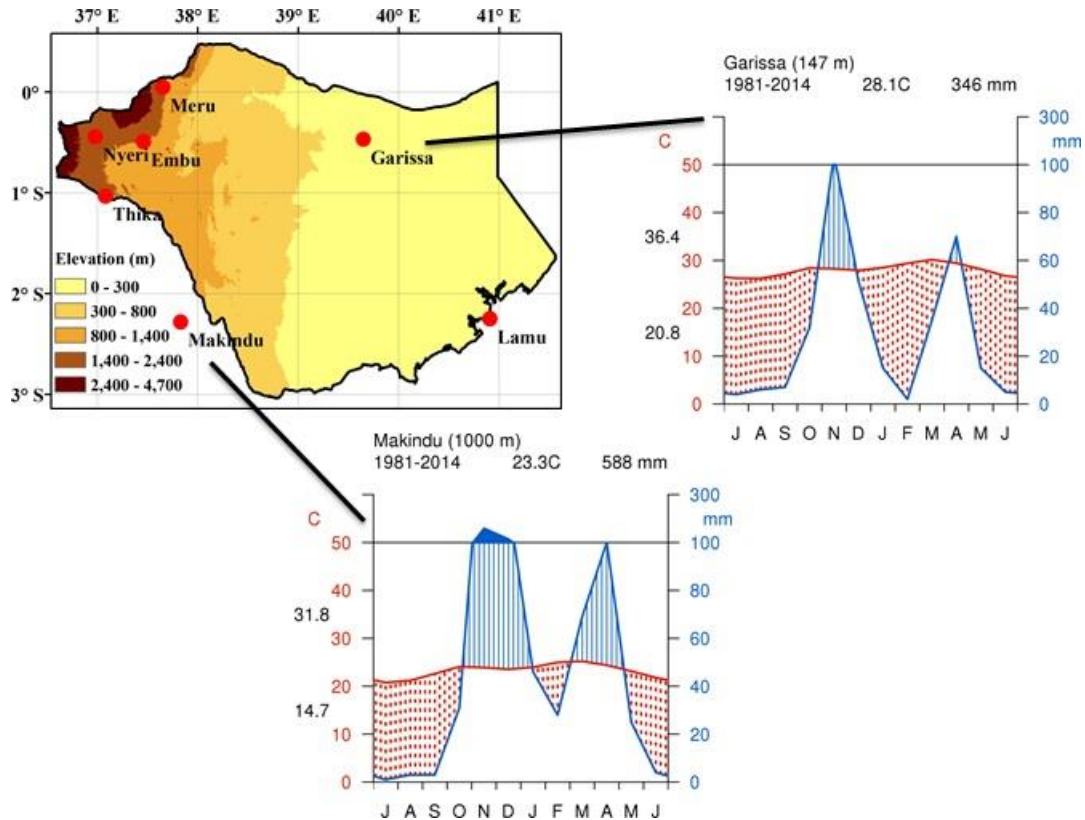


Figure III-2: Climate diagrams for the meteorological stations and the corresponding elevation map for the TRB

III.2.3 Lower Tana

The LT is at the lowest altitude above sea level of all considered sections of the TRB. It borders the west of the Indian Ocean and its climatology is influenced by the ocean's coastal wind regime and transport of air masses. Here, the MAM season contributes the most amount of rain compared to the OND season (see Figure III-3). The elevation-precipitation relationship is not a factor here as the area around Lamu which is at an altitude of 6 m.a.s.l. has an average annual rainfall between 760-1100 mm compared to for instance Garissa at an altitude of about 147 m.a.s.l. with corresponding precipitation of below 500 mm.

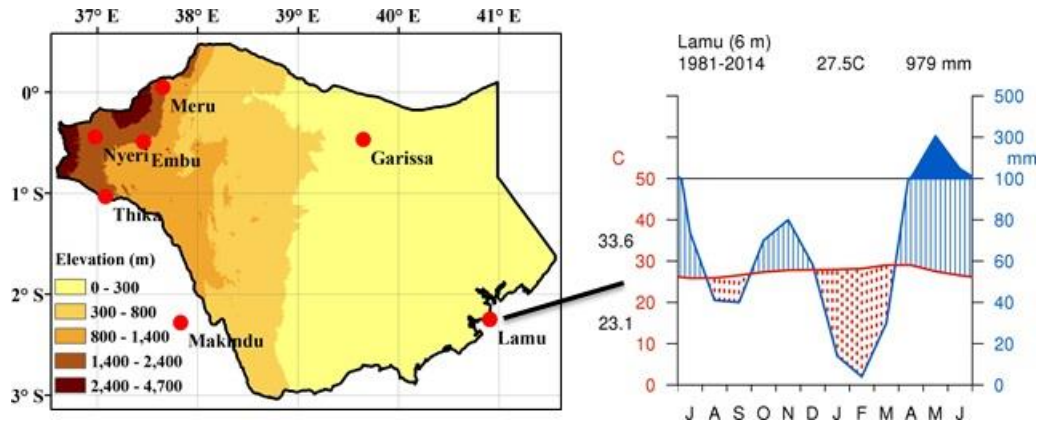


Figure III-3: Climate diagram for the LT region and the corresponding elevation map for TRB

III.3 Precipitation

With the above review of the precipitation and temperature climatology of the TRB based on long term observations, details of each of these variables and especially focusing on the simulations in the WRF model for the period 2011-2014 are described. Section III.3 presents model precipitation results versus stations observations on one hand and on the other hand versus the TRMM data.

III.3.1 Model results at 50 km horizontal resolution versus station observations

Figure III-4 shows the scatter plots for the UT, MT and LT sections of TRB, based on precipitation from the respective meteorological stations compared to WRF simulations. The plots represent the anomalies or mean centered values of each total monthly station's precipitation and the corresponding simulated precipitation for each part of the TRB. The mean centered values are obtained by subtracting each value of the series from the long term mean of each series. The r values shown correspond to the anomalous correlations.

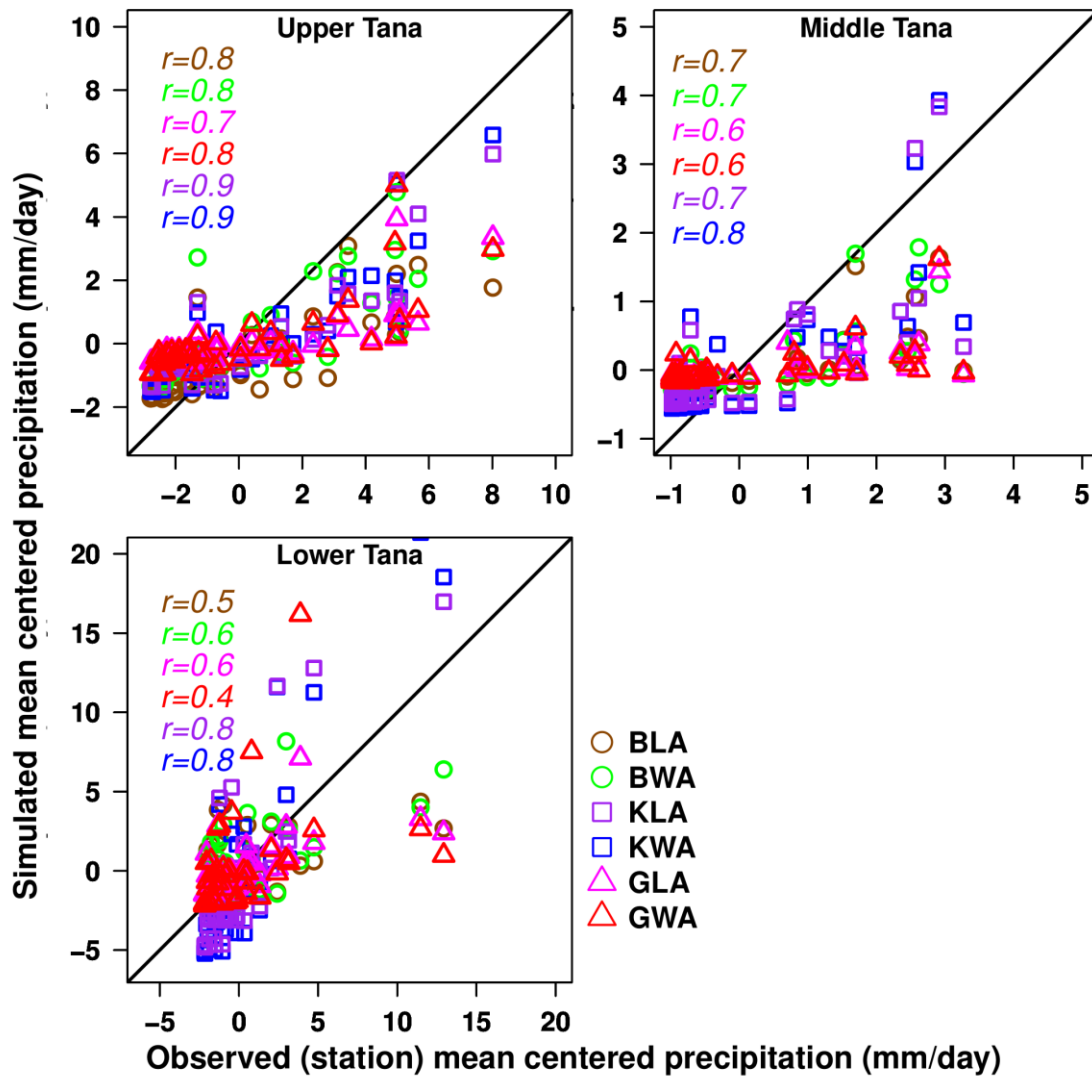


Figure III-4: Monthly gridded products which are mean centered from the six WRF experiments compared to rainfall data from selected stations over the Tana River basin for 2011-2014

In all considered six WRF configurations, there is a display of reasonable degree of agreement ($r > 0.5$) with station data time series in all sections of the TRB. Higher correlation coefficients are realized at the UT whereas mixed or much lower scores are recorded at LT.

The KLA and KWA (KF-based combinations) consistently display higher correlation scores in all sections of TRB with however exaggerated few high values in the LT. However the simulated precipitation in the LT is lower than that observed at the UT and MT. BLA and BWA (BMJ-based combinations) have correlations scores that fall be-

tween those of KF-based combinations and the GLA and GWA (GF-based combinations).

Annual and seasonal totals

Figure III-5 shows the characteristics of mean seasonal precipitation over the stations in the UT, MT and LT. There is generally a wide disparity in the case of the MAM season. However, with each individual parameterization combinations there seems to be a uniform distribution of the seasonal precipitation. There is consistent underestimation of the station precipitation in both the UT and MT by all the six WRF configurations.

In **UT**, only the KWA configuration yields more than half of the observed (2011-2014) and climatological (1981-2014) mean annual precipitation described in Section III.2.1, both seasonally and annually. For instance, during the MAM season, all the six WRF configurations exhibit poor performance with less than half the precipitation amount observed at the station for 2011-2012. It is only during 2013 that the KF combinations realized 60 - 70 % of the observed precipitation. In general, during this season KWA yields more precipitation than KLA with both the GF-based and BMJ-based combinations yielding the least amount of precipitation. Similarly, the KF-based combinations show the closest variability whereas the GF-based combinations show the least variability compared to that of the stations. In the case of the OND season, there is slightly mixed performance as the BMJ-based combinations more so BWA, register better performance in 2011-2012 even than KLA i.e., 65 % of the station precipitation. In OND season, all the configurations show more or less similar variability over UT.

In the **MT**, the KF-based combinations produce more than half of the observed and climatological mean annual precipitation. KWA produces amounts closer to that observed, i.e., 45 % of the cumulative seasonal amounts during the MAM season. The performance of all the configurations during OND is similar to that of MAM. All the six WRF configurations register poor performance during 2013 and 2014. The KF-based combinations depict same magnitude as that of stations while it is low for all the other four configurations during the MAM season. In terms of variability, during OND, the GF-based combinations match the station variability while the KF-based combinations show slightly the highest variability.

In **LT**, both the BMJ-based and GF-based combinations agree reasonably with the observed and climatological mean annual precipitation while the KF-based combinations

are wetter. The GWA-based combinations produce seasonal amounts closer to that recorded at the station. In the case of variability, in both MAM and OND seasons, the KF-based combinations show the highest variability while GWA's variability slightly matches that of the station precipitation.

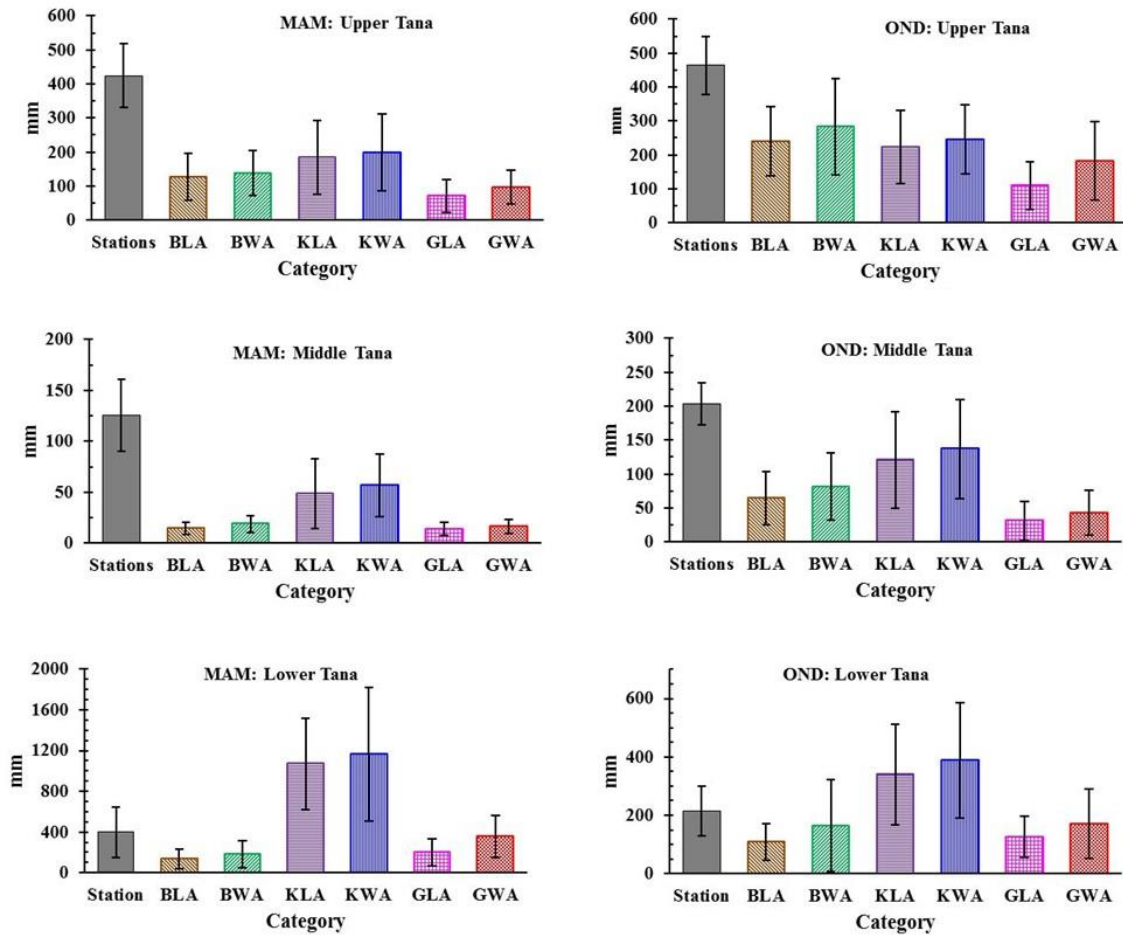


Figure III-5: Mean seasonal (MAM and OND) precipitation as observed in the stations and simulated over different sections of Tana River basin shown in bars. The mean is computed from the seasonal totals during 2011-2014. The error bars indicate their corresponding standard deviation

III.3.2 Model results at 50 km horizontal resolution versus TRMM data

The spatially averaged precipitation over the TRB and surrounding areas simulated in the six WRF configurations is compared to TRMM estimates. The results for the UT and MT are consistent with that described in Section III.2.1. The KF-based

combinations yield more than 50 % (KLA ~ 54 %, KWA ~ 60 %) of the mean annual precipitation derived from TRMM. These results are confirmed in Table III-2 that shows the total amounts for the 4 years taking into consideration precipitation from the two rainy seasons of MAM and OND. As seen before, the BMJ-based combinations yield amounts that fall between the GF-based and the KF-based combinations.

Table III-2: Mean annual amount of precipitation (MAM + OND) simulated by the six WRF configurations and derived from TRMM spatially averaged over study area for 2011-2014

Category	Total amount (mm/yr)	% of observed (TRMM)
TRMM	502	100
BLA	144	29
BWA	182	36
KLA	280	56
KWA	313	63
GLA	90	18
GWA	126	25

The six WRF experiments' performances in reproducing the annual and seasonal precipitation are similarly replicated as before. This is illustrated in the seasonal mean and standard deviation results as seen in Figure III-6. The results of KWA experiment are closest to that of TRMM compared to the other five configurations in both MAM and OND.

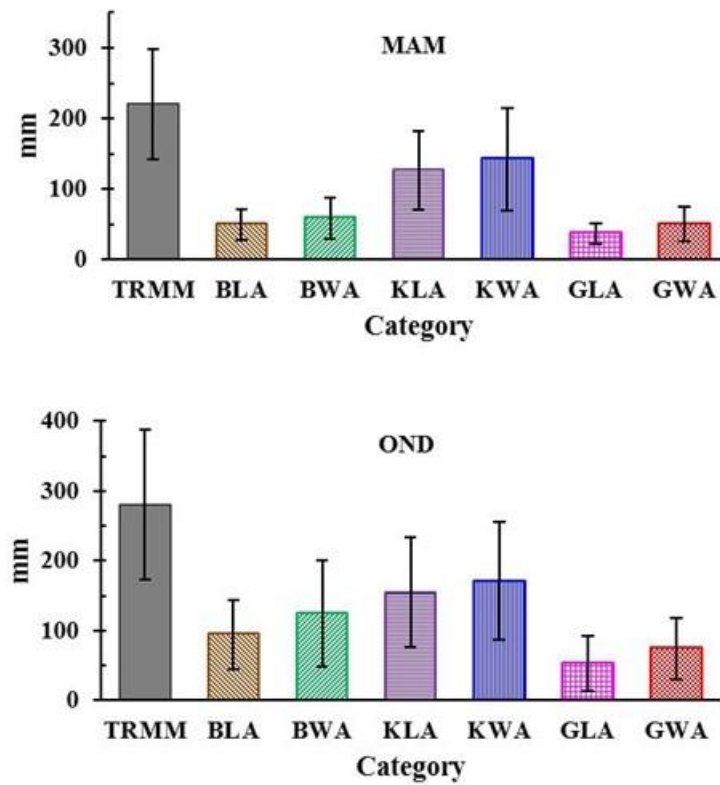


Figure III-6: Mean seasonal (MAM and OND) spatially averaged precipitation as estimated in TRMM and simulated in the six WRF experiments over the TRB. The mean is computed from the seasonal totals during 2011-2014. The error bars indicate their corresponding standard deviation

III.4 Temperature

Here the focus is on temperature model results simulations versus temperature recorded at the stations firstly and secondly versus the CRU temperature.

III.4.1 Model results at 50 km horizontal resolution versus station temperatures

The three variables of monthly mean temperature (minimum, maximum and mean) at the stations (Nyeri, Meru, Thika and Lamu) are compared to the corresponding WRF grid-points.

Table III-3 shows the average mean annual temperatures of these variables.

Minimum temperature: The mean annual minimum temperature (2011-2014) for the stations Nyeri, Meru, Thika, and Lamu are slightly warmer by 1-2 °C than that of the coldest months in each of these stations during the period 1981-2014. The six WRF configurations simulate similar temperatures over these stations. Over Nyeri, Thika and coastal Lamu, there is a colder bias (i.e., approximately 5 °C, 2 °C and 1 °C respectively). However, over Meru, all the WRF configurations show a warmer bias of approximately 2 °C.

Maximum temperature: The mean annual maximum temperature (2011-2014) recorded over the stations is colder by 2-3 °C than that of the corresponding hottest month during the period 1981-2014. All the WRF configurations simulate colder temperatures with (colder) bias of as higher as 10 °C.

Mean temperature: The average annual temperatures simulated in the six WRF configurations are equally colder as those of maximum temperature (≈ 8 °C in Nyeri, ≈ 2.3 °C in Meru, ≈ 6.1 °C in Thika, ≈ 3 °C in Lamu).

Table III-3: The mean annual temperature (minimum, maximum, mean) during the period 2011-2014 as recorded in the stations (Nyeri, Meru, Thika and Lamu) and that derived from the 6 WRF configurations. The elevation m.a.s.l. of each of the stations is indicated

	Nyeri (1798 m.a.s.l.)	Meru (1554 m.a.s.l.)	Thika (1549 m.a.s.l.)	Lamu (6 m.a.s.l.)
Minimum temperature				
Station	12.5	13.3	14.2	24.3
BLA	7.9	14.7	11.2	23.9
BWA	8.0	14.6	11.3	23.8
KLA	8.5	14.9	11.3	23.7
KWA	8.6	14.9	12.1	33.7
GLA	7.7	14.1	11.0	23.3
GWA	7.9	14.2	11.2	23.3
Maximum temperature				
Station	23.8	24.1	26.7	31.8
BLA	13.5	18.6	17.3	26.4
BWA	13.5	18.3	17.2	26.4
KLA	13.0	18.3	16.8	25.9
KWA	13.1	18.3	16.9	26.0
GLA	13.1	18.3	17.0	26.2
GWA	13.4	18.3	17.2	26.1
Mean temperature				
Station	18.2	18.7	20.4	28.0
BLA	10.6	16.5	14.3	25.1
BWA	10.7	16.5	14.3	25.1
KLA	10.6	16.4	14.2	24.8
KWA	10.7	16.4	14.3	24.8
GLA	10.3	16.0	14.2	24.8
GWA	10.5	16.0	14.3	24.7

The relationship between the time series of the three monthly mean temperature variables (minimum, maximum and mean) as simulated versus that recorded at the stations is summarized in scatter plots of mean centered values (anomalies for the period 2011-2014). This is illustrated in Figure III-7.

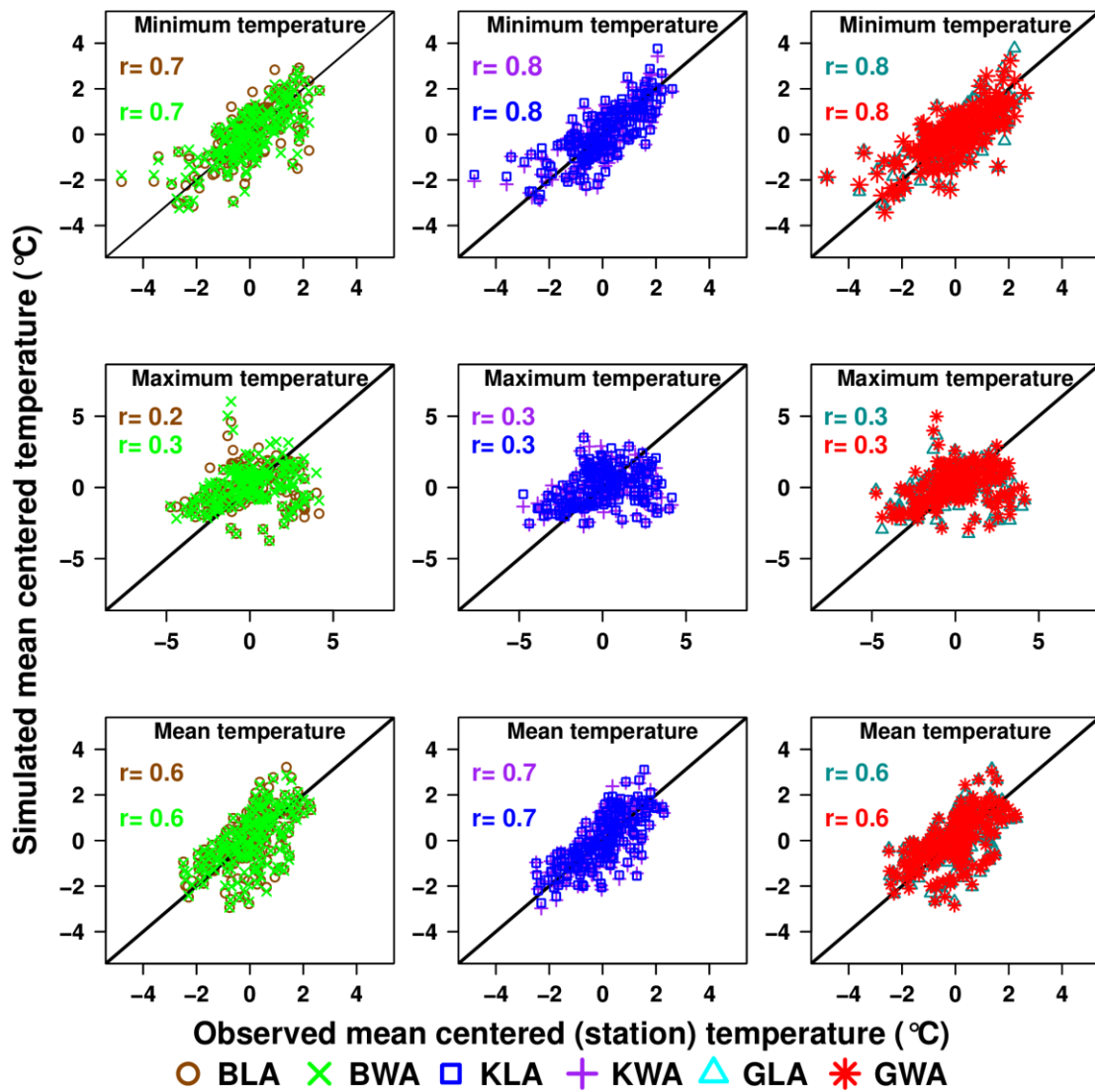


Figure III-7: Scatter plot showing simulated and observed (station) mean centered monthly mean temperatures (minimum, maximum and mean) from the six WRF configurations for the period 2011-2014

The greatest bias seen in the maximum temperature as seen earlier in

Table III-3 is further confirmed by very low correlation coefficients between the simulated and observed monthly mean maximum temperature in all the six WRF configurations as illustrated in Figure III-7. There is however reasonable agreement between the simulated and observed monthly means minimum temperature in all the configurations which show similar correlation coefficients ($r > 0.7$). In general, the performances of the six WRF configurations are similar for the simulation of the given variable.

III.4.2 Model results at 50 km horizontal resolution versus CRU temperature

The six WRF model configurations capture well the interannual evolution of temperature compared to that derived from CRU as seen in Figure III-8, with $r > 0.6$ (see

Table III-4). In line with the results attributed to the stations, the WRF configurations simulate similar temperature with spatially averaged series. The minimum temperature (T_{\min}) have the least bias (lowest MAE) while the highest bias ($\text{MAE} \leq 10 \text{ }^\circ\text{C}$) is depicted in case of maximum temperature (T_{\max}). This bias impacts the simulated mean temperatures (T_{mean}) which equally has a higher colder bias.

The mean seasonal temperatures are similarly simulated consistent with previous discussions. As expected, mean season temperatures during OND are slightly lower than those during MAM season.

All the six WRF model configurations underestimate both precipitation and temperature during the period 2011-2014 at the 50-km horizontal resolution in the upper and middle Tana. The different configurations demonstrate the dependence of precipitation on topography as seen in the simulation results over UT and MT. There is however an exaggerated overestimation of precipitation over LT (in Lamu station). This may be attributed to the microclimate in this region and its proximity to the Indian Ocean. In general, the KWA configuration reproduces the precipitation climatology over the UT and MT closer to observations than the other five configurations (i.e., KLA, BLA, BWA, GLA and GWA). KWA is thus selected for all subsequent experiments from Section III.5 onward in this thesis.

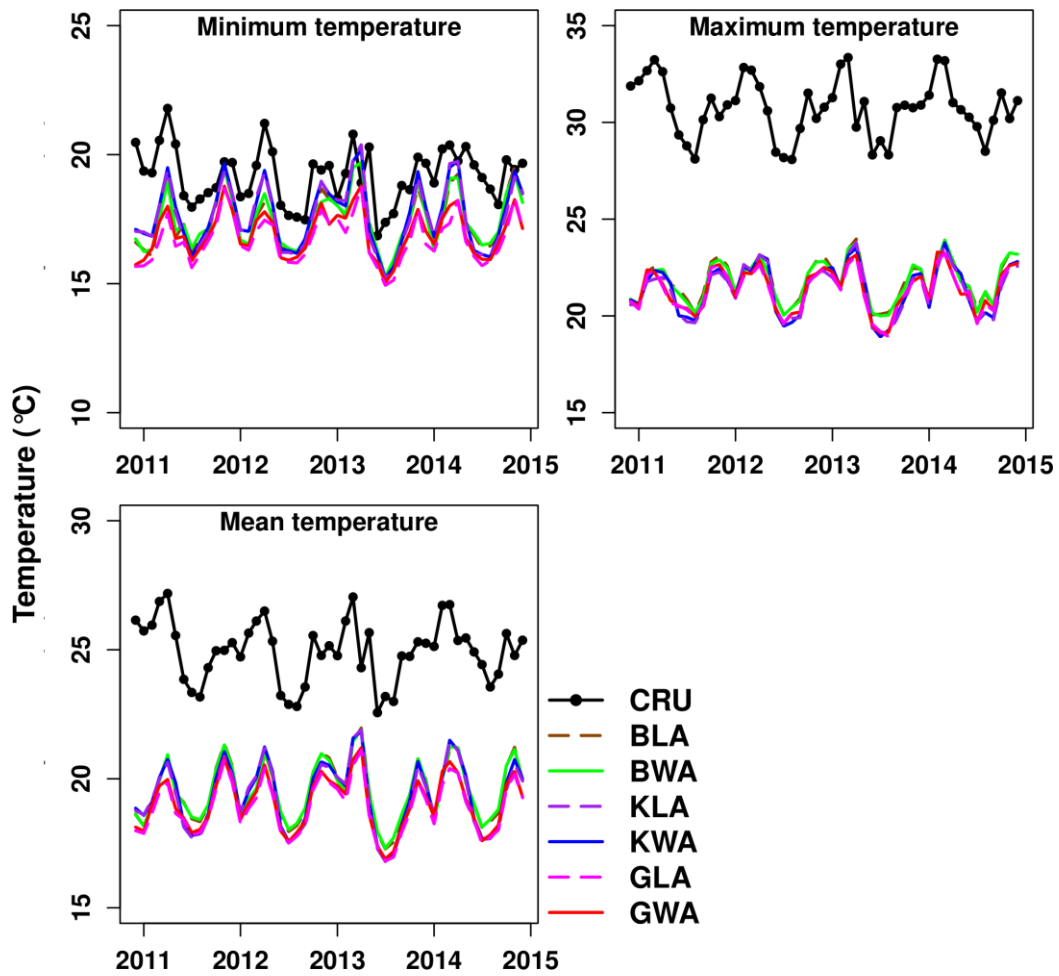


Figure III-8: Monthly mean temperature (minimum, maximum, and mean) spatially averaged over the study area for the period 2011-2014, derived from CRU and the six WRF simulations

Table III-4: The correlation coefficient, r and mean absolute error, MAE between monthly mean temperature (minimum, maximum and mean) derived from CRU and the six WRF configurations for 2011-2014

Experiment	Correlation coefficient, r			Mean absolute error, MAE		
	T_{min}	T_{max}	T_{mean}	T_{min}	T_{max}	T_{mean}
BLA	0.60	0.57	0.60	1.8	8.9	5.4
BWA	0.61	0.60	0.60	1.7	9.0	5.4
KLA	0.66	0.66	0.73	1.7	9.4	5.6
KWA	0.67	0.68	0.72	1.6	9.3	5.6
GLA	0.53	0.66	0.64	2.5	9.4	6.0
GWA	0.57	0.69	0.68	2.3	9.4	5.9

III.5 Impact of land use and horizontal resolution on modeled precipitation

This section investigates the WRF's ability in simulating the seasonal, annual cycle and interannual variability of precipitation in the TRB. More specifically, the impact of two different land use classifications, i.e., (MODIS and USGS; Section II.1) at two horizontal resolutions (50 km and 25 km) is investigated. This assessment of the WRF model, based on all possible combinations, results in 4 experiments denoted to as: MODIS25, MODIS50, USGS25 and USGS50. This forms part of the second set of WRF sensitivity experiments based on outer domain D1. An explanation of the land-cover or land-use classifications over the TRB in MODIS and USGS is given in Section III.5.1. The simulated precipitation results versus both station and TRMM data are discussed in Sections III.5.2 and III.5.3 respectively. The work in Sections III.5 and III.6 has been published in the Journal of Theoretical and Applied Climatology (Kerandi *et al.*, 2016).

III.5.1 Land use distribution in the TRB

Figure III-9 illustrates the distribution of the dominant mean land use category in each model grid over the TRB from the four WRF experiments as depicted in the land use classifications. MODIS and USGS land use datasets classify the regions slightly differently, but show reasonable agreement in the portions of the savannas.

Note that within each model grid, the most dominant land use category from the land use map (24 categories for USGS, and 20 for MODIS) in terms of contributing area is chosen for that grid (Liang *et al.*, 2005). Accordingly, there are 9 classes for MODIS25 and only 5 classes for MODIS50 over the TRB (Figure III-9a-b). The MODIS driven experiments classify the TRB to be covered by 70 % savannas and grasslands. According to the global land cover characteristics (GLCC) classification, these two categories are of herbaceous type with forest canopy cover between 10-30 %. As an illustration, MODIS25 classifies regions around Nyeri, Embu, Meru and Thika to be dominated by evergreen broadleaf forestland and woody savanna. USGS25 and USGS50 display 7 and 5 classes out of the 24 land use categories respectively (Figure III-9c-d). The dominant land use categories for TRB based on USGS classification are the shrublands and croplands/woodland mosaic constituting about 80% of the total area. The GLCC classifies shrublands as lands characterized by xerophytic vegetative types and woody systems with desert like features. For the area around Nyeri, Embu, Meru

and Thika, USGS25 describes it to be savanna and deciduous broadleaf forest, which is in contrast with the MODIS classification.

Compared to USGS25, MODIS25 provides a more heterogeneous spatial pattern, which is attributed to enhanced sensitivity of MODIS land use to horizontal resolution in comparison to USGS land use (Pohl *et al.*, 2011).

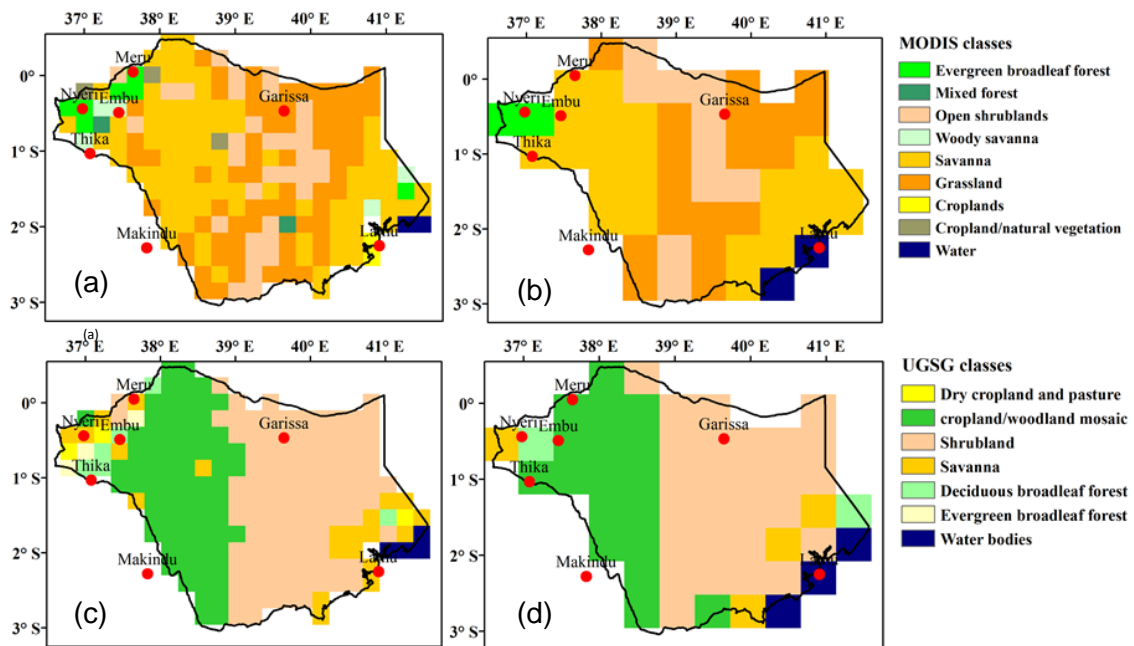


Figure III-9: The dominant land use category in each grid point over the TRB: (a) MODIS25, (b) MODIS50, (c) USGS25 and, (d) USGS50 during the period 2011-2014 (Kerandi *et al.*, 2016)

III.5.2 Model results versus station data

Figure III-10 illustrates the performance of the four WRF configurations in simulating the annual cycle of precipitation at grid points corresponding to the stations in the three sub regions of TRB. All configurations capture well the shape of rainfall seasonality reasonably. They, however, underestimate the precipitation peak in the upper TRB during MAM, while MODIS25 agrees well with observations in both timely and magnitude of the peak during OND season. In the middle TRB, all the experiments clearly underestimate the MAM and OND precipitation whereas in the lower part it is clearly overestimated.

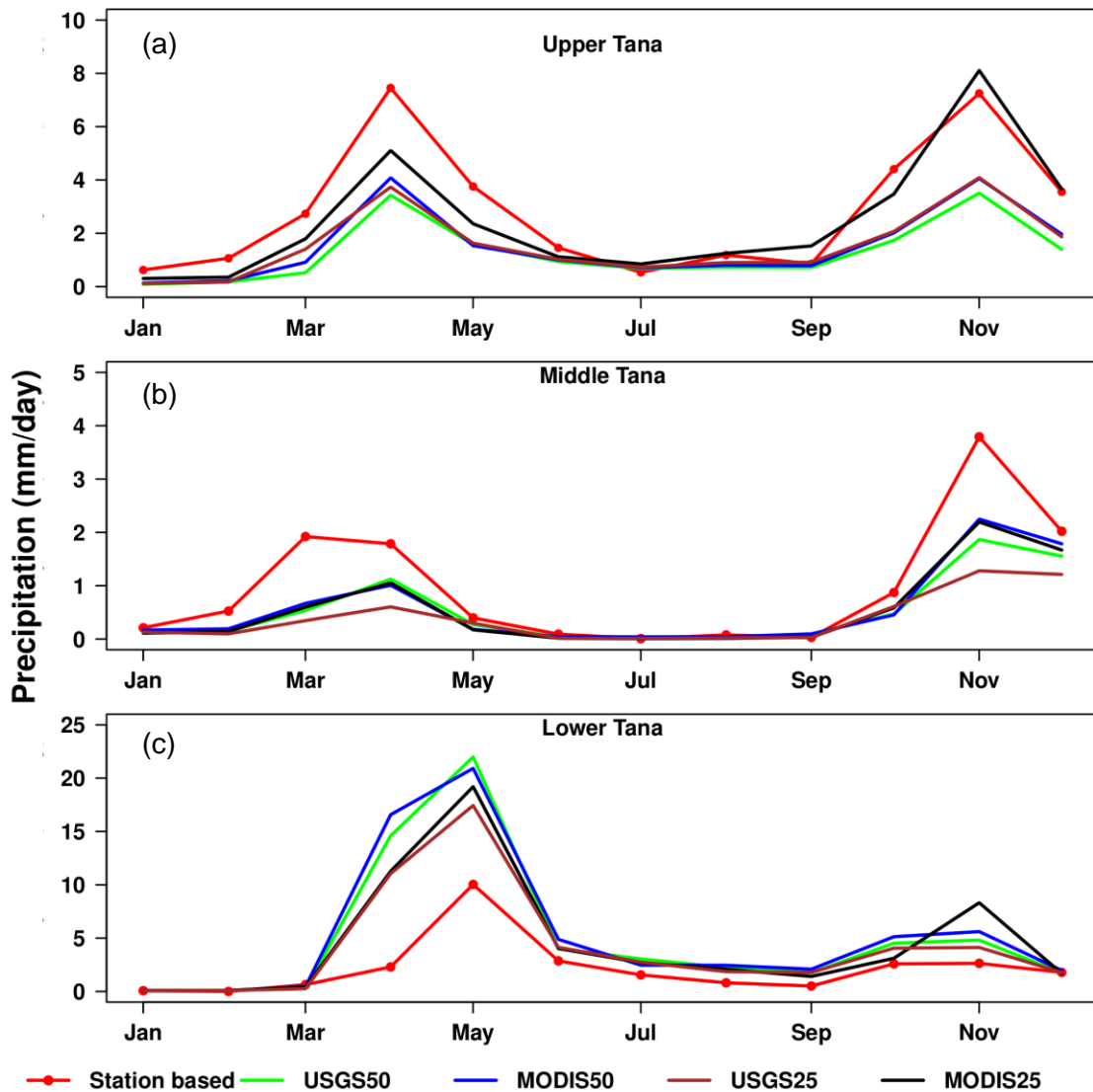


Figure III-10: Mean annual cycle of precipitation over the stations in the three sub regions of the TRB (a) upper TRB, (b) middle TRB, and (c) lower TRB (in mm/day) derived from station data and WRF simulations: MODIS25, MODIS50, USGS25 and USGS50 for 2011-2014

Seasonal and annual totals

In the upper TRB, the MODIS25 produced seasonal and annual amounts closest to that recorded at the stations throughout the period 2011-2014. In particular, during the OND season, whereas all other configurations underestimated the seasonal amounts, MODIS slightly overestimated that of 2011 and 2012 and reasonably matched that of 2013 and 2014. In the middle TRB, the different WRF configurations yielded distinct seasonal and hence annual amounts. There is clearly no consistency of superiority among the different configurations. Just as in the annual cycle, all configurations clearly

underestimated the precipitation during MAM and OND seasons. In the lower TRB, all the WRF configurations overestimated the station precipitation consistent with earlier findings. The aforementioned is illustrated in Table III-5 that shows the mean seasonal and annual precipitations.

Table III-5: Mean seasonal and annual precipitation averaged over stations in upper, middle and lower TRB during 2011-2014

Upper TRB					
	Station	USGS50	MODIS50	MODIS25	USGS25
MAM	424.7	168.2	198.4	281.9	206.2
OND	464.1	202.2	245.1	464.2	244.7
Annual	1060.6	471.3	554.2	909.8	568.1
Middle TRB					
	Station	USGS50	MODIS50	MODIS25	USGS25
MAM	125.4	58.8	56.6	55.6	38.1
OND	203.5	118.7	136.9	135.7	94.9
Annual	356.5	191.6	210.9	200.8	142.1
Lower TRB					
	Station	USGS50	MODIS50	MODIS25	USGS25
MAM	399.9	1127.8	1159.7	946.2	880.1
OND	214.8	338.8	388.4	398.5	304.7
Annual	791.3	1808.5	1915.9	1660.7	1510.3

Interannual variability

The standard deviation (σ) of yearly annual and seasonal (MAM, OND) total precipitation during 2011-2014 is determined in order to investigate the interannual variability of the four WRF configurations using the station data as a reference. In the upper TRB, all WRF configurations show a reasonable magnitude of interannual variability. MODIS25 exhibits a closer variability like that of observed data. There is relatively greater variability during the MAM season than during OND and even annually. This is not the case in middle TRB, as all the WRF configurations fail to capture the relative magnitudes of the annual, MAM and OND variability. In the lower TRB, only MODIS25 fails to capture the relative magnitudes of the annual, MAM and OND variability. The OND season shows clearly the greatest variability than that of MAM and annual variability.

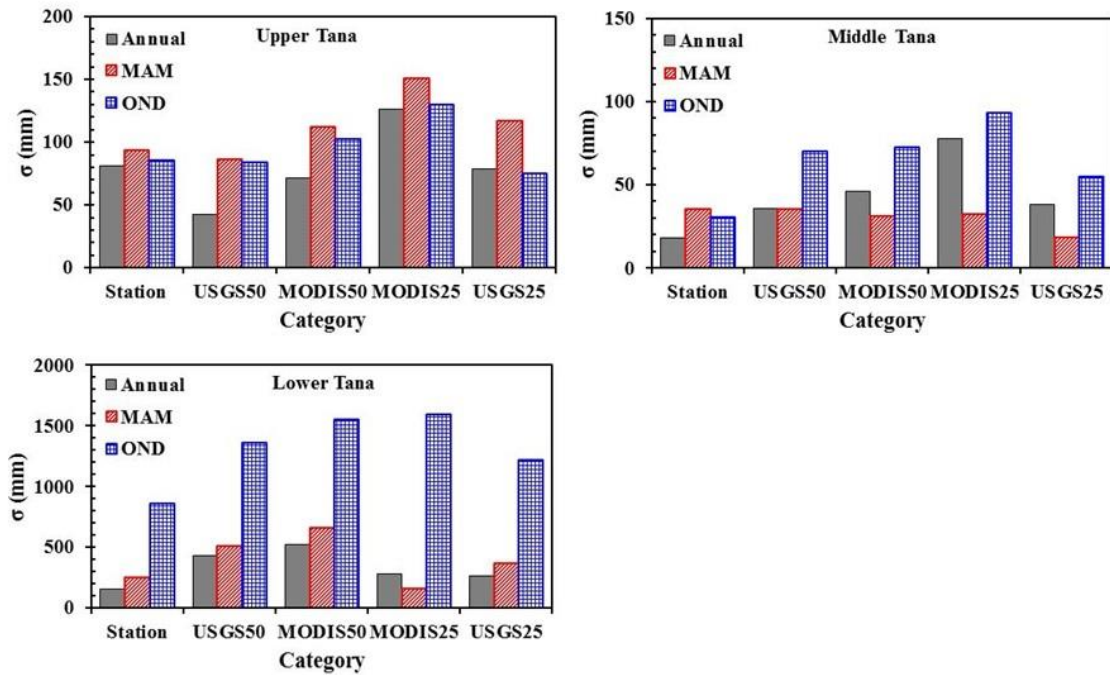


Figure III-11: Standard deviation of annual, seasonal (MAM, OND) total precipitation during the period 2011-2014. Precipitation is derived from station data distributed over the TRB sub-regions and the four WRF configurations (USGS50, MODIS50, MODIS25, and USGS25)

III.5.3 Model results versus gridded data

The simulated annual cycle of precipitation for the period 2011-2014 mimics reasonably that of TRMM for all considered WRF configurations ($r > 0.9$ with 95 % confidence interval and p -value < 0.001 ; Figure III-12). The climatological seasonal peaks in April and November are well captured, yet all the four configurations underestimate the monthly mean precipitation as seen in Section III.5.2. The two known rainfall seasons of MAM and OND are generally well depicted.

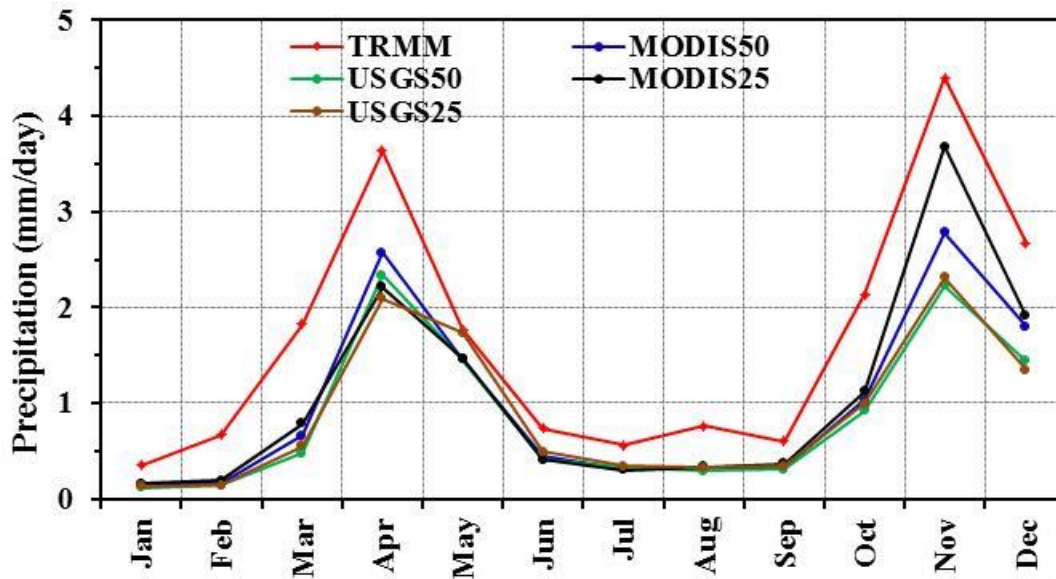


Figure III-12: Annual cycle of monthly averaged precipitation (in mm/day) spatially averaged over the study region for the period 2011-2014, derived from TRMM and the four WRF experiments

Seasonal totals and averages

The seasonal total amounts of spatially averaged precipitation, derived from the monthly time series, are shown in Figure III-13. There is diverse performance by the four WRF experiments during the MAM season and over the individual years. The total seasonal amounts for the period 2011-2014 for the four WRF experiments are: MODIS50 simulated 571 mm while USGS50 simulated 520 mm. MODIS25 simulated 544 mm while USGS25 simulated 534 mm. The corresponding total derived TRMM precipitation is 882 mm. The four WRF configurations simulated almost equal seasonal amounts over the individual years.

During OND season MODIS50 simulated 683 mm, while USGS50 simulated 559 mm. MODIS25 on its part simulated 817 mm, while USGS25 had 567 mm. These simulated seasonal amounts are compared to that derived from TRMM for the same period (2011-2014). MODIS25 consistently simulates more seasonal amounts that are closer to TRMM than MODIS50, USGS50 and USGS25. With spatial averaging, over the area covering the sub-regions designated as UT and LT (see study area, Figure I-1), the results are found to be similar to those described in Section III.5.2 for both MAM and OND.

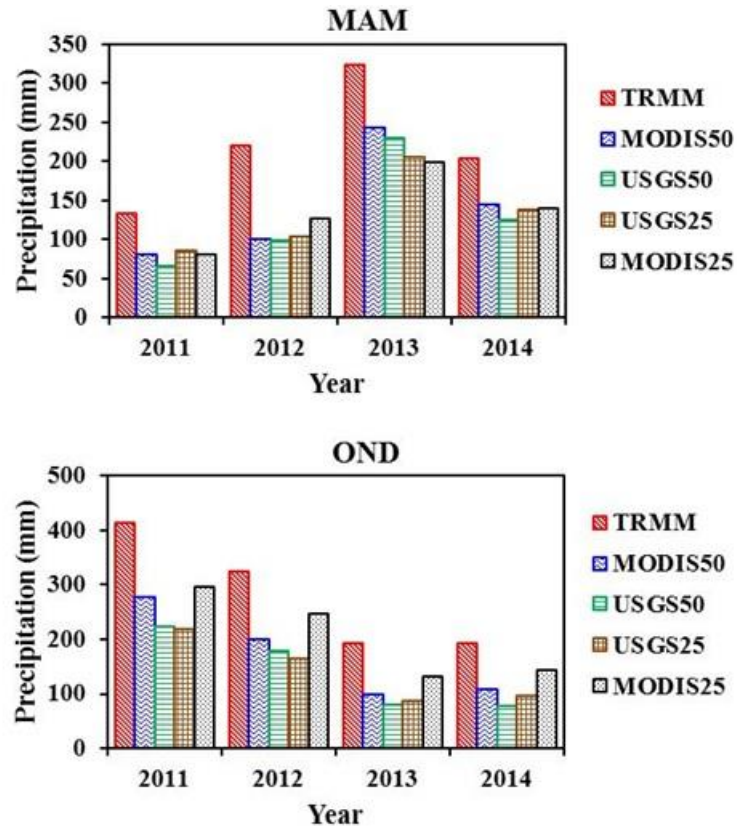


Figure III-13: Total seasonal (MAM, OND) amount of observed and simulated precipitation for individual years (2011-2014) spatially averaged over the study region

Interannual variability

In the case of spatially averaged precipitation, TRMM is taken as the baseline to check the interannual variability of the four WRF configurations. All WRF configurations show a reasonable magnitude of interannual variability though weakly in the USGS driven experiments (Figure III-14).

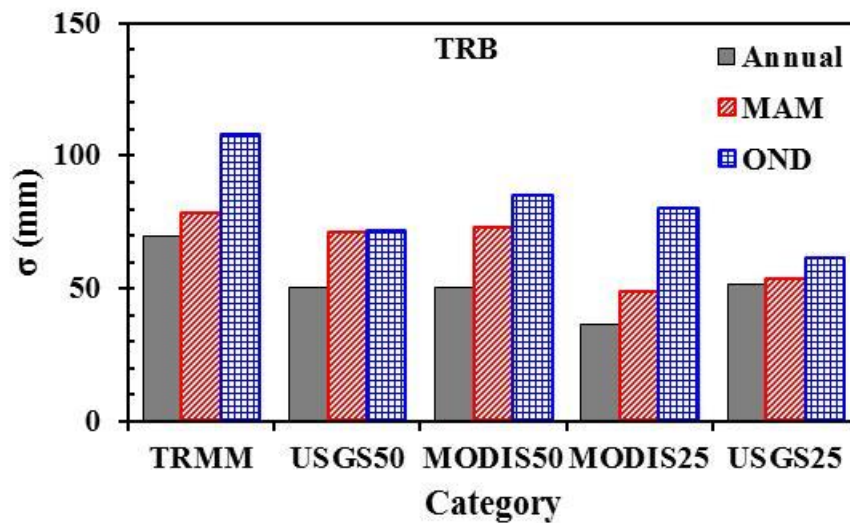


Figure III-14: Standard deviation of the annual, seasonal (MAM, OND), total precipitation during 2011-2014, spatially averaged over the study region. The precipitation is derived from TRMM and the four WRF configurations

Time averaged precipitation

MAM

Considering the time-averaged precipitation for individual years, during the MAM season (Figure III-15), the WRF model in all configurations is generally wetter along the lower parts south-west of the catchment (coastal strip) compared to TRMM. On the other hand, in the north-west (in the vicinity of Mt. Kenya, upper TRB) and middle of TRB, the WRF model is relatively drier than TRMM. In 2011, all WRF configurations are drier compared with TRMM in general, and more specifically in the middle parts of the TRB. During 2012 and 2013 all WRF experiments captured well the precipitation maximum, with MODIS25 displaying the closest patterns (relative to TRMM). In 2014, however, MODIS25 shows poor performance in the middle TRB.

OND

During OND season (Figure III-16), there is a closer spatial patterns compared to that observed in TRMM. All WRF experiments capture the precipitation maximum (north-west of the TRB), while being wetter along the lower TRB (coastal strip). The MODIS configurations (MODIS25 and MODIS50) are consistently wetter than USGS configurations (USGS25 and USGS50) which are in line with the results presented earlier. In

general, the simulated and observed precipitation shows a decline over the years, with 2011 being the wettest while 2013 and 2014 are drier among the four considered years.

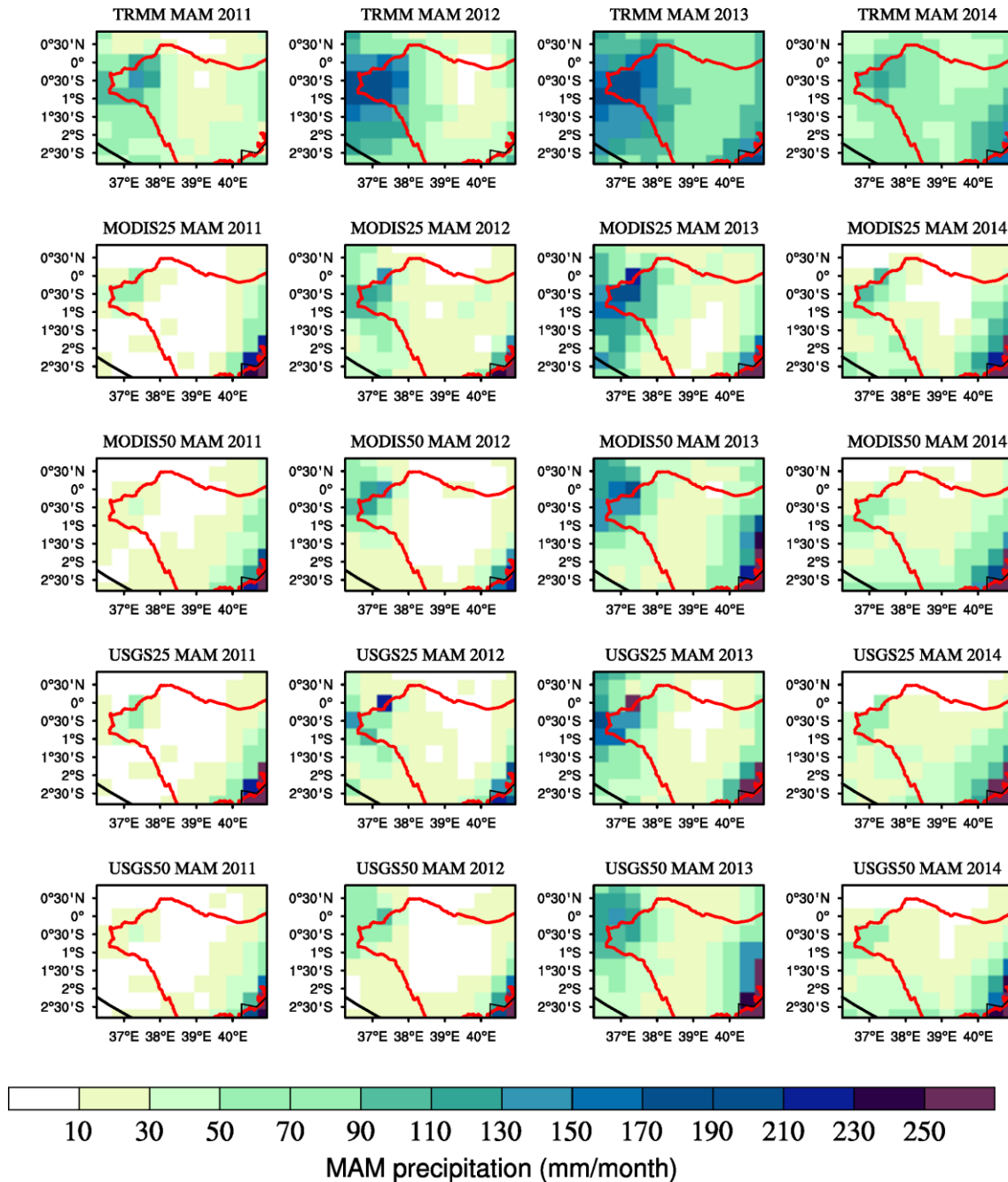


Figure III-15: Precipitation maps of the study area averaged for MAM season for the period 2011-2014, derived from (1st row) TRMM, (2nd row) MODIS25, (3rd row) MODIS50, (4th row) USGS25, and (5th row) USGS50. The red contour line delineates part of TRB boundary

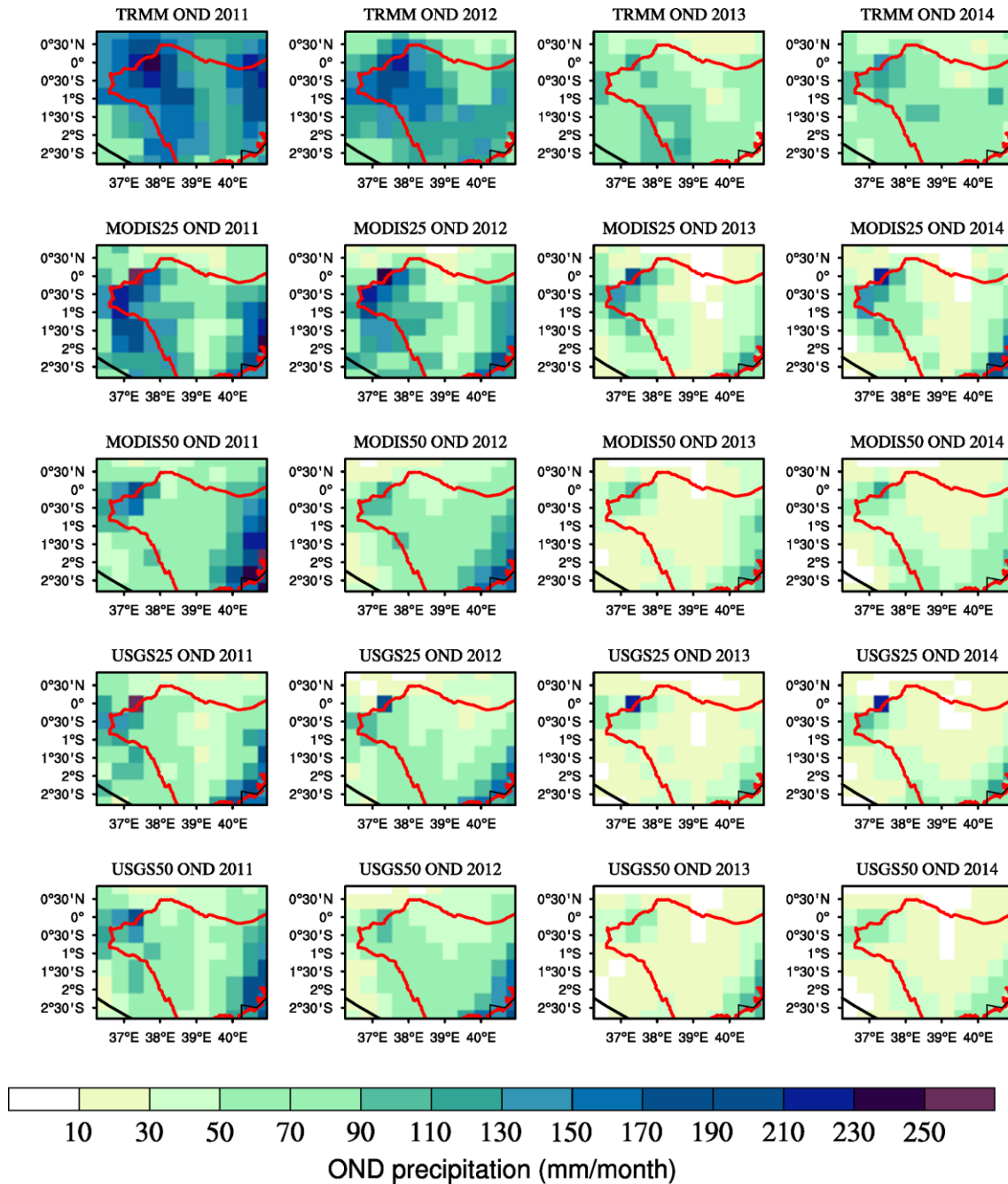


Figure III-16: Precipitation maps of the study area averaged for OND for the period 2011-2014, derived from (1st row) TRMM, (2nd row) MODIS25, (3rd row) MODIS50, (4th row) USGS25, and (5th row) USGS50. The red contour delineates part of TRB boundary

Statistical inference of the time averaged precipitation

A Taylor diagram based performance analysis (Taylor, 2001) is applied for an in-depth study of differences between modeled and observed precipitation shown in Figure III-15 and Figure III-16. Figure III-17, Figure III-18, and Figure III-19 show normalized

statistics i.e., the pattern correlation (r), root-mean-square (RMS) difference and the standard deviation (σ) of the seasonal mean rainfall of the four WRF experiments with respect to TRMM estimates for the period 2011-2014.

During MAM (Figure III-17) season of 2011, all the four WRF experiments had weak pattern correlations ($r < 0.2$). In 2012, there were fairly reasonable spatial pattern correlations ($r \approx 0.4$). The pattern correlations of the four WRF experiments were higher in 2013 and 2014, ranging from approximately 0.5 to 0.8, but showing diverse standard deviation ($1.8 \leq \sigma \leq 3.3$). MODIS25, in general, displayed the highest pattern correlations for the two years.

In case of OND (Figure III-18), all four experiments show similar performance in terms of spatial variability with standard deviations ($1 \leq \sigma \leq 2$) and pattern correlation ($r < 0.6$). Unlike during MAM, no clear inferences can be drawn for the different years.

Figure III-19 shows all MAM and OND season taking into account the monthly mean precipitation during the period 2011-2014. During the MAM season, all the four WRF experiments overestimated the magnitude of the interannual variation relative to TRMM with normalized standard deviations of approximately ($\sigma \approx 1.5$) and RMSE values of between 1 and 1.5. It is MODIS25 that showed a relatively high pattern of correlation ($r > 0.6$) and a lower normalized RMSE compared to the other experiments. In the case of OND, USGS50 showed the highest spatial variability and the lowest pattern correlation compared to USGS25, MODIS50 and MODIS25. The latter three experiments had similar equal normalized RMSE values. MODIS25 again showed a slightly higher pattern correlation.

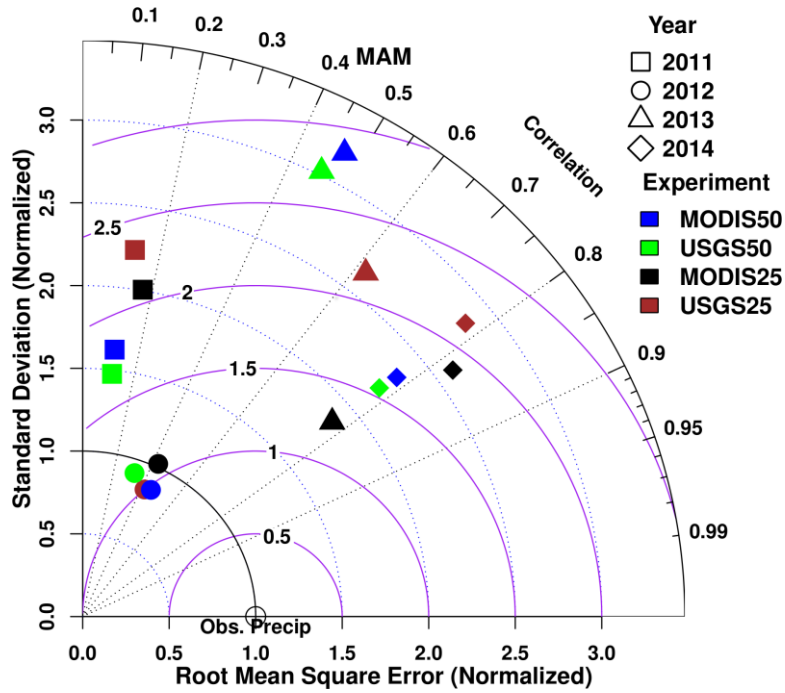


Figure III-17: Normalized pattern statistics during the MAM season derived the four WRF experiments: MODIS50, USGS50, MODIS25, and USGS25. The reference data (Obs. Precip) is derived from TRMM for the period 2011-2014

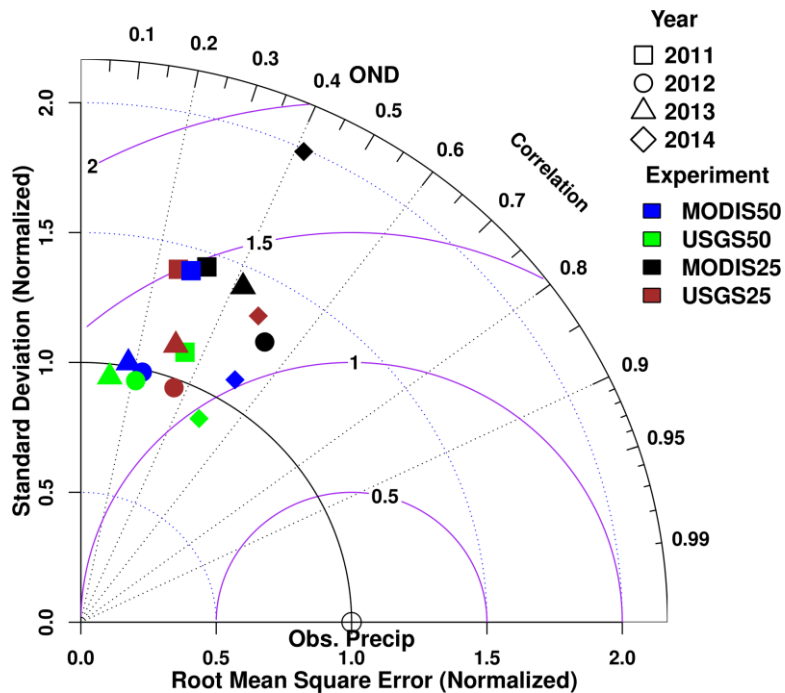


Figure III-18: Normalized pattern statistics during the OND season derived from the four WRF experiments: MODIS50, USGS50, MODIS25, and USGS25. The reference data (Obs. Precip) is derived from TRMM for the period 2011-2014

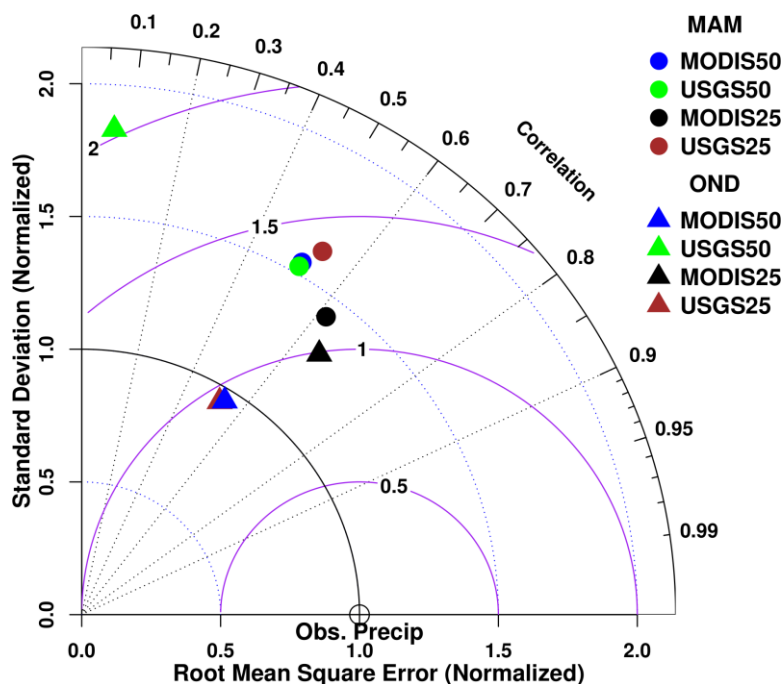


Figure III-19: Normalized pattern statistics showing the monthly mean over all March-May (MAM) and October-December (OND) derived from the four WRF experiments: MODIS50, USGS50, MODIS25, USGS25 in reference to TRMM data (Obs. Precip) for the period 2011-2014

III.6 Impact of land use and horizontal resolution on modeled temperature

This section is subdivided into two, whereby Section III.6.1 focuses on temperature simulation results versus station temperature while Section III.6.2 presents temperature simulation results versus CRU temperature over the TRB.

III.6.1 Model results versus station temperature

The results under this section are similar to those in Section III.4.1. The WRF model in the 4 configurations capture well the annual cycle of temperature compared to that observed at the respective stations with $r > 0.9$. The monthly mean temperatures as simulated in the four configurations are similarly colder compared to station temperatures with a MAE values between 1 °C and 5 °C. As discussed earlier, the WRF simulations accounted for the air temperature decrease with altitude. All the WRF configurations simulate the lowest temperatures over Nyeri, which is located at the highest altitude of all stations. The highest temperatures are simulated at Lamu, which is at the lowest

altitude. There is only little impact of the model horizontal resolution on the simulated temperatures. The biases of all WRF experiments are high, on average about 9 °C at Nyeri, 6 °C at Thika, 3 °C at Lamu, and 2 °C at Meru.

Interannual variability

Figure III-20 shows the interannual variability of annual and seasonal (MAM and OND) temperatures at the stations and that derived in WRF corresponding to the grid points of these stations. The station temperature data is taken as the reference dataset. There is diverse performance of the 4 WRF configurations in each of these stations. The capture of the interannual variability doesn't depend on the location or altitude of the station.

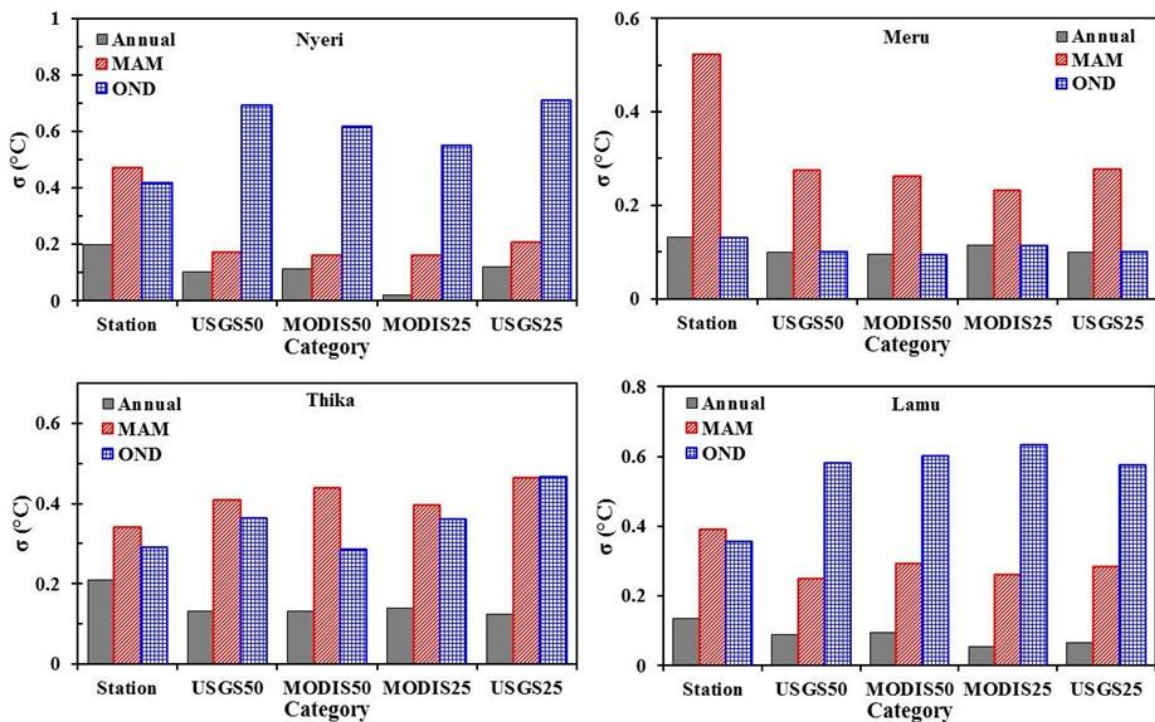


Figure III-20: Standard deviation of annual, seasonal (MAM, OND) mean temperature over selected stations in TRB during the period 2011-2014

In Meru and Thika, all the WRF configurations show reasonable magnitude of interannual variability with only USGS25 failing to capture the relative magnitudes of the annual, MAM and OND variability. In Nyeri and Lamu, it is an opposite scenario as all the 4 WRF configurations fail to capture the relative magnitudes of interannual variability. This illustrates the differences of the climatology that exist at very short distances in the TRB.

III.6.2 Modeled results versus CRU temperature

The spatially-averaged monthly mean temperature over the study region exhibit correlation coefficients of $r > 0.7$ for all the four WRF configurations, compared to CRU. All configurations capture reasonably the seasonality of monthly mean, maximum and minimum temperature. In line with the results for the stations, WRF simulates similar temperatures for the spatially-averaged series as seen earlier. There is a relative good agreement between CRU and the minimum temperature, but a significant (cold) bias can be found for maximum and mean temperature.

All the WRF configurations show similar spatial variability and amplitudes ($1 < \sigma < 1.2$, $0.2 < RMSE < 0.4$), over the years as well as having high correlation patterns of $r > 0.9$, (Figure III-21 and Figure III-22) following the time-averaged temperature over the study area. However, all the WRF configurations failed to capture the interannual variability of CRU in all cases (minimum, maximum and mean temperature).

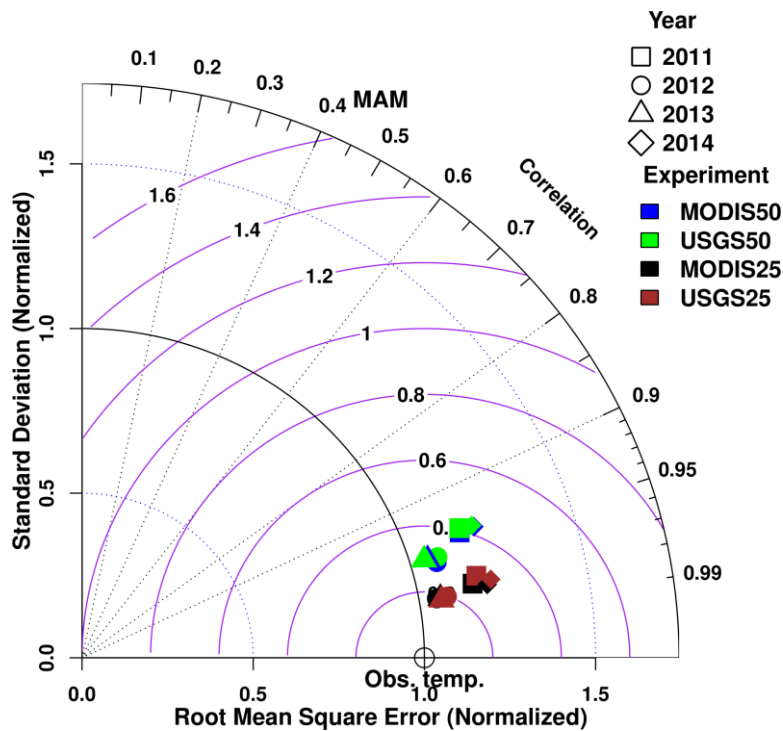


Figure III-21: Normalized statistical comparison of the spatially averaged mean temperature during MAM season over the study area for the period 2011-2014

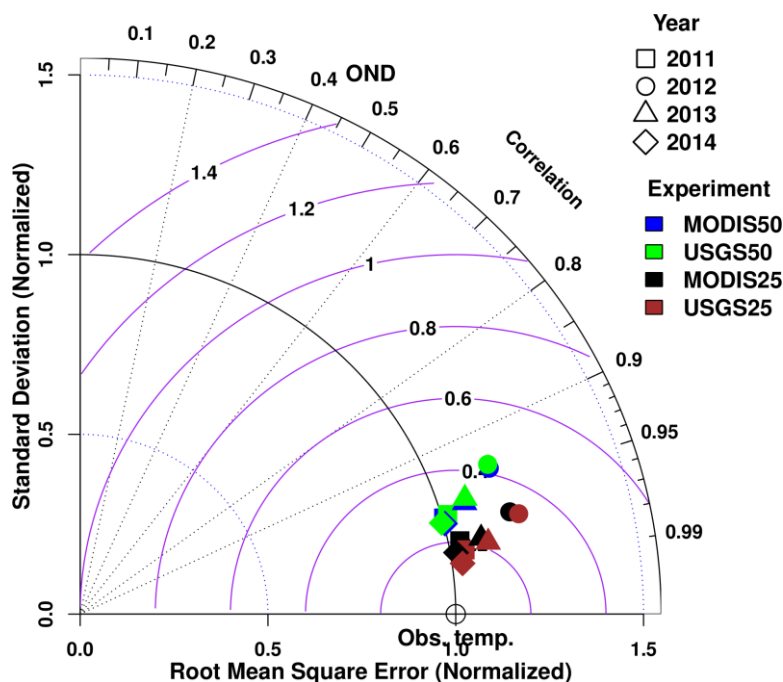


Figure III-22: Normalized statistical comparison of spatially averaged mean temperature during OND season over the study area for the period 2011-2014

III.7 Summary and discussion

The rainfall and temperature distribution of different sections of the TRB is summarized in climate diagrams following Walter-Lieth approach. This provides the basis of the precipitation and temperature climatology upon which the simulations of the WRF model is evaluated. Three cumulus and two microphysics parameterizations and one planetary boundary layer (i.e., $3 \times 2 = 6$ configurations) are investigated. All other parameterizations are same for all the configurations. All configurations yield more precipitation in the upper TRB compared to middle TRB. This shows that precipitation in WRF especially in this region is dependent on topography which is in agreement to earlier studies for African regions south of the Sahara (e.g., Jury *et al.*, 2007; Endris *et al.*, 2013). The KF, WSMS6, ACM2 (KWA) configuration provides the most reasonable results in terms of seasonal and annual amounts to those recorded at the stations and in particular in the upper TRB. This combination’s performance is in agreement with earlier studies for the East Africa region (e.g., Endris *et al.*, 2013; Pohl *et al.*, 2011). These earlier studies found the WRF model to overestimate precipitation. However, here the WRF model underestimates the observed precipitation. This could be attributed to the TRB having received below normal mean annual precipitation during 2011-2014 for the last 45 years (Kerandi *et al.*, 2016).

All configurations considered perform better during the OND season compared to the MAM season. There is clear overestimation of the precipitation in the lower TRB consistent with earlier studies (e.g., Pohl *et al.*, 2011). The results obtained in terms of spatial averaging using TRMM as the basis of evaluation are similar to that obtained for station data.

In case of temperature all the considered six configurations simulate similar temperature with a cold bias compared to both station and CRU temperature. The cold bias is very much pronounced in mean maximum temperature than in mean minimum temperature. The respective altitudes of the stations play a little role in reducing the bias.

The impact of model horizontal resolution (50 km and 25 km) and the land use (MODIS and USGS) is reflected in simulated precipitation and not in simulated temperature. All the four WRF model configurations reasonably reproduced the spatial and temporal evolution (seasonality) of both TRMM-derived precipitation and CRU-derived temperature over the TRB and surrounding areas. Significant cold bias as seen in the first set of six WRF experiments were also found using both the observation stations as well as CRU data, independently of the configuration. The limited accuracy in simulating temperature might not only be due to deficiencies of the WRF, but also due to deficiencies of the CRU dataset (interpolation problems) in representing the actual temperature in such a mountainous region with a low density of observation stations. In terms of precipitation, the MODIS25 revealed the closest correspondence to the observations.

IV WRF and WRF-Hydro: Sensitivity and performance at 5 km

IV.1 Introduction

The simulation results from the WRF-only and the coupled WRF-Hydro are discussed in this chapter. All simulation results are based on D2 which is at 5 km horizontal resolution (Figure IV-1). The area of study under focus (and also in subsequent chapters) is that of the Mathioya-Sagana subcatchment (MSS) and its surrounding as earlier indicated in Section I.5. This chapter starts with an overview of MSS characteristics before discussions on simulated precipitation and discharge. The precipitation simulation results are compared with station data and gridded satellite data (TRMM and CHIRPS). Most of the work in this chapter has been published in the Journal of Theoretical and Applied Climatology (Kerandi et al., 2017).

IV.1.1 Mathioya-Sagana subcatchment (MSS) area

The delineated Mathioya-Sagana subcatchment (MSS) is located to the northwest of the TRB. More specifically, it lies between 0°10' and 0°48'S and 36°36' and 37°18'E (Figure I-1; see Section I.5) covering an area of approximately 3279 km² (\approx 26.2 % of the entire upper TRB). According to the MODIS-based land-use classification data, it is characterized by the evergreen broadleaf forest, the savannas and woody savannas (Figure IV-1a). It has an elevation between 1000 and 4700 m.a.s.l. (Figure IV-1b). The subcatchment is served by mostly perennial tributaries which include: Sagana, Ragati, New Chania, Amboni, Mathioya, Gura, Gakira and Rukanga. All these tributaries are part of the Tana River drainage network that has its source at the slopes of Mount Kenya and the Aberdare Ranges. The Tana River is the longest river in Kenya stretching about 1012 km with an annual mean discharge of five billion cubic meters (Agwata, 2005). The river network of the MSS contributes immensely to the Tana River network. This is because these rivers are upstream of the entire TRB. The Rukanga River is most downstream of all these tributaries with the Tana Rukanga's river gauge station (RGS 4BE10; 0°43'53"S, 37°15' 29"E) located at the outlet of MSS. The Tana Rukanga's RGS 4BE10 discharge is used for calibration and evaluation of the relevant model in this study. The MSS area, like most parts of East Africa, receives its rainfall in the two known seasons of March, April and May (MAM) and October, November and December (OND). The monthly/annual temperatures over MSS are about 17°C or less (Kerandi *et al.*, 2016).

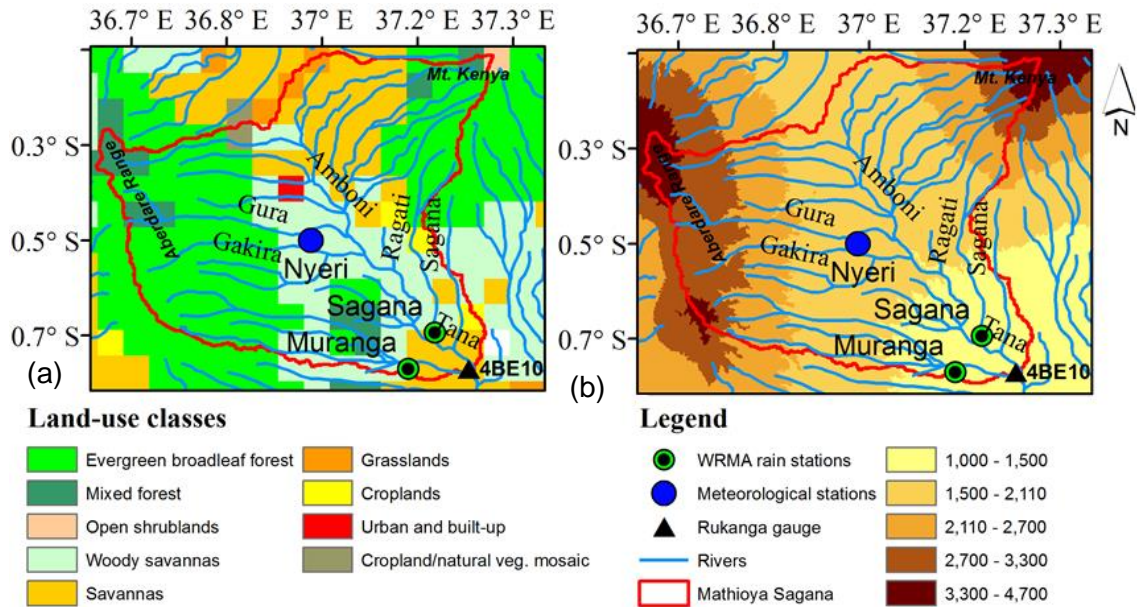


Figure IV-1: Mathioya-Sagana subcatchment (MSS; marked by red contour) and surrounding showing: (a) dominant land use classes based on MODIS, and (b) the digital elevation model (DEM), 90-m, 3 arc-second dataset. One meteorological station (Nyeri), two rain stations (Sagana, Murang'a), Tana Rukanga's RGS 4BE10 and river network in the MSS

IV.2 Precipitation

The simulation results are based mainly on how well the WRF-only and coupled WRF-Hydro modeling systems capture the observed seasonality, annual and interannual variation. The selected statistical measures to further explain these comparisons are presented in Appendix B: Statement of the objective criteria and other statistical measures.

IV.2.1 Model results versus station data

The precipitation from the three stations (Nyeri: -0.44° , 36.98° ; Murang'a: -0.72° , 37.15° and Sagana: -0.66° , 37.20°) over the MSS is compared to that derived from the corresponding WRF-only and coupled grid points. The precipitation amounts are all mean centered i.e., subtracting each value from the long term mean for the 4 years of the respective series. Figure IV-2 shows the resulting scatter plot in which all stations are compared to the nearest model grid point (located at -0.61° , 37.11°) between the three stations. There is a fair agreement between the shape of the three series: the simulated (WRF-only; coupled WRF-Hydro) and the observed (station data). This is an indica-

tion of the two modeling systems capturing well the seasonal and annual evolution of station precipitation. Both the coupled WRF-Hydro and the WRF-only slightly have same coefficient of determination R^2 on average, however with variation over individual stations. As these stations are located in a highly mountainous region, as expected, precipitation amounts vary at short distances. Further examination of the skill scores (SS) of the two models show that WRF-only is slightly inferior, $SS \approx 0.01$ compared to WRF-Hydro, $SS \approx 0.09$ when all station data is averaged. However, this is not any criteria to assume that the coupled WRF-Hydro is that superior to WRF-only compared to station data even though it posts fairer correlation coefficients in two of the three stations. Note that SS is similar to NSE i.e., the closer to 1, the better the model prediction.

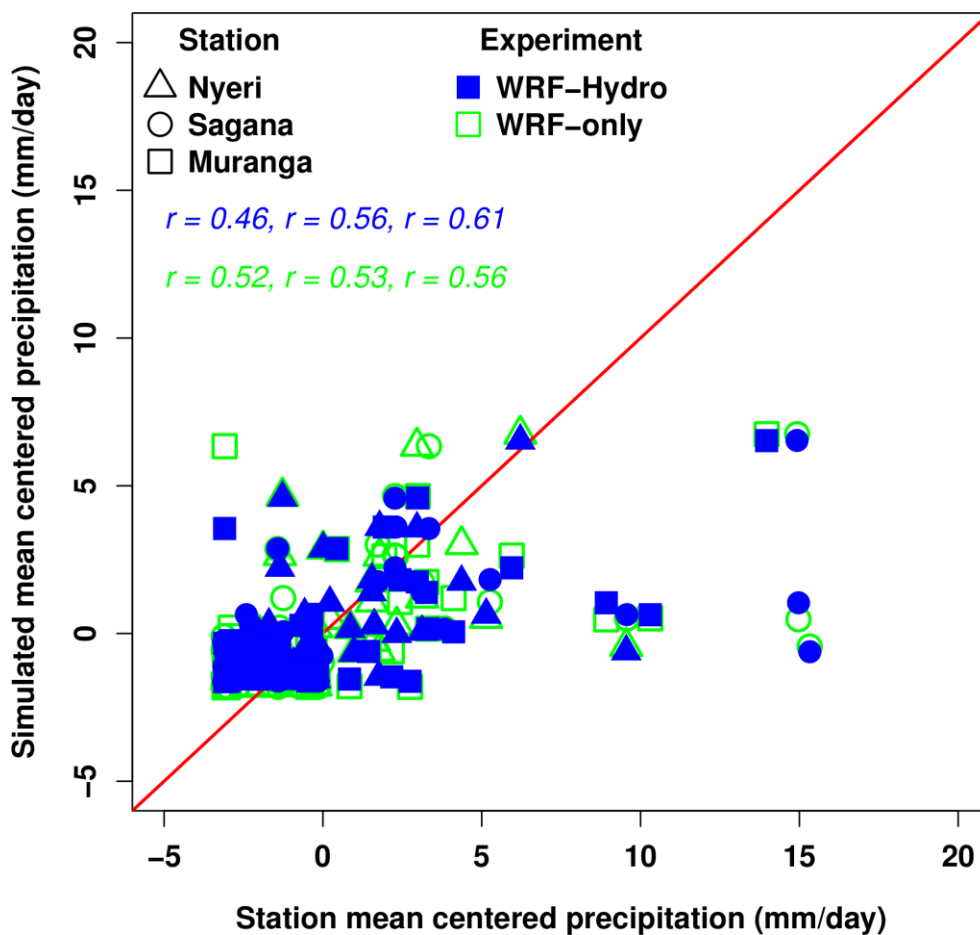


Figure IV-2: Scatter plot showing mean centered simulated (WRF-only, coupled WRF-Hydro) and stations (Nyeri, Muranga, Sagana) precipitation data over MSS for 2011-2014

Seasonal totals over the stations

Figure IV-3 shows the seasonal amounts derived from the two modeling systems and that from Nyeri, Murang’a and Sagana stations. During the MAM season, both WRF-only and coupled WRF-Hydro yield approximately 48 % of the station precipitation for the entire period of 2011-2014 on average. In general, the models underestimate the individual and all stations-averaged seasonal amounts consistently over the years. The performance is primarily poor in 2011 and 2012. In 2013, however, there is a fair agreement between the two models especially over Nyeri station. In the case of OND, albeit mixed performances, there is fair correspondence between both WRF-only and coupled WRF-Hydro with respect to the individual stations and averaged total precipitation over the stations. However, an opposite scenario to that of the MAM season is seen in 2013 in which both WRF-only and coupled WRF-Hydro do not perform better. This shows that the performance in the two seasons is independent from each other.

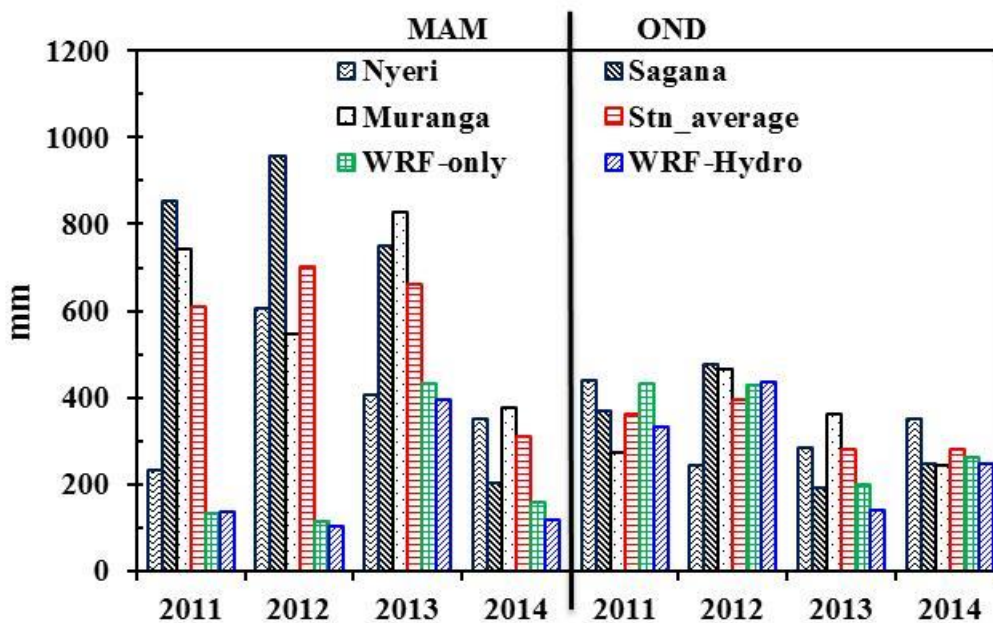


Figure IV-3: Seasonal totals (MAM, OND) amount of observed (station data) and simulated (WRF-only, coupled WRF-Hydro) for individual years during 2011 to 2014

IV.2.2 Model results versus gridded data

The model results from spatially averaged precipitation in WRF-only and coupled WRF-Hydro over the MSS and its surrounding forms the second category of experiments that

are compared with TRMM and CHIRPS. For easier comparisons, the simulated precipitation and that derived from CHIRPS are remapped onto the TRMM grid.

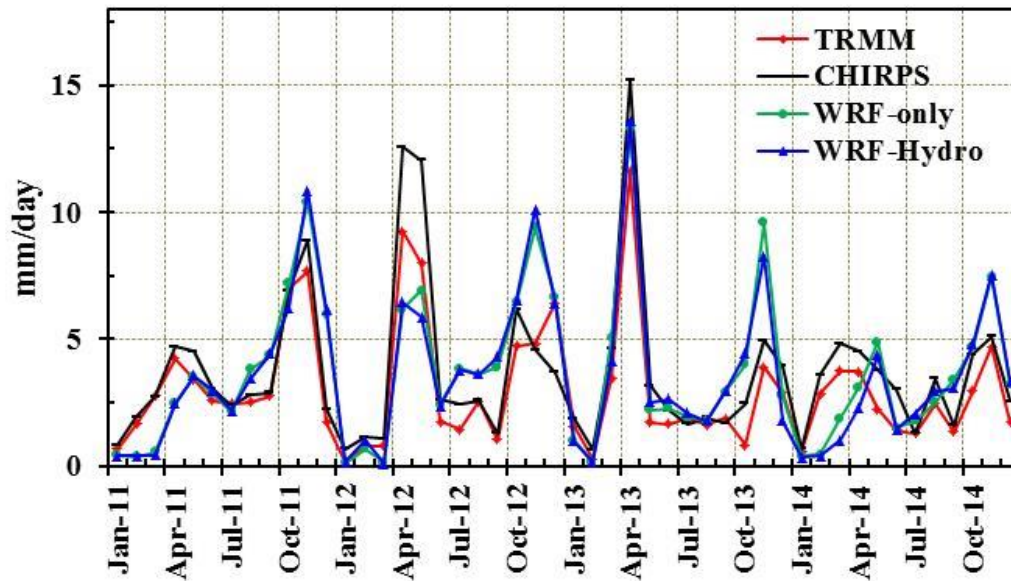


Figure IV-4: Time series of monthly precipitation (in mm/day) spatially averaged over MSS and its surrounding (see Fig. 4.1) for the period 2011-2014 derived from TRMM, CHIRPS, WRF-only and coupled WRF-Hydro

Figure IV-4 and Table IV-1 show the results of the generated monthly time series of both the simulated and observed precipitation. Both WRF-only and coupled WRF-Hydro capture quite reasonably the seasonal and annual cycle of precipitation with overall high correlations coefficients compared to the two observational datasets. The two modeling systems capture well the seasonal peak of OND as November but occasionally miss that of the MAM season by one month i.e., indicating it as May instead of April.

The values of the selected statistics for WRF-only and coupled WRF-Hydro compared to both TRMM and CHIRPS are modest and compare well between the two. The best performance is seen in 2013, being also the year when coupled WRF-Hydro has the best predictability (high skill score, $SS = 0.62$ and lowest $CV = 40\%$). These results are consistent to those obtained in Section IV.2.1.

Table IV-1: Selected statistics (mean absolute error, MAE, in mm/day; root mean square error, RMSE, in mm/day; correlation coefficient, r ; coefficient of variation, CV, in % and skill score, SS) for spatially averaged precipitation time series shown in Figure IV-4. The statistics in reference to CHIRPS (C) are indicated in blue, while those in reference to TRMM (T) are in black

		2011		2012		2013		2014	
		WRF-only	WRF-Hydro	WRF-only	WRF-Hydro	WRF-only	WRF-Hydro	WRF-only	WRF-Hydro
MAE	T	1.4	1.4	1.5	1.7	1.3	1.3	1.4	1.5
	C	1.3	1.4	2.2	2.4	1.1	1.2	1.4	1.5
RMSE	T	1.8	1.9	2.1	2.3	2.0	1.8	1.7	1.8
	C	1.7	1.7	3.0	3.3	1.6	1.5	1.7	1.9
r	T	0.79	0.76	0.78	0.73	0.90	0.91	0.56	0.49
	C	0.82	0.80	0.64	0.58	0.90	0.92	0.53	0.46
CV	T	61	64	69	76	68	61	57	59
	C	44	47	82	88	44	40	46	51
SS	T	0.25	0.21	0.15	0.06	0.16	0.25	0.30	0.27
	C	0.45	0.43	0.00	-0.07	0.46	0.62	0.44	0.38

IV.2.3 Seasonal and cumulative totals

The total seasonal precipitation is based on the two rainy seasons of MAM and OND. The sum of the seasonal amounts i.e., $P_{MAM} + P_{OND}$ is an indicative of the average annual precipitation for the given year for the region assuming that no or negligible precipitation is recorded in the dry months. Both models capture well the variability of the two rainy seasons over the MSS and its surrounding. The simulated total seasonal precipitation for the four years (2011-2014) is more than that derived from TRMM but slightly less than that derived from CHIRPS. The respective total amounts are TRMM = 3180 mm, CHIRPS = 3956 mm, WRF-only = 3906 mm and WRF-Hydro = 3758 mm as shown in Figure IV-5 (top). During MAM, the models underestimate the observed precipitation in both TRMM and CHIRPS especially in 2011 and 2012. The simulated amount is slightly closer that derived in CHIRPS in 2013 while coupled WRF-Hydro underestimates the 2014 rains. In general, during this season, the models show a good capture of seasonal variability over the years albeit with a drier bias. During OND, both WRF-only and WRF-Hydro consistently overestimate the observed precipitation in TRMM and CHIRPS. This is consistent with results discussed in Section IV.2.1. The models also capture well the OND seasonal variability over the years though with a wet bias.

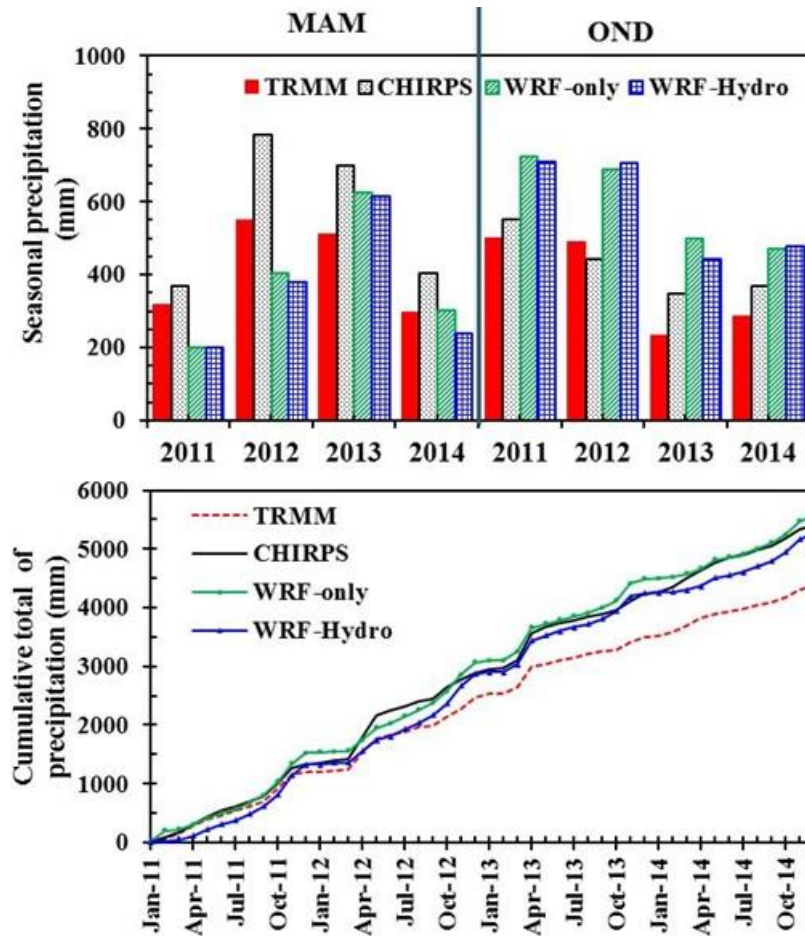


Figure IV-5: (Top) Total seasonal (MAM + OND), and (bottom) cumulative total precipitation derived from TRMM and CHIRPS and simulated in WRF-only/coupled WRF-Hydro during 2011 to 2014

Figure IV-5 (bottom) displays the cumulative total of precipitation as derived from the two models and derived from the two satellite datasets. The results show that WRF-only yields more precipitation (5567 mm) compared to the coupled WRF-Hydro (5271 mm). As stated earlier, both models yield more precipitation compared to that derived in TRMM (4369 mm) in excess of approximately 27 % and 24 % respectively. This is not the case compared to CHIRPS (5408 mm), whereby there is a closer agreement in the cumulative totals over the years. With the latter gridded dataset, WRF-only (coupled WRF-Hydro) overestimate (underestimate) it by about 2 %.

IV.2.4 Interannual variability

The two models' ability to mimic both the pattern and amplitude of the observed inter-annual variation is presented in the Taylor diagrams (Figure IV-6 and Figure IV-7). The

two figures summarize the normalized statistics of correlation coefficient r , standard deviation σ and root mean square error $RMSE$ of the seasonally simulated precipitation in the individual years compared to that derived from CHIRPS.

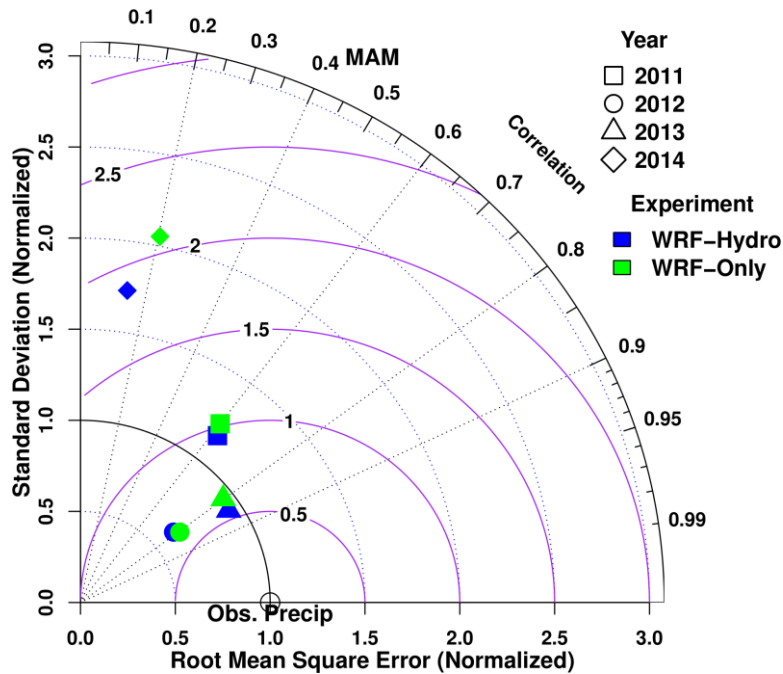


Figure IV-6: Taylor diagram showing pattern correlation r , normalized standard deviation σ and normalized root mean square error $RMSE$ for monthly mean precipitation simulated in WRF-only and coupled WRF-Hydro compared to CHIRPS (observed precipitation) during MAM season for individual years

During MAM (Figure IV-6), there is a mixed performance over the years in the two models. However, as seen earlier (Section IV.2.2), WRF-only and coupled WRF-Hydro display similar pattern in terms of the considered statistics. In 2011 and 2014 the models show a higher variability than in CHIRPS and low correlation coefficients ($r < 0.6$). In 2012 and 2013 both WRF-only and coupled WRF-Hydro underestimate the magnitude of the interannual variability. They, however, have a reasonable correlation coefficient ($r \approx 0.8$) and a low $RMSE$. In general, both WRF-only and coupled WRF-Hydro captures reasonably the magnitude of interannual variability variation relative to CHIRPS with low $RMSE$ and low amplitudes.

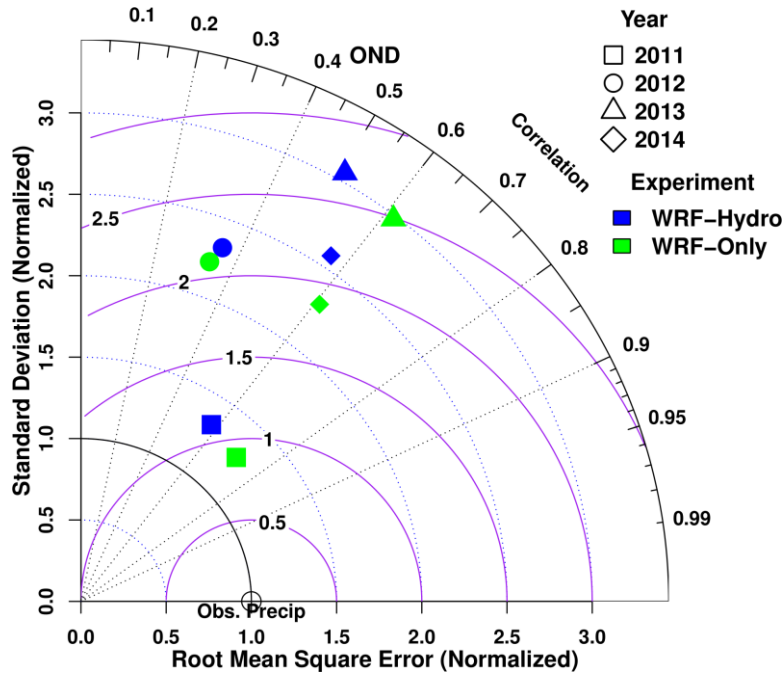


Figure IV-7: Taylor diagram showing pattern correlation r , normalized standard deviation σ and normalized root mean square error $RMSE$ for monthly mean precipitation simulated in WRF-only and coupled WRF-Hydro compared to CHIRPS (observed precipitation) during OND season for individual years

In the case of OND (Figure IV-7), there is a wide spread performance over the years with generally high spatial variability and low correlation coefficients ($r \leq 0.6$). The two models also overestimate the interannual variation of CHIRPS consistent with earlier discussion in the previous section. In 2011 both WRF-only and coupled WRF-Hydro show more reasonable correlation coefficient (WRF-only, $r \approx 0.7$; coupled WRF-Hydro, $r \approx 0.6$) and low $RMSE$.

IV.2.5 Spatial precipitation over the Mathioya-Sagana sub-catchment

The results discussed in this section are specific to the delineated Mathioya-Sagana subcatchment (MSS). The observed seasonal spatial maps for MAM and OND averaged for the 4 years (2011-2014) over MSS are shown in Figure IV-8.

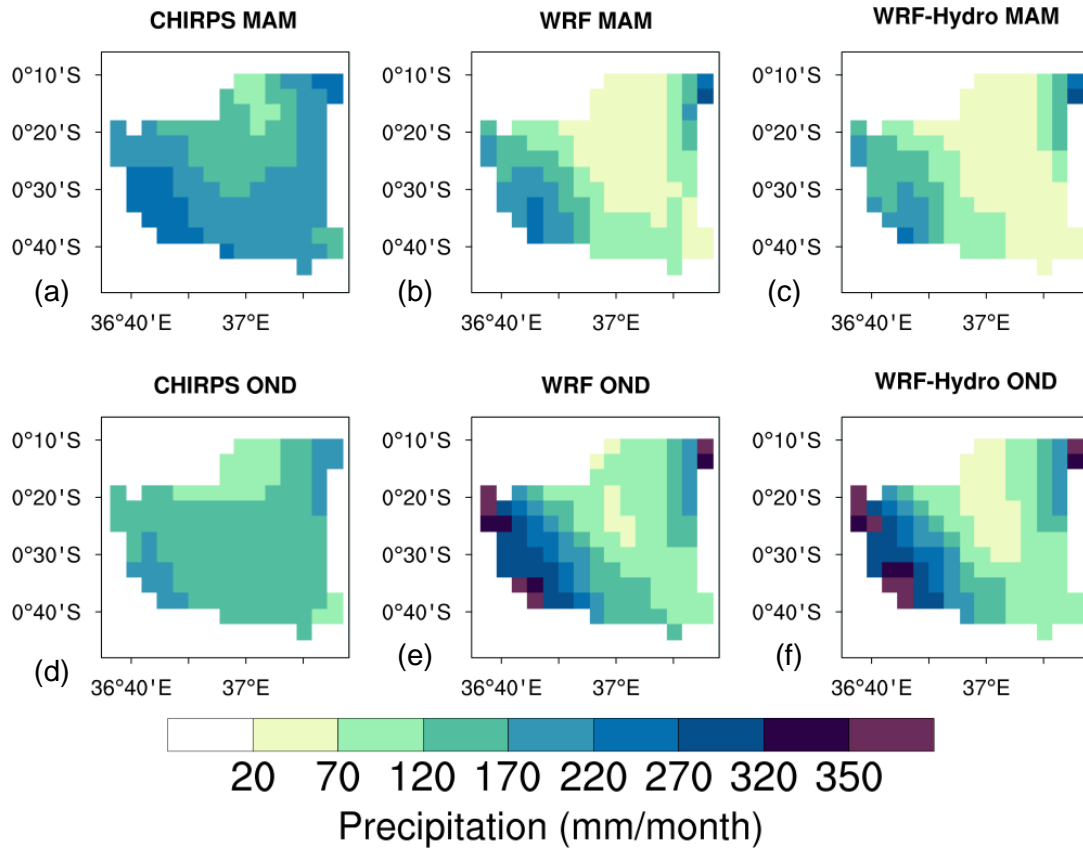


Figure IV-8: Precipitation maps of MSS region averaged for all MAM and OND seasons during 2011-2014: (a-c) MAM (d-f) OND. The first column represents CHIRPS, 2nd column represents WRF-only, and 3rd column represents coupled WRF-Hydro

There is a clear distinction between the two seasons in which the models overestimate the OND precipitation compared to CHIRPS while they grossly underestimate that of MAM season consistent with results presented in Sections IV.2.1 to IV.2.3 . Even so, a clear dependence of precipitation on topography is depicted as the models yield more precipitation in the West of the catchment an area where the Aberdare ranges are located.

IV.3 Coupled WRF-Hydro simulated discharge versus observed discharge

The coupled WRF-Hydro simulated river discharge is compared to that of observed discharge at Tana Rukanga's RGS 4BE10 for 2011-2014. As in all simulation results in this study, a two months (Nov-Dec 2010) spin-up is allowed for the model to reach its equilibrium. The coupled WRF-Hydro model utilizes the calibrated values for the selected parameters (see Section II.6). The coupled WRF-Hydro model is evaluated the

same way as the uncoupled WRF-Hydro using graphical and selected objective criteria of NSE and RSR whose formulation is presented in Appendix B: Statement of the objective criteria and other statistical measures

Figure IV-9 shows the hydrograph of observed and simulated discharge at a daily resolution and the corresponding hyetograph as simulated from coupled WRF-Hydro over the MSS during 2011 to 2014. The simulated and observed discharge are fairly correlated (the 2011-2014 correlation coefficient, $r \approx 0.52$) with occasional lagging of simulated peaks to those observed.

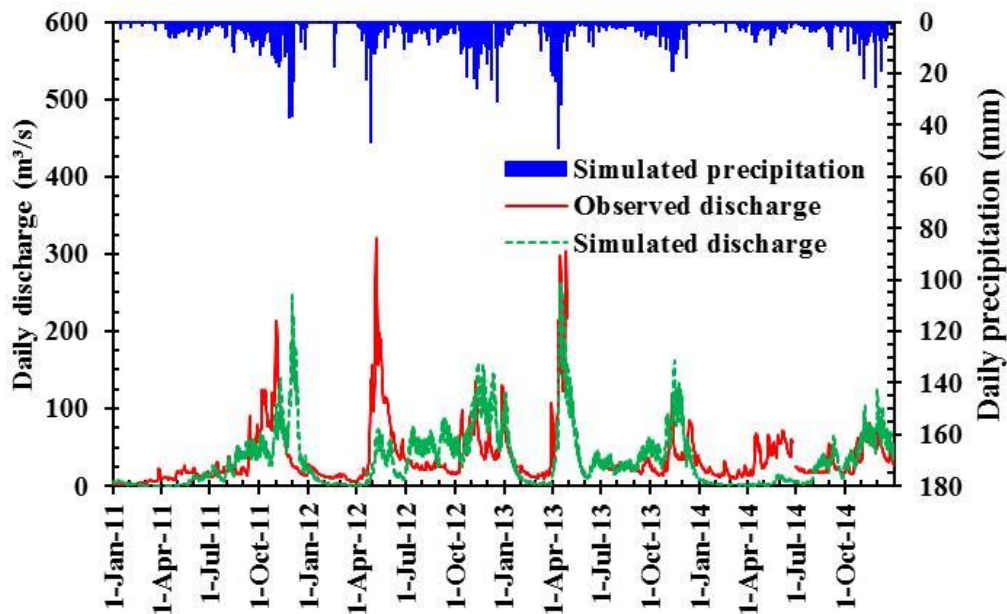


Figure IV-9: Observed and simulated (coupled WRF-Hydro) hydrographs and hyetograph in the MSS for the period 2011 to 2014 at 4E10 gauge station

There is a clear correspondence of the observed and simulated discharge as a response to the rain storms in the region. There is a linear relationship between discharge and precipitation over the catchment (correlation coefficient r of 0.81). The derived statistics from the simulated and observed series are shown in Table IV-2.

Figure IV-10 shows further comparison of the simulated and observed discharge at daily and monthly time steps based on linear regression with values of the y-intercept and coefficient of determination (R^2) indicated.

Table IV-2: Selected statistics (Nash-Sutcliffe efficiency, NSE and the RMSE-observations standard deviation ratio, RSR) between discharge in coupled WRF-Hydro and observed at 4BE10 gauge during the period 2011-2014

	2011-2014	2011	2012	2013	2014
	Daily time step				
NSE	0.02	-0.17	-0.21	0.49	-1.02
RSR	0.99	1.08	1.10	0.71	1.42
	Monthly time step				
NSE	0.15	0.35	-0.85	0.71	-1.43
RSR	0.91	0.77	1.30	0.51	1.49

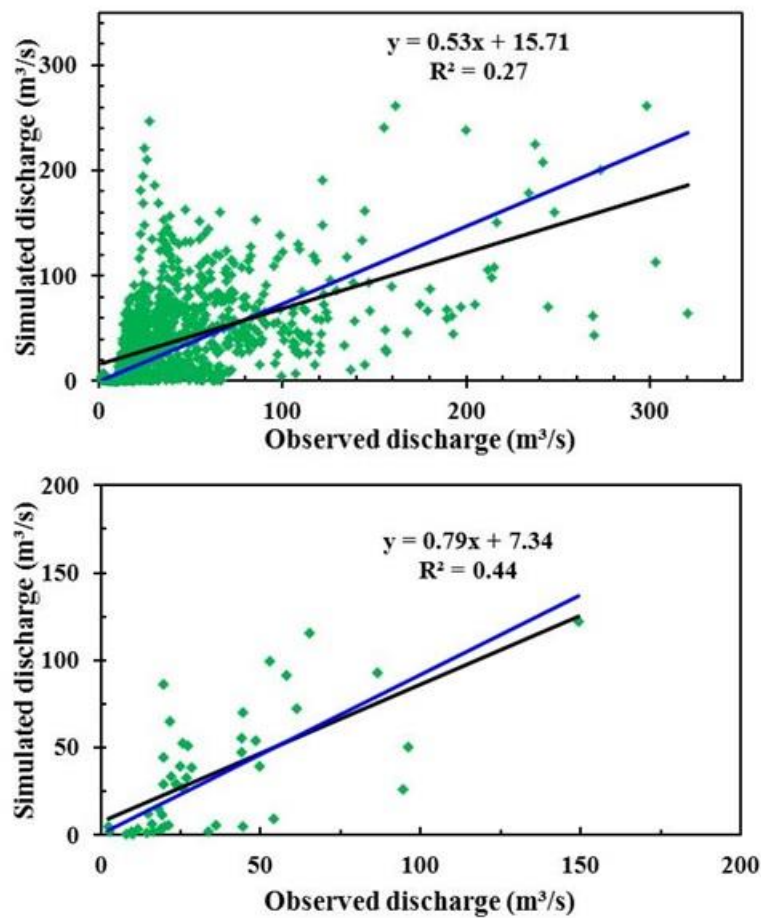


Figure IV-10: Scatter plot showing comparison of simulated and observed discharge (a) daily time step (b) monthly flow for the period 2011-2014 at Tana Rukanga’s RGS 4BE10. The blue line is the 1:1 line whose intercept is set at 0.0

At daily time step, the value of R^2 is found to be 0.27 while the NSE is 0.02 for the period 2011-2014. These low values are also indicative of the model’s underestimation of the high flows especially during the April, May, June (AMJ) season. Clear underestima-

tion is well pronounced for May in the years 2011, 2012 and 2014. This translates to poor performance of the model over these years as shown by the respective NSEs and RSRs values. The model reasonably captures the high flows of MAM 2013 and those of OND season. Overall the year 2013 recorded the best performance with a total of 300 days with full observed discharge (Figure IV-11). The good performance in 2013 is consistent with results for precipitation in which the models had a similar performance compared to that from the gridded datasets.

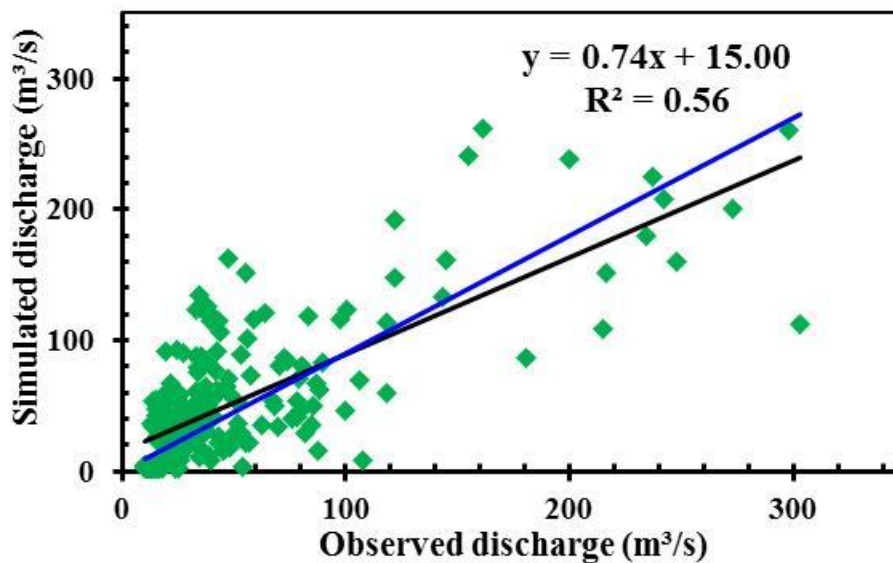


Figure IV-11: Scatter plot showing comparison of simulated and observed discharge in the year 2013 at Tana Rukanga’s RGS 4BE10. The blue line is the 1:1 line whose intercept is set at 0.0

Further results show a reasonable correspondence between simulated and observed accumulated discharge (Figure IV-12). The total volume of discharge observed at Tana Rukanga’s 4BE10 gauge during this period was 1658 m³ while the corresponding simulated discharge is approximately 1596 m³ i.e. only approximately 3 % difference.

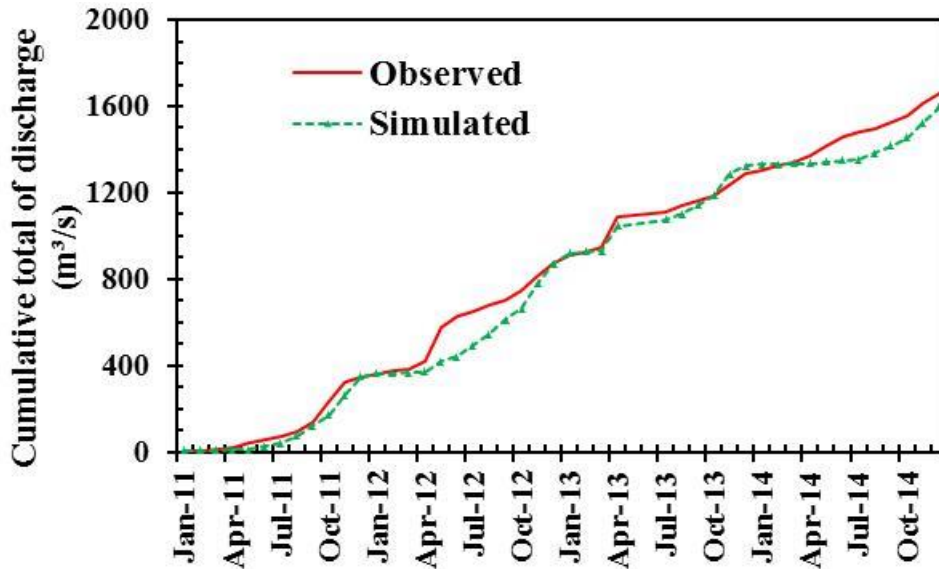


Figure IV-12: Cumulative totals of simulated and observed discharge at Tana Rukanga's RGS 4BE10 for the period 2011-2014

IV.4 Summary and discussion

As seen in Chapter 3, the WRF-only model at 25 km horizontal resolution and based on the MODIS land use produced precipitation results that were closest that derived from station data and TRMM. In this chapter, further investigations of the WRF-only model at a higher resolution, i.e., 5 km and based on D2 was carried out. The WRF-only results are compared to that of the coupled WRF-Hydro model. An analysis of the simulated and observed discharge at the 4BE10 gauge is also presented.

WRF-only and coupled WRF-Hydro exhibit similar skill in reproducing the stations (located over MSS) and that from the gridded satellite derived precipitation. The two models underestimate the MAM seasonal precipitation but closely match that of the OND season.

In case of the spatially averaged precipitation, simulated precipitation from both WRF-only and coupled WRF-Hydro is closer to CHIRPS than to TRMM. This may be attributed to the high horizontal resolution of the new CHIRPS (5 km) compared to TRMM (25 km), meaning TRMM could not be able to resolve the orographic features causing precipitation at this resolution. There are no discernable differences between WRF-only and coupled WRF-Hydro results in the monthly evolution, seasonal amounts and interannual variability. The two models underestimated the MAM seasonal precipi-

tation but overestimated that of OND. This is more pronounced in the mountainous regions in the West of the MSS where the Aberdare Ranges are located. It is clear that this region receives more precipitation as is expected. These results differ from those of Givati *et al.* (2016) and Senatore *et al.* (2015) who found that the coupled WRF-Hydro was better in yielding amount closer to observations in their regions.

Results of coupled WRF-Hydro simulated discharge compared to that recorded at the Tana Rukanga's RGS 4BE10 show a reasonable agreement. However, there is noticeable lagging and underestimation of the high peak flows, and hence a low NSE. The low NSE values are different from those obtained from the uncoupled WRF-Hydro. This is consistent with earlier studies (Senatore *et al.*, 2015; Givati *et al.*, 2016). Besides, the result from this study takes into consideration a longer period of 4 years than any of the named previous studies. It is seen in this study that some individual years can post very bad results (e.g. 2011, 2012, 2014) while others very good results (e.g. 2013; Table IV-2). On the other hand, there is a good relationship and response of the simulated hydrographs to that of the rain storms. The good performance in 2013 is a response towards good agreement in the simulated precipitation and that derived from CHIRPS. Further results show that the coupled WRF-Hydro model cumulative totals discharge are in good agreement with that recorded at the RGS 4BE10. This shows that the problem with the coupled WRF-Hydro does not lie in the total simulated discharge, but in capturing the timing and magnitude of the peak discharge.

In general, the models simulate reasonably well the seasonal, annual and interannual variability of both precipitation and discharge in the MSS and its surrounding.

V Terrestrial Water Balance for Mathioya-Sagana Subcatchment

V.1 Introduction

In Chapter IV the focus was on precipitation and discharge which are two major components of the terrestrial water balance (TWB). The TWB components are related as defined in Equation II-1. This chapter discusses on the characteristics of these components. In particular, the seasonal and interannual variation of precipitation (P), evapotranspiration (ET), discharge (R), and change in terrestrial water storage (dS/dt) over the Mathioya-Sagana subcatchment (MSS) and its surrounding are presented here.

The simulated TWB components are processed from the WRF-only and coupled WRF-Hydro modeling systems. P , ET and R are directly derived from the model outputs while dS/dt is calculated as a residue of P , ET and R i.e., $dS/dt = P - (ET+R)$. There are two other methods of estimating dS/dt which include firstly, in terms of soil moisture and groundwater components, and secondly, estimation from the atmospheric water balance components that are discussed in Chapter VI. The total runoff for the case of WRF-only is computed from the sum of surface and underground runoff.

Prior to inter-model comparisons between WRF-only and coupled WRF-Hydro, an evaluation of ET gridded datasets (GLEAM) is presented. The evaluation is based on comparison of the three GLEAM datasets and simulated ET from WRF-only and coupled WRF-Hydro. There are no in-situ ET observations available for this study and the gridded datasets are used instead. The validation and evaluation of P and R was presented in Chapter IV. An “adapted observations” of dS/dt is determined from the observations/gridded datasets of P , ET and R . Similar approaches of estimating or deriving dS/dt based on available datasets has been used in e.g., Draper and Mills (2008) and Yeh and Famiglietti (2008). The adapted observed dS/dt form part of observational datasets to evaluate its counterpart derived from simulated components. This approach is also followed in this chapter. Most of the work in this chapter has been published in the Journal of Theoretical and Applied Climatology (Kerandi *et al.*, 2017).

V.2 The Global Land Evaporation Amsterdam Model (GLEAM) and simulated ET

For comparison purposes, *ET* from the three datasets (i.e., GLEAM_v3.0a, GLEAM_v3.0b and GLEAM_v3.0c) and that simulated from WRF-only and coupled WRF-Hydro are remapped onto the grid of GLEAM_v3.0a.

Figure V-1 shows spatial maps of the 4-year mean annual evapotranspiration *ET* over the inner domain D2 as derived from the GLEAM datasets and simulated in WRF-only and coupled WRF-Hydro. All the GLEAM datasets agree reasonably well in their display of the spatial patterns of the time averaged *ET* over the whole of D2. WRF-only and coupled WRF-Hydro fairly captures these patterns reasonably well with however underestimations. For instance, the models capture the *ET* maximum zone in the northwest of upper TRB in agreement with the three GLEAM datasets. The regions with less *ET* on average lie to the east of upper TRB.

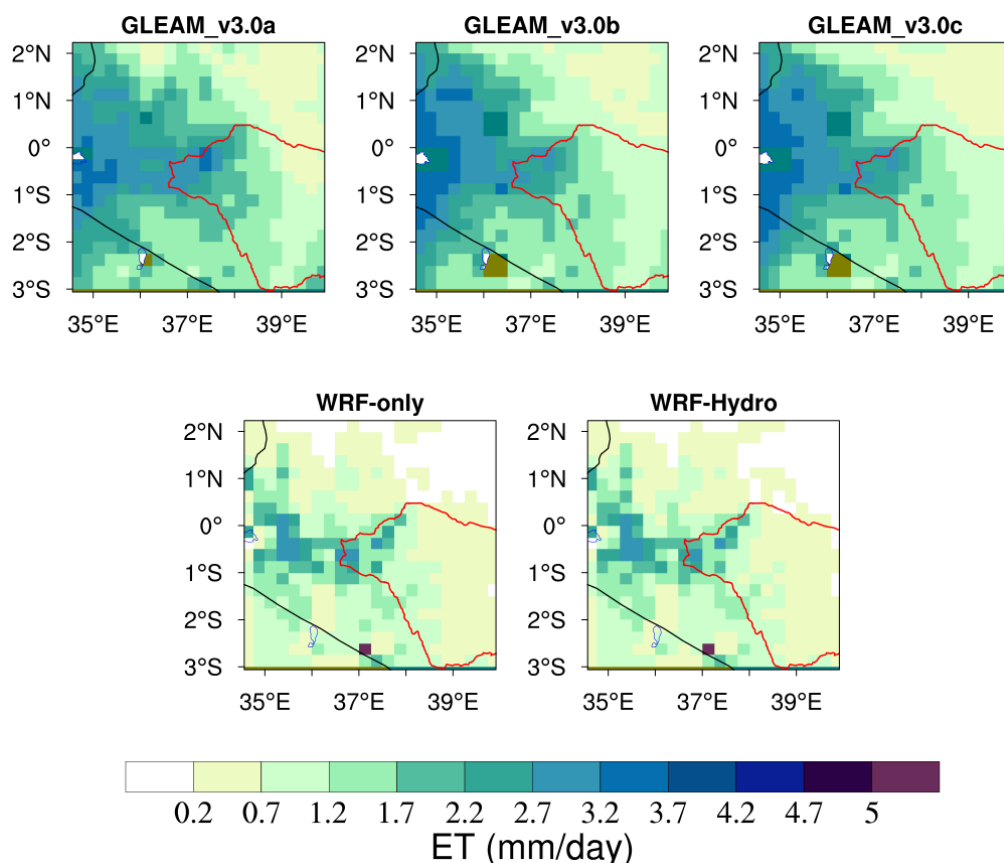


Figure V-1: Evapotranspiration maps spatially averaged over the inner domain (D2) for the period 2011-2014, derived from the GLEAM datasets (row 1) and simulated in WRF-only and coupled WRF-Hydro (row 2). The red contour delineates portion of the TRB

The spatial maps results are summarized in the Taylor diagram (Figure V-2). The models are significantly correlated; $r \geq 0.50$, $p < 0.001$ and have a normalized standard deviation σ and root mean square error $RMSE$ of 1.0. The two models are thus capable of reliably simulating ET over this region.

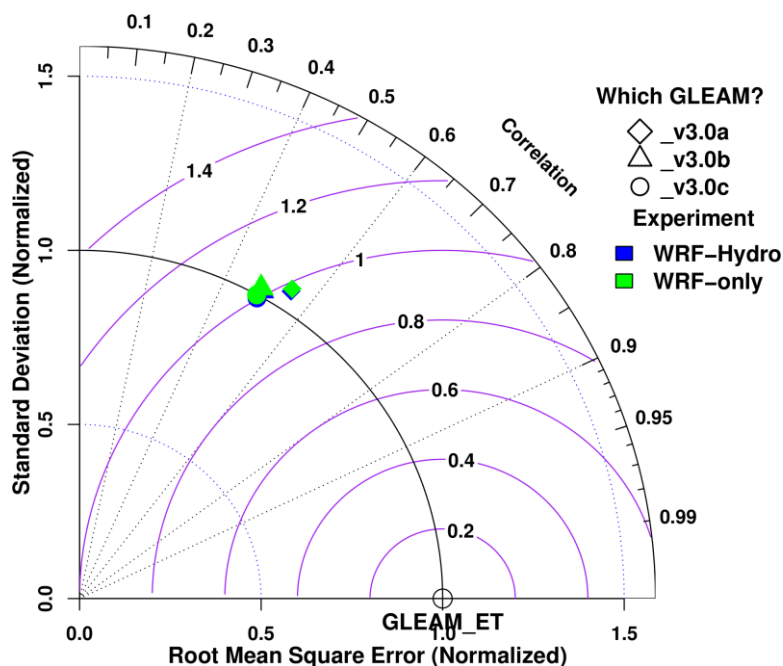


Figure V-2: Normalized pattern statistics of comparison of time averaged ET between that derived from GLEAM datasets and simulated by WRF-only and coupled WRF-Hydro for the inner domain during 2011-2014

Based on the foregoing description on these datasets and how they compare with simulated ET , any of the GLEAM datasets can be utilized for further studies involving ET in the region. However, further analysis of spatially averaged ET over MSS and its surrounding is done to identify one which agrees more with the simulated ET . Figure V-3 displays the scatter plot with regression line and R^2 that compares the mean centered values of ET from the three datasets and that derived from the simulations in WRF-only and coupled WRF-Hydro. The WRF-only exhibits slightly higher R^2 than coupled WRF-Hydro consistently with better explained variability of GLEAM_v3.0b dataset. In general, both WRF-only and coupled WRF-Hydro shows a closer agreement with GLEAM_v3.0b. GLEAM_v3.0b is thus considered in subsequent discussions.

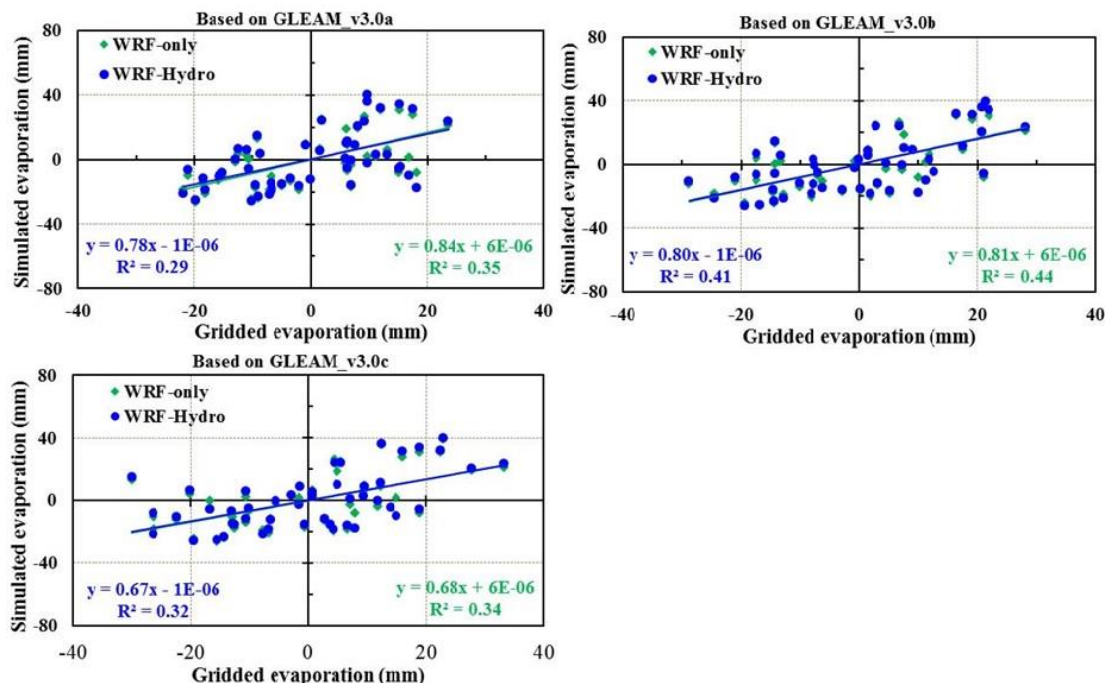


Figure V-3: Scatter plot of the mean centered monthly sum of *ET* derived from GLEAM datasets (GLEAM_v3.0a, GLEAM_v3.0b and GLEAM_v3.0c) compared to that simulated in WRF-only and coupled WRF-Hydro spatially averaged over MSS and its surrounding for the period 2011 to 2014

V.2.1 Interannual variability of *ET*

The monthly and interannual variation of simulated *ET* and that derived in GLEAM_v3.0b is displayed in Figure V-4. The two models capture reasonably the peaks and troughs of the gridded datasets. The simulated *ET* from both WRF-only and coupled WRF-Hydro are well correlated in temporal evolution (WRF-only: $r(46) = 0.65$, $p < 0.001$; coupled WRF-Hydro: $r(46) = 0.63$, $p < 0.001$). The peak months fall between December and January and also during April to May, while lowest values occur during the months of March and August. The highest values thus correspond to the time immediately after when the rainy seasons is ending while the lowest values occur before the onset of the rainy seasons. The 4-year mean of the three series are: GLEAM_V3.0b = 2.6 mm/day, WRF-only = 2.2 mm/day, and coupled WRF-Hydro = 2.1 mm/day. There is no much difference between observed and simulated *ET* based on these mean annual values. However, it is seen that the models slightly underestimate the observed *ET* consisted with the results highlighted in Section V.2.

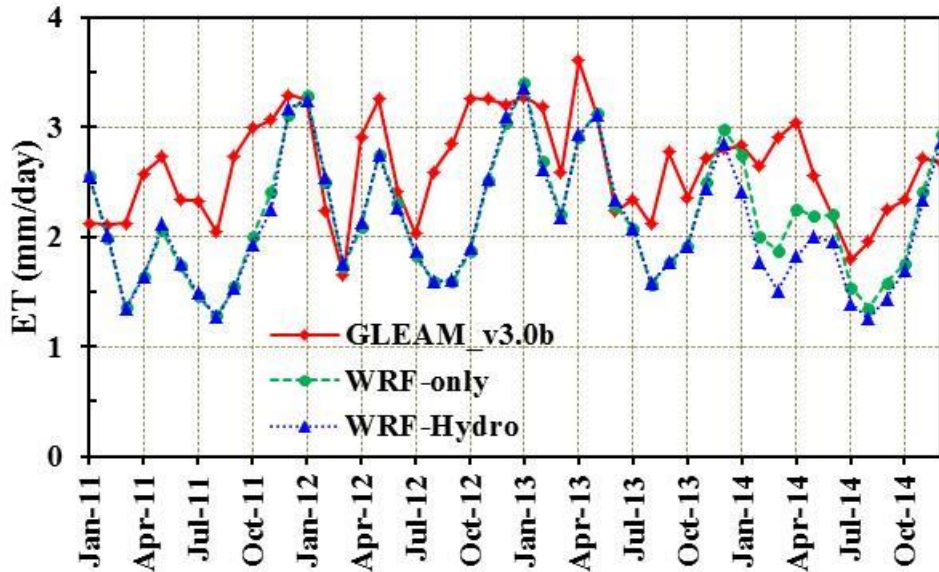


Figure V-4: Monthly and interannual variation of ET as derived from GLEAM_v3.0b dataset and simulated in WRF-only and coupled WRF-Hydro over MSS and surrounding for 2011-2014

V.3 Verification of change in terrestrial water storage dS/dt

The adapted observations of dS/dt are derived based on the months with available discharge R from the Tana Rukanga's RGS 4BE10. P and ET are obtained from CHIRPS and GLEAM_v3.0b datasets respectively. Figure V-5 shows the monthly series of dS/dt as observed and simulated.

Both WRF-only and coupled WRF-Hydro capture well the seasonal and interannual evolution of the adapted observations of dS/dt . The simulated series are strongly correlated to the observed series, $r(44) = 0.73$, $p < 0.001$. The contribution of this good relationship comes more from the MAM season than the OND season. This is because during the latter season, there are more differences in magnitudes between simulated and observed dS/dt . During OND, the two models overestimate the peak season consistent with that for precipitation. This trend results in differences in the 4-year means i.e., $dS/dt_{\text{adapted observation}} = 0.16$ mm/day, $dS/dt_{\text{WRF-only}} = 0.80$ mm/day and $dS/dt_{\text{coupled WRF-Hydro}} = 0.76$ mm/day. These differences are large and expected especially as P , ET , and R vary in horizontal resolution and come from different sources.

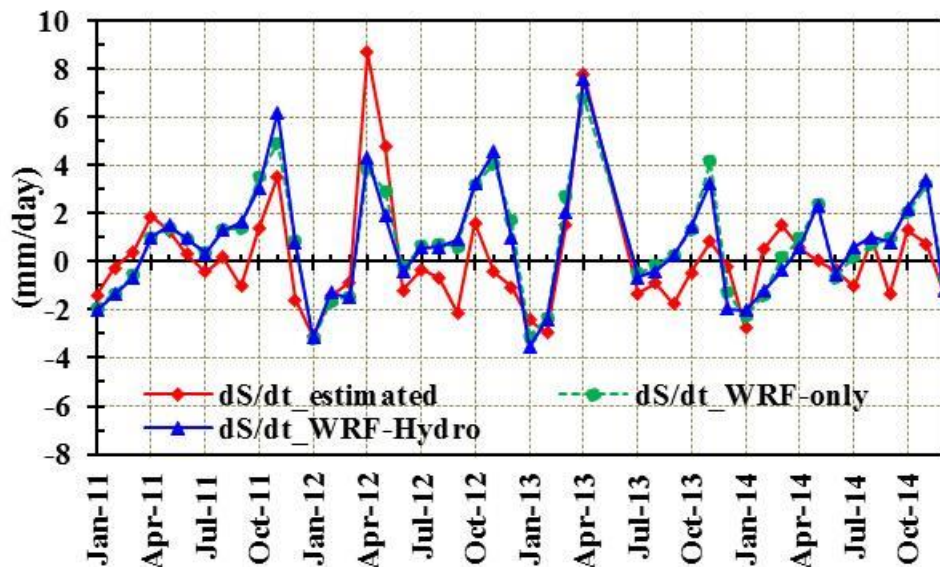


Figure V-5: Monthly and interannual variation of "adapted observations shown in red" and simulated (WRF-only shown in green; coupled WRF-Hydro shown in blue) dS/dt over MSS during 2011 to 2014

V.4 Interannual variability of TWB components

In this section, inter-model comparison between WRF-only and coupled WRF-Hydro is analyzed and presented. Figure V-6 shows the seasonal and interannual variability of the monthly time series of the TWB components as simulated in the two models. An explanation of the characteristics of each variable is provided below.

Precipitation P

The monthly evolution and interannual variability of P as simulated in both WRF-only and coupled WRF-Hydro exhibit striking similarity. Detailed discussion on the characteristics of P was provided in Section IV.2. During the 4-year period (2011-2014), WRF-only yields on average 3.7 mm/day while coupled WRF-Hydro yields 3.6 mm/day. The lowest amounts and corresponding highest deviation from the mean for the four years occurs during the months of January-February.

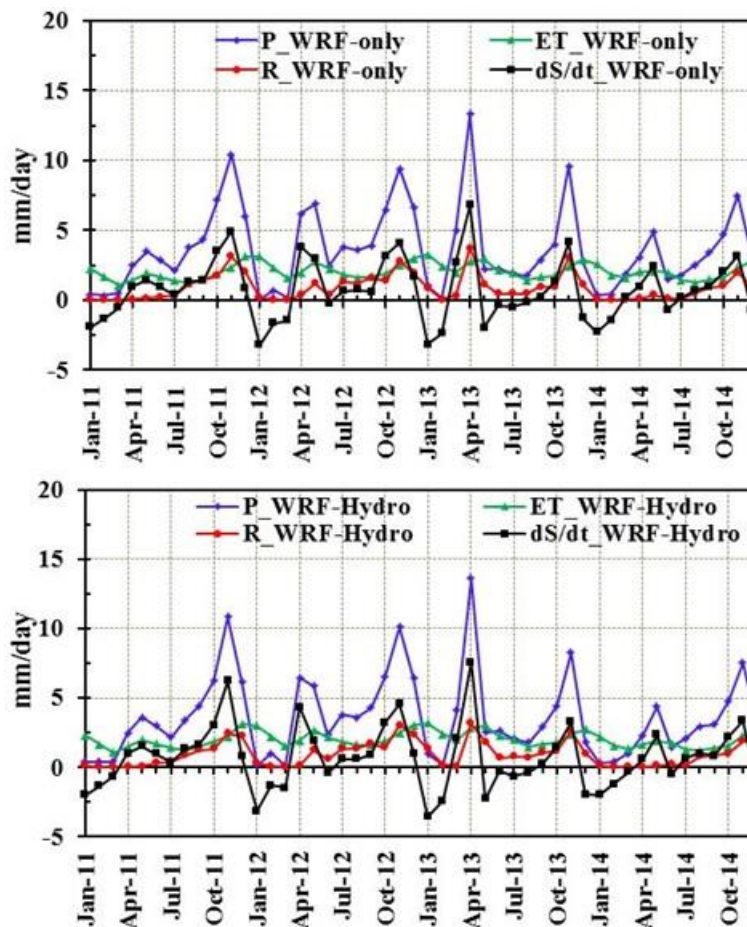


Figure V-6: Monthly TWB components as simulated in WRF-only (top) and coupled WRF-Hydro (bottom), spatially averaged over MSS and its surrounding for the period 2011-2014

Discharge *R*

Like *P*, a detailed discussion of *R* was provided in Section IV.3. Simulated discharge in coupled WRF-Hydro and total runoff from WRF-only show similar seasonality and interannual variability. This is further augmented by the illustration shown in Figure V-7. Here, both models capture the magnitude and interannual variability of the observed discharge. The MAM season is seen to exhibit the highest variability compared to OND season and annual variability.

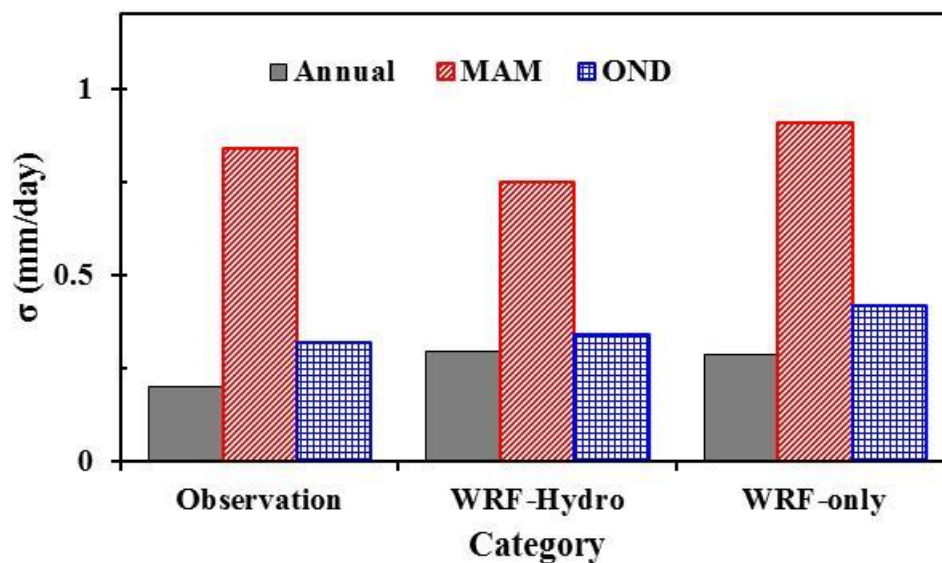


Figure V-7: Standard deviation of mean annual, seasonal (MAM, OND) discharge averaged during the period 2011-2014

Both WRF-only and the coupled WRF-Hydro indicate April as the peak month for the AMJ season while they indicate November as the peak month for the OND season consistent with observations. The 4-year (2011-2014) average discharge is 0.90 mm/day for WRF only, while it is 0.93 mm/day for the coupled WRF-Hydro. The observed discharge during the corresponding period is on average 0.95 mm/day. There is thus a close correspondence between simulated and observed discharge. This is seen in WRF-only and the coupled WRF-Hydro compared to observations having a strong significant relationship, $r(44) = 0.68$ and $r(44) = 0.62$, $p < 0.001$ respectively.

Evapotranspiration *ET*

The monthly and interannual variation of *ET* as simulated by WRF-only and coupled WRF-Hydro is explained in Section V.2.

Change in terrestrial water storage dS/dt

The monthly and interannual evolution of dS/dt exhibit seasonality with peak values in the months of April and November. The 4-year mean value of dS/dt derived from WRF-only is 0.72 mm/day compared to that from coupled WRF-Hydro of 0.68 mm/day. The characteristics based on the two models is similar and consistent to that presented in Section V.3 over a smaller area i.e., the MSS. On monthly scale, dS/dt component assumes both negative values and positive values. The negative or low values are domi-

nant during the months of January- February and June. Both models exhibit similar interannual variability.

V.4.1 Relationship between WRF-only and coupled WRF-Hydro components

The monthly differences between the two models simulated TWB components are shown in Figure V-8.

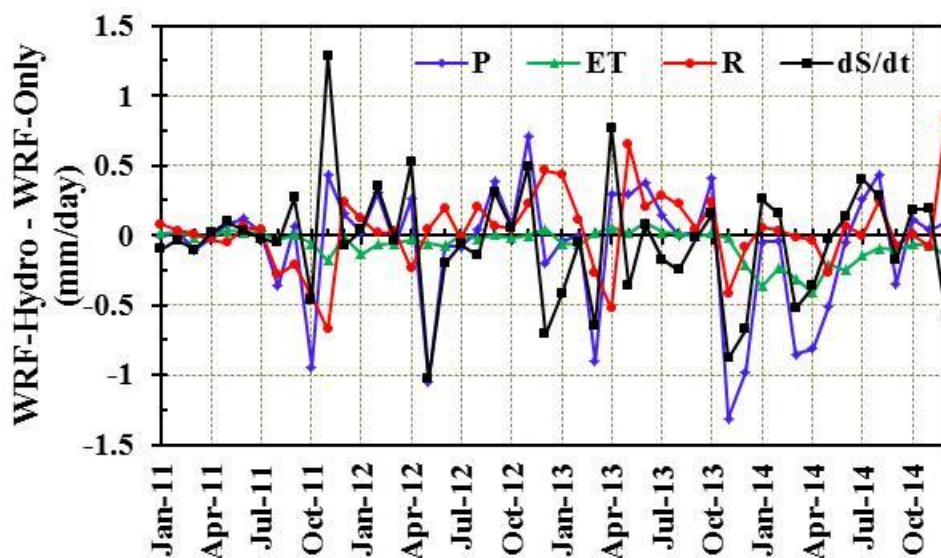


Figure V-8: Monthly differences (coupled WRF-Hydro minus WRF-only) of TWB components (in mm/day) for the period 2011-2014

The magnitudes of the average differences from the time series shown, for all TWB components are very small (between 0.03 mm/day and 0.08 mm/day). Precipitation shows the highest magnitude while discharge shows the least. On average, it is only in the simulation of discharge that coupled WRF-Hydro yields slightly better than the WRF-only. Though over the years there is an interchangeable behavior in magnitudes.

The evolution of monthly differences in dS/dt and P , in both models show similar patterns with higher differences in the peak months of MAM and OND seasons. P and dS/dt in the individual models exhibit the highest correlations ($r > 0.91$, $p < 0.001$). On average the differences between all TWB components are little and constant during the months of June and October. In the case of dS/dt and R , the sign of the differences between WRF-only and WRF-Hydro alternates, i.e. increased (reduced) runoff leads to

lowering (increasing) of the amount of soil moisture. This is common during the peak months of the rainy seasons of MAM and OND. The relationship between these two components in both WRF-only and coupled WRF-Hydro show a positive correlation which is however more stronger in WRF-only (i.e., $r(46) = 0.70$, $p < 0.001$ against $r(46) = 0.53$, $p < 0.001$). Further results shows that there is very low and insignificant relationship between ET and dS/dt in both models.

The difference between P and ET i.e., $P - ET$ for the two models yields similar values. On average for the four year period considered, these differences are 1.61 mm/day. This is further discussed in Section V.4.2. The relationship between P and ET , in terms of evolution and variability, shows a low positive insignificant relationship in both models ($r(46) = 0.25$, $p = 0.09$ for WRF-only and $r(46) = 0.29$, $p = 0.05$ for the coupled WRF-Hydro). In the case of $P - R$, WRF-only has a higher difference of 2.78 mm/day compared to that for the coupled WRF-Hydro of 2.67 mm/day. The relationship between P and R is strong in both models with high correlation coefficients ($r > 0.8$, $p < 0.001$). The difference between WRF-only and the coupled WRF-Hydro is seen in the relationship between the simulated ET and R . The two components are reasonably correlated in coupled WRF-Hydro with a correlation coefficient of $r(46) = 0.51$, $p < 0.001$, while weakly correlated in the WRF-only with a correlation coefficient of $r(46) = 0.36$, $p = 0.01$.

V.4.2 Annual mean of terrestrial water balance components

Table V-1 shows the 4-year annual mean of TWB components (in mm/year) over the MSS and its surrounding. P has the greatest contribution to the TWB, while ET on average, for the two models, is approximately 55 % of P . The R values are only 24 - 26 % of those of P .

Table V-1: The 4-year mean of TWB components: P , ET , R and dS/dt for the MSS and its surrounding for the period 2011 to 2014

TWB component (mm/year)	Experiment	
	WRF-only	WRF-Hydro
P	1346	1317
ET	753	729
R	329	341
dS/dt	264	247

The order of magnitude of the annual mean of the TWB components show no changes compared to that in monthly averages. In individual years, however, the highest P is that recorded in 2012, which is also similar to ET . The highest R in the two models was recorded in 2013, while dS/dt has the maximum value during 2011. This means that P , ET and R exhibit an increasing trend since 2011 through 2012 before falling towards to low values in the year 2013 and 2014. This by extension is seen in the annual mean differences in $P - ET$ for both WRF-only and the coupled WRF-Hydro. The aforementioned details are illustrated in Figure V-9. Here it is displayed the magnitude of the mean annual of the TWB components for individual years specifically for the MSS (and the corresponding observations). Higher differences between observed and simulated components by both models are registered in P and ET , while lower differences are seen in R .

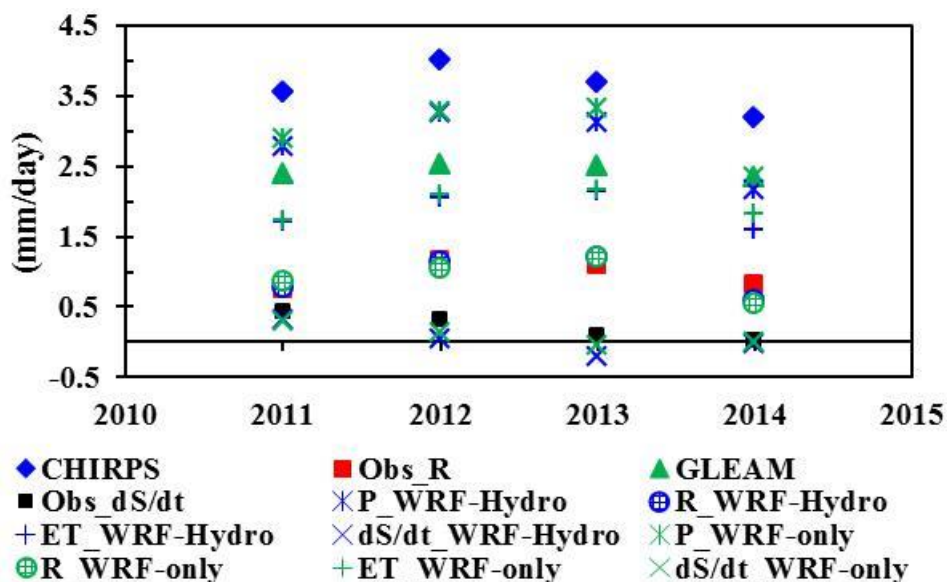


Figure V-9: Mean annual TWB components as observed and simulated for MSS for the period 2011-2014

V.5 Summary and discussion

The TWB components of precipitation P , evapotranspiration ET , streamflow R and change in terrestrial water storage dS/dt are analyzed and presented in both observational and simulation modes. The simulated ET in WRF-only and the coupled WRF-Hydro capture reasonably the observed ET patterns, seasonal peaks and interannual evolution exhibited in GLEAM datasets. The three GLEAM datasets i.e., GLEAM_v3.0a, GLEAM_v3.0b and GLEAM_v3.0c are applied for the first time in the MSS and its surroundings or in general East Africa and display similar patterns. In reference to the MSS and its surroundings, the Northwest of the upper TRB is characterized with slightly higher ET than towards its Eastern parts. The high ET values in parts of TRB can be attributed to the underlying land use of evergreen forest and savanna. Such areas are also characterized by abundant precipitation. On the other hand, higher temperatures over the eastern sections of TRB are not associated with higher evaporation rates. However, what is relevant in this context is related to the expected higher precipitation over equatorial areas as well as maximum evaporation rates (Peixoto and Oort, 1992) in which case the opposite scenario to these applies.

WRF-only and coupled WRF-Hydro model computed dS/dt over the MSS show a reasonable positive correlation compared to the adapted observations of dS/dt computed from observational datasets. This means, with available gridded datasets of P and ET and well archived discharge R data, it is possible to determine this important component of the water cycle that is critical in closing the water cycle and significant in the water resources, climate, agriculture and ecosystem (Yeh and Famiglietti, 2008).

The seasonality and interannual variability of the TWB components as simulated in both WRF-only and coupled WRF-Hydro shows similarity. The peak season for P , R and dS/dt occur during April and November that corresponds to the two rainy seasons of MAM and OND. ET shows a weaker peak season a month later in both seasons. Further results show that in both the two models, the MAM season displayed a higher interannual variability compared to the OND season or annually. A notable example of this variability is in discharge.

The magnitudes of the differences between the WRF-only and coupled WRF-Hydro are small for all the components. The WRF-only model simulated higher values of all the components with exception of discharge.

The relationship between the TWB components in individual models shows significantly fair to strong positive correlations, except between ET and dS/dt and also between ET and P . The very high correlations between dS/dt and P on one hand and R and dS/dt on the other hand shows a likelihood of a positive feedback soil moisture-precipitation (e.g., Kunstmann and Jung 2007). The weaker relationship corresponding to ET shows that for instance it has most likely a negative feedback on P in the subcatchment and its surrounding. The difference between WRF-only and coupled WRF-Hydro in the relationship between ET and R show stronger correlation in the latter model than the former.

The order of mean annual values of simulated TWB varies like that of observed components both annually and in the 4-year mean with very little variation in ET . P and R mean annual increases from 2011 and reach a maximum in 2012 and decreases to a minimum in 2014. However, for dS/dt , the mean annual values decreases from 2011 to a minimum in 2014. Generally, in both WRF-only and the coupled WRF-Hydro, P has the highest variation followed by dS/dt , then R and lastly ET . This variation is more in coupled WRF-Hydro in all the four TWB components as seen both in standard deviation for the four years and in the interannual range.

VI Atmospheric Water Balance for Mathioya-Sagana Subcatchment

VI.1 Introduction

The basic theory of the atmospheric water balance (AWB) was presented in Section II.7. As a review of the theory, the AWB variables are the atmospheric water vapor convergence C , evaporation ET , precipitation P and the change in atmospheric water storage dW/dt . As in Chapter V, for TWB components, all AWB components are spatially averaged over the Mathioya-Sagana subcatchment (MSS) and its surroundings. The simulated components from the WRF-only and the coupled WRF-Hydro models for the 4-year (2011-2014) climatology are compared in terms of seasonal, annual and interannual variability together with the differences in inter-model simulations. This chapter presents work that has been published in the Journal of Theoretical and Applied Climatology (Kerandi *et al.*, 2017). Section VI.1.1 examines the seasonal and interannual variability of AWB components before exploring the inter-model comparisons of these components in terms of their mean annual cycle and annual averages in Section VI.2. The relationship between C and streamflow R is examined in Section VI.3 which leads to further description of estimation of the change in terrestrial water storage dS/dt .

VI.1.1 Seasonal and interannual variability of AWB components

Figure VI-1 displays seasonal and interannual variability of the computed monthly AWB components as simulated in WRF-only and coupled WRF-Hydro.

Precipitation P and Evapotranspiration ET

The monthly and interannual variation of P and ET are similar to that explained in Chapter V for the case of TWB components. P is considered a loss from the atmosphere and a gain for the terrestrial surface, while ET is obviously a gain for the atmosphere and a loss from the surface. As seen in Chapter V, ET reaches its peak in May for the MAM season, one month after that of P .

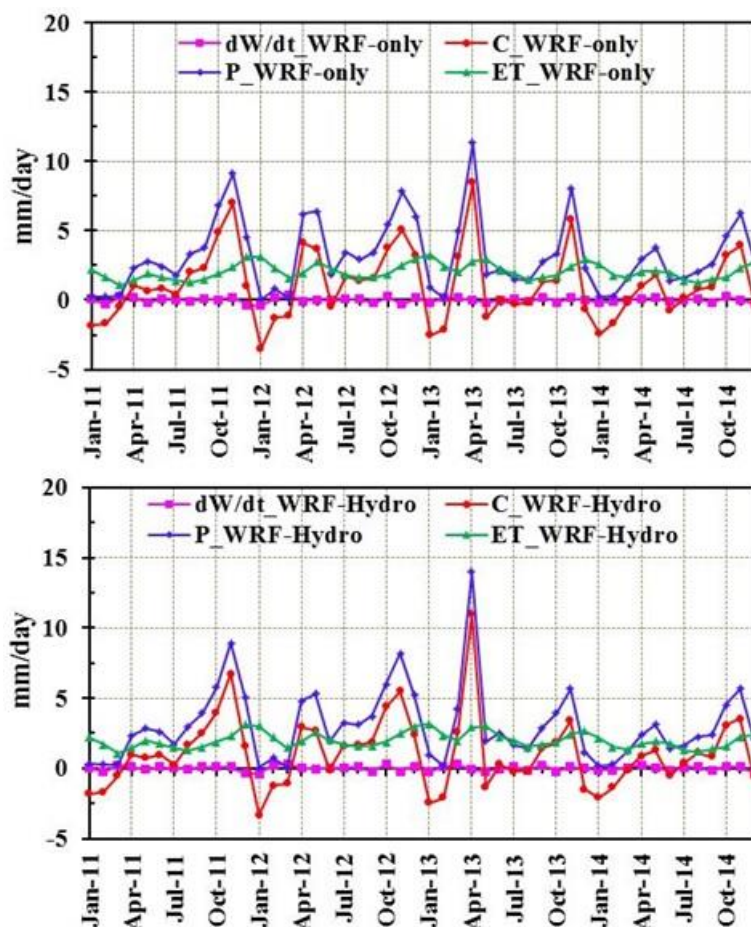


Figure VI-1: Monthly AWB components as simulated in WRF-only (top) and coupled WRF-Hydro (bottom) for the MSS and surrounding during 2011-2014: precipitation P , blue line; evaporation ET , green line; atmospheric water vapor convergence C , red line; change in atmospheric water storage dW/dt , magenta line

Atmospheric moisture convergence C

The atmospheric moisture convergence C monthly and interannual variation is typical of that of P . C reaches its peak in April and November which is the peak months of the two rainy seasons (i.e., MAM and OND) in this region. The lowest values are during the months of January. C can assume both negative and positive values which mean that its long term magnitude can reduce owing to the cancelling out of the values.

Atmospheric water storage dW/dt

The atmospheric water storage dW/dt hardly shows any monthly or interannual variation in both WRF-only and coupled WRF-Hydro. It is very small compared to the other terms and tends to zero, as is expected for a regional water balance.

VI.2 Relationship between WRF-only and coupled WRF-Hydro components

The monthly differences between coupled WRF-hydro and WRF-only AWB components are summarized and displayed in Figure VI-2. Table VI-1 summarizes the long term variation of the same.

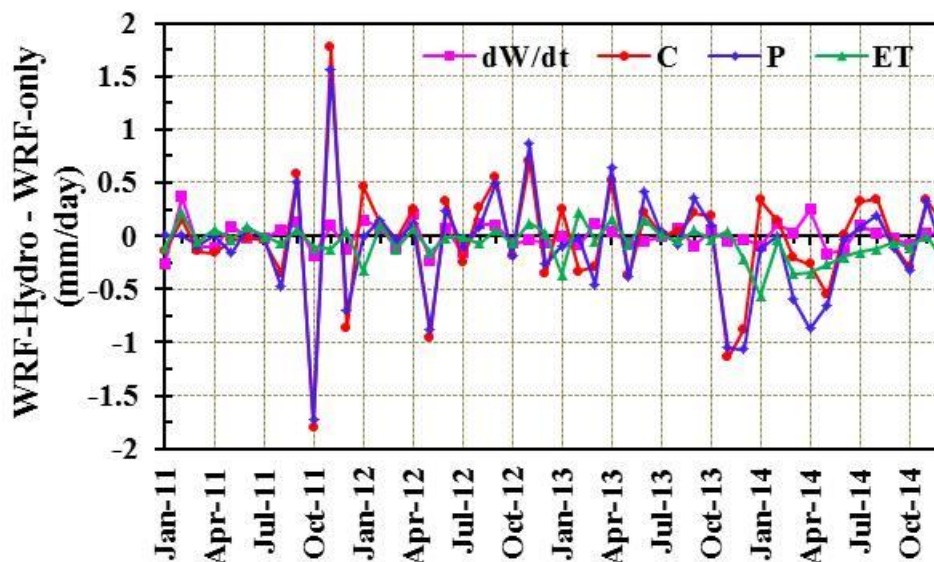


Figure VI-2: Monthly differences (coupled WRF-Hydro minus WRF-only) of AWB components shown in Figure VI-1 for the period 2011 to 2014

Table VI-1: Annual differences between coupled WRF-Hydro and WRF-only AWB components shown in Figure VI-2. All values are in mm/day

AWB component	2011	2012	2013	2014	4-yr mean
<i>dW/dt</i>	-0.01	0.00	-0.01	0.01	0.00
<i>C</i>	-0.09	0.08	-0.13	0.02	-0.03
<i>P</i>	-0.08	0.04	-0.13	-0.19	-0.09
<i>ET</i>	0.00	-0.03	-0.01	-0.20	-0.06

The magnitude of the differences between WRF-only and coupled WRF-Hydro AWB components are more in 2013 and least in 2011 and 2012. It is noticed that the differences in *P* and *C* display a similar pattern over the years. This implies that the differences in *P* originate from differences in *C*. This is associated with the impact of moisture vapor influx into the domain whose average magnitude for the 4-year period is greater than that of vapor outflow in both models. However, in individual years the models display larger differences, especially during the years when the coupled WRF-Hydro yields more *C* than WRF-only model. The differences in *ET* and *dW/dt* are comparatively smaller with however the year 2014 having the highest difference for the case of *ET* (0.20 mm/day).

The relationship between the AWB components as simulated in the individual models show diverse correlations. There is very high positive correlation between *C* and *P*, $r(46) > 0.96$, $p < 0.001$ in both WRF-only and the coupled WRF-Hydro. However, there is a very small insignificant relationship between *ET* and *C*. *ET* also exhibit a weak positive relationship compared to *dW/dt*, i.e., $r(46) = 0.35$, $p = 0.01$ for WRF-only and $r(46) = 0.39$, $p < 0.001$ for the coupled WRF-Hydro.

On monthly or longer periods, it is seen that $P - ET \approx C$ as $dW/dt \approx 0$. This means that the difference between *P* and *ET* is a good substitute for atmospheric moisture convergence.

VI.2.1 Mean annual cycle of AWB components

Figure VI-3 displays the 4-year mean annual cycle of the AWB components as simulated in WRF-only and the coupled WRF-Hydro. The seasonality of the four AWB variables is evident and is consistent with earlier discussion as highlighted in Section VI.1.1. The mean annual cycle of *C* shows that the MSS and its surrounding is characterized

by large water vapor convergence most of the year (roughly from March onwards) unlike periods of divergence (January to March). The former periods of convergence when $P > E$ dominate throughout the year unlike when $E > P$. It is an indication of the influence of the orographic effects of Mount Kenya and the Aberdares, which are responsible for the abundant precipitation in the region as seen in the previous chapters. Clearly, dW/dt is seen to remain about zero on average, consistent with expectations of a regional water balance. In the case of ET compared to C , ET remains greater than C from May until August (September) for WRF-only (coupled WRF-Hydro). These are months during which dry conditions prevail in the region and ET seems to be dominant.

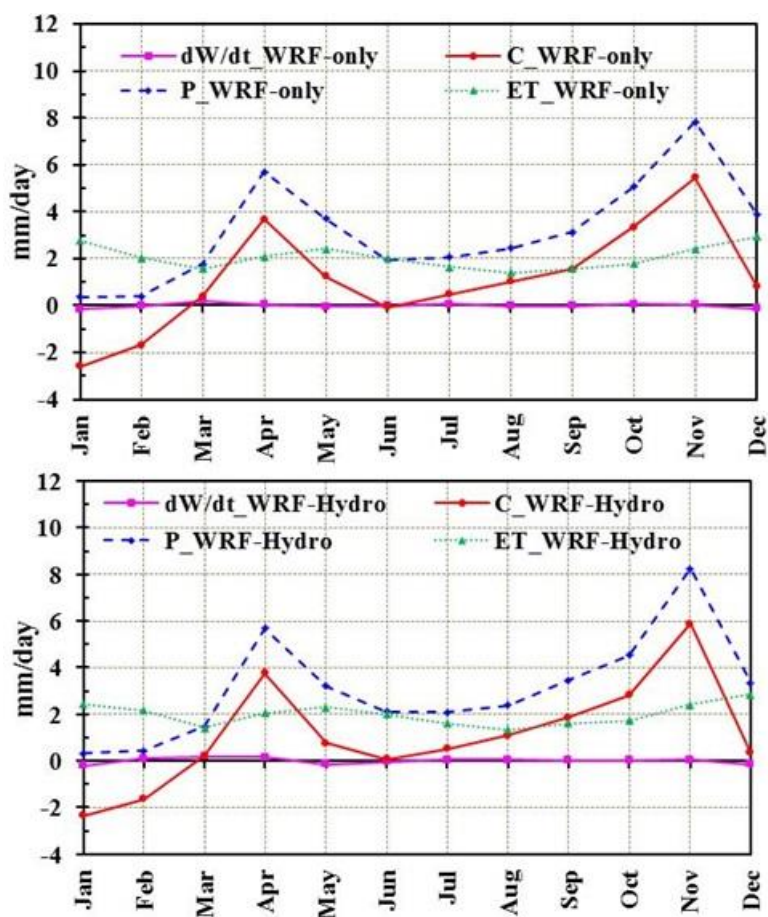


Figure VI-3: Mean annual cycle of AWB components averaged during 2011 to 2014 as simulated in (top) WRF-only and (bottom) coupled WRF-Hydro for the MSS and its surrounding

Table VI-2 shows the mean annual cycle of standard deviation of the AWB components averaged for the period of 2011 to 2014.

Atmospheric water balance for Mathioya-Sagana subcatchment

Table VI-2: Mean annual cycle of AWB components showing monthly standard deviation. Values in bold show the month (s) with highest variability for MAM and OND season

Experiment		Jan	Feb	Mar	Apr	May	Jun
<i>dW/dt</i>	WRF-only	0.19	0.23	0.13	0.13	0.16	0.09
	WRF-Hydro	0.03	0.11	0.10	0.16	0.10	0.16
C	WRF-only	0.67	0.33	1.92	3.52	2.05	0.69
	WRF-Hydro	0.46	0.54	1.82	3.88	1.79	0.64
P	WRF-only	0.36	0.30	2.26	4.12	1.95	0.45
	WRF-Hydro	0.33	0.38	2.1	4.62	1.69	0.57
ET	WRF-only	0.50	0.37	0.38	0.56	0.49	0.26
	WRF-Hydro	0.47	0.42	0.39	0.65	0.51	0.29
<hr/>							
		Jul	Aug	Sep	Oct	Nov	Dec
<i>dW/dt</i>	WRF-only	0.04	0.1	0.18	0.21	0.23	0.25
	WRF-Hydro	0.09	0.11	0.17	0.20	0.27	0.25
C	WRF-only	0.85	0.92	0.58	1.46	1.28	1.76
	WRF-Hydro	0.71	0.84	0.86	0.85	2.03	1.84
P	WRF-only	0.92	0.87	0.54	1.44	1.18	1.72
	WRF-Hydro	0.86	0.76	0.80	0.80	1.87	1.93
ET	WRF-only	0.27	0.18	0.09	0.13	0.07	0.15
	WRF-Hydro	0.32	0.19	0.13	0.14	0.16	0.29

The year-to-year variability of dW/dt is highest during the OND season in the months of November and December for WRF-only and coupled WRF-Hydro respectively. *C* and *P* show correspondingly high year-to-year variability during the same months of April and November (December). The variation in April, is however, comparatively higher.

VI.2.2 Annual averages of the AWB components

The annual averages of the AWB are summarized in Table VI-3. The averages are usually nearly zero for the atmospheric water tendency term (dW/dt), consistent with earlier discussions. The annual averages of vapor influx into the domain are consistently more than the outflow out of the domain. The results in this section compliment those in Section VI.1.1. The mean values for ET over the years and the 4-year mean for both WRF-only and coupled WRF-Hydro are closely related in magnitude. The values increase from 1.8 mm/day in 2011 to a maximum of 2.3 mm/day in 2013. P and C have their maximum annual averages in 2012. The 4-year mean of C in both WRF-only and coupled WRF-Hydro is about a half that of P which is the leading term in terms of magnitude. As seen earlier, C events follow closely those of P and that they have a very strong linear relationship.

Table VI-3: Annual averages of the AWB components as simulated in WRF-only and coupled WRF-Hydro during 2011 to 2014 for Mathioya-Sagana subcatchment

	Experiment	2011	2012	2013	2014	4-yr mean
dW/dt	WRF-only	0.00	0.01	0.00	-0.01	0.00
	WRF-Hydro	0.00	0.02	0.00	-0.01	0.00
IN	WRF-only	118.50	118.80	119.98	122.18	119.86
	WRF-Hydro	117.99	118.90	117.73	120.87	118.87
OUT	WRF-only	117.14	117.28	118.87	121.60	118.72
	WRF-Hydro	116.72	117.30	116.75	120.27	117.76
C	WRF-only	1.35	1.52	1.11	0.58	1.14
	WRF-Hydro	1.27	1.59	0.98	0.60	1.11
P	WRF-only	3.14	3.71	3.41	2.51	3.19
	WRF-Hydro	3.06	3.75	3.27	2.32	3.10
ET	WRF-only	1.79	2.21	2.31	1.92	2.06
	WRF-Hydro	1.79	2.17	2.30	1.72	1.99

VI.3 Relationship between mean vapor convergence and streamflow

In practice, it is expected that the mean vapor convergence C should be equal to the average streamflow R over a long time and Equation II-6 holds true. This however is depended on many factors that may include either the time period under investigation (e.g., Yeh and Famiglietti, 2008) or the geographical location of the region under study (e.g., Severatne, 2003).

Figure VI-4 shows the monthly and interannual evolution of C and R as simulated by WRF-only and coupled WRF-Hydro. The observed discharge during the same period is included for comparison.

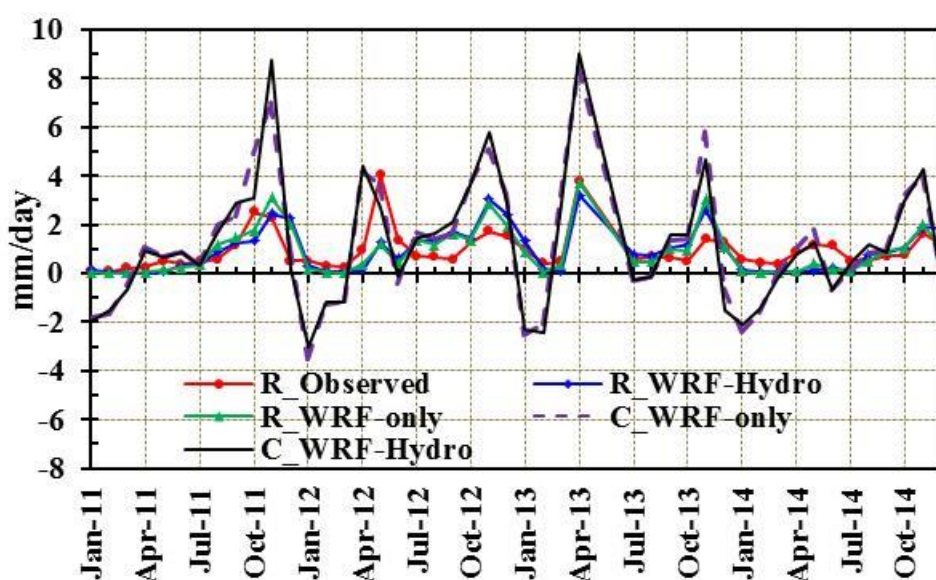


Figure VI-4: Monthly timeseries of discharge and atmospheric convergence as simulated by WRF-only and coupled WRF-Hydro during 2011 to 2014 for Mathioya-Sagana subcatchment.

Observed discharge for Mathioya-Sagana basin is also included (red line)

The monthly and interannual variability of C and R follows a similar pattern with peak values during April and November. The lowest values of C occur during the month of January while that of both observed and simulated discharge occur a month after i.e., February and March. The time series are in agreement in temporal evolution with correlation coefficients of more than 0.7.

Table VI-4 shows the 4-year mean of C and R . The mean values for the two models are very close. There exist imbalances between C and R that differ significantly between the two models.

Table VI-4: The 4-year mean of the atmospheric vapor convergence, C and discharge, R and the difference between the two

	WRF- only	WRF- Hydro	Observation
R (mm/day)	0.90	0.92	0.95
C (mm/day)	1.22	1.19	-
Imbalance $= (C/R) - 1$	36 %	29 %	28 % (25 %)

The bias or difference between C and R in the coupled WRF-Hydro simulated variables is lower than that in WRF-only. This is further confirmed when using observed discharge at the mouth of the Mathioya-Sagana subcatchment, which is independent of the two simulations compared to their simulated C . The low imbalance in coupled WRF-Hydro can be associated with its integrated processes of the subsurface overland, channel and bucket model which are absent in the WRF-only model. Our results are comparable with those performed over larger basins in other parts of the world (e.g., Yeh & Famiglietti, 2008).

However, the assumption that both dW/dt and dS/dt becomes negligible at longer periods (annually or longer) doesn't apply for dS/dt in this study as seen in Chapter V. This is consistent with the findings of Oki *et al.* (1995) that dS/dt doesn't tend to zero even for a period of 4 years due to interannual variation of soil moisture storage. Thus Equation II-6 doesn't hold true at this scale. Instead Equation II-5 can be written as

$$C = R + \frac{dS}{dt} \tag{VI-1}$$

since only dW/dt reduces to zero at monthly scale or longer. This could be an appropriate relationship that links the TWB and AWB at the scale of MSS and its surrounding. The results of Equation VI-1 are shown in Figure VI-5.

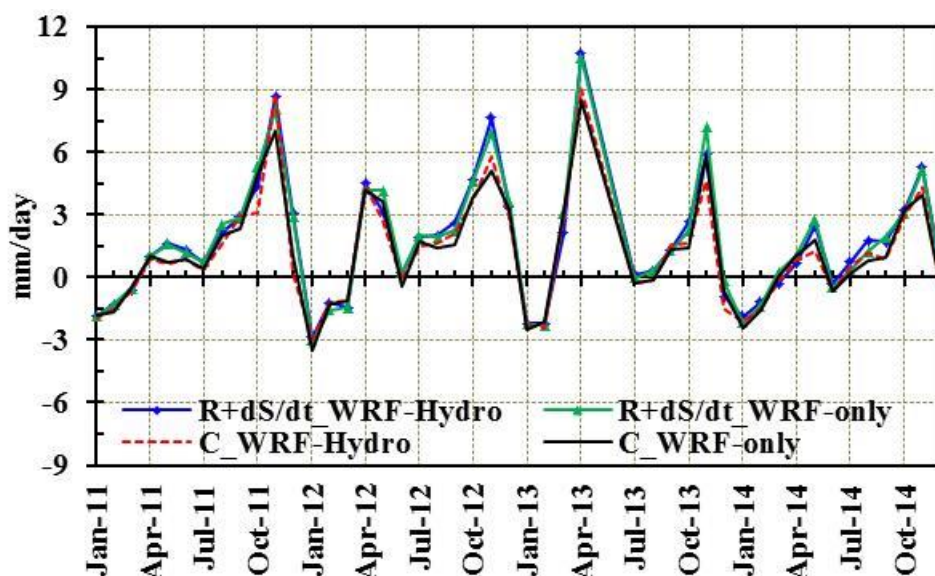


Figure VI-5: Monthly time series of simulated R and dS/dt and corresponding C over MSS for the period 2011-2014

There is a very good agreement in the temporal evolution of $R + dS/dt$ and C in both WRF-only and the coupled WRF-Hydro. There is also a very strong positive relationship between $R + dS/dt$ and C , $r(46) > 0.97$, $p < 0.001$. The 4-year mean are closely related with only a difference of approximately 29 %.

VI.4 Land-atmospheric interactions within the Mathioya-Sagana subcatchment

This section is based on Equations II-7 and II-8 on the atmospheric bulky properties, i.e. the recycling ratio β and the precipitation efficiency χ . The two measures are used to analyze the land-atmospheric interactions and feedbacks between the land and atmosphere in the study area.

VI.4.1 Recycling ratio β

Figure VI-6 shows the monthly and interannual variation of the recycling ratio for the period 2011 to 2014 as simulated in the WRF-only and coupled WRF-Hydro. In general, the value of β is high whenever there are low moisture influx and high evapotranspiration. This is in agreement with findings of Asharaf *et al.* (2012). In particular, β is seen to vary from 0.01 to 0.04. High values of β occur during the months of January that exhibit largest amount of ET (dominant compared to P). In terms of the rainy sea-

sons i.e., MAM and OND, it is noticed that β remains below 0.02. The MAM and OND of 2013 registered the highest β which is associated with the end months in that season having had the highest amount of ET compared to other months in those seasons. This implies that precipitation originating from evapotranspiration in the MSS region, i.e., the study area, contributes little to the total precipitation in this region during the quadrennial. It is concluded that local precipitation in the study area does not depend significantly on the state of the land surface, and that potential land-precipitation feedback mechanisms have a reduced impact.

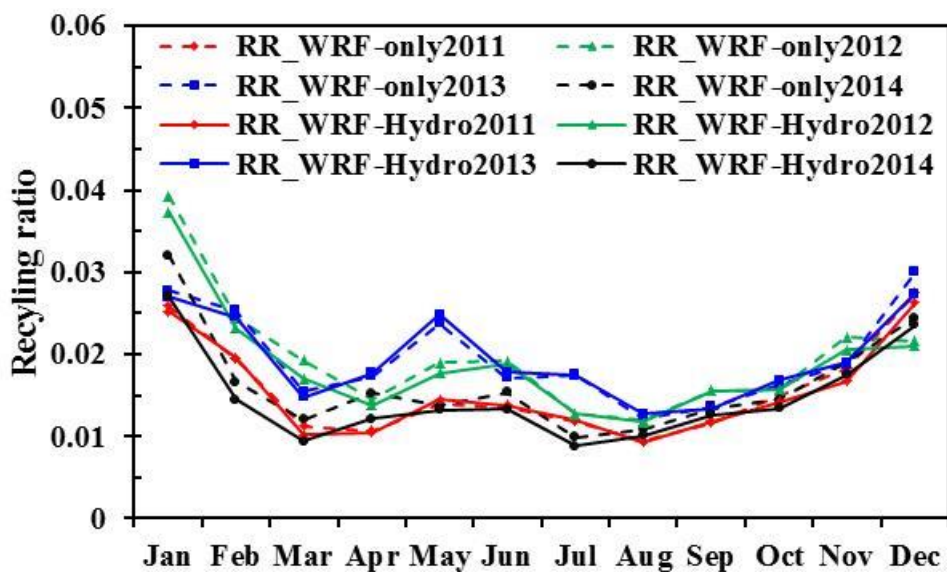


Figure VI-6: Monthly variation of the recycling ratio for the years 2011 to 2014 as simulated in WRF-only and coupled WRF-Hydro for the Mathioya Sagana subcatchment

VI.4.2 Precipitation efficiency χ

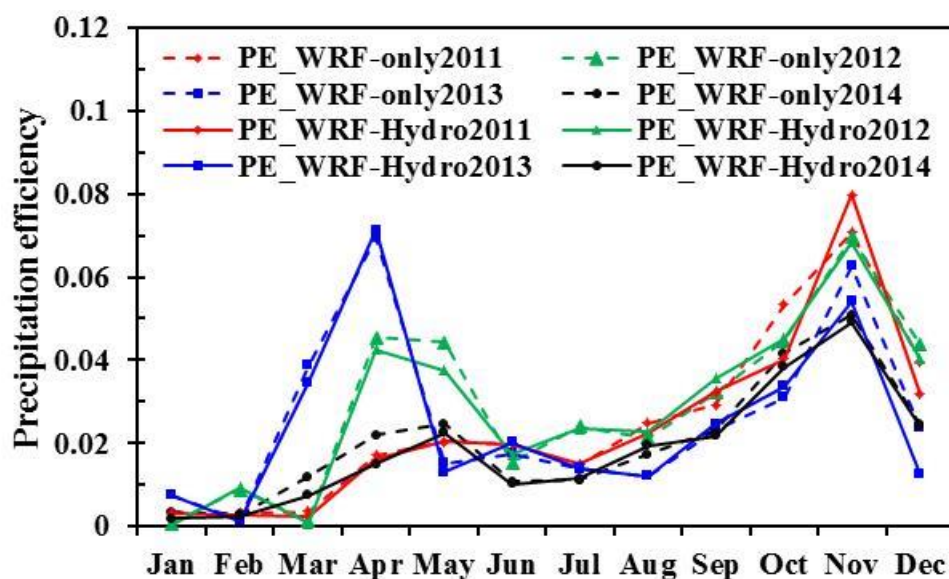


Figure VI-7: Monthly variation of precipitation efficiency for the years 2011 to 2014 for Mathioya-Sagana subcatchment as simulated in WRF-only and coupled WRF-Hydro

The monthly variation of the precipitation efficiency χ is displayed in Figure VI-7 for different years. Two distinct seasons similar to that of the rainy seasons i.e., MAM and OND in each of the years, are depicted. The values of χ for the two models are in the range of 0.0 and 0.07. These values, especially during the MAM season, differ significantly from one year to another. The reason behind this can be associated with the amount of precipitation during those seasons. The values of χ reach their peaks during the months of April (May) and November.

VI.4.3 Mean annual averages of β and χ

The mean averages of β and χ are summarized in Table VI-5 together with the computed 4-year average. The annual averages for the two models are nearly equal on average over the years. The magnitudes of the two are also more or less equal. The correlation coefficients between P and β is negative for both WRF-only and coupled WRF-Hydro i.e., -0.16 and -0.14 respectively while for the case of P and χ it is 0.98 for both models.

Table VI-5: Annual averages of the recycling ratio and the precipitation efficiency for Mathioya-Sagana subcatchment during 2011 to 2014

	2011	2012	2012	2014	4-Year mean
RR_WRF-only	0.02	0.02	0.02	0.02	0.02
RR_WRF-Hydro	0.02	0.02	0.02	0.01	0.02
PE_WRF-only	0.02	0.03	0.03	0.02	0.03
PE_WRF-Hydro	0.02	0.03	0.02	0.02	0.02

VI.5 Further estimation of terrestrial water storage dS/dt

In Chapter V, the terrestrial water storage dS/dt results are computed as a residual of P , ET and R . dS/dt is considered as a basic quantity of closing the water balance (Yeh and Famiglietti, 2008). To this effect, dS/dt is estimated as a residual of C , dW/dt from AWB components and R which is measured at the outlet of the basin (Oki *et al.*, 1995; Senevitne *et al.*, 2004; Yeh and Famiglietti, 2008). This is represented in Equation II-5, which can be rewritten to as

$$\frac{dS}{dt} = C - \frac{dW}{dt} - R. \quad \text{VI-2}$$

On the other hand, dS/dt is also defined and expressed in terms of its constituents, i.e. soil moisture, groundwater, land ice, surface and underground water and biomass water. Soil moisture is considered the major element in contributing to seasonal changes in terrestrial water storage in the tropics and midlatitudes (Senevitne *et al.*, 2004). In this thesis, only soil moisture and underground water model outputs are considered in estimating dS/dt . In this section, we demonstrate the relationship between these three approaches of estimating dS/dt is demonstrated. All three approaches give reasonable results for this estimation.

Figure VI-7 shows the monthly and interannual variation results of dS/dt obtained from the three methods explained above together with the adapted observed dS/dt . There is reasonable agreement between the observed and estimated dS/dt in the monthly evolution. In all approaches the capture of the seasonal peaks i.e., April for MAM and No-

vementer for OND is clearly depicted. In a clear relationship to the observed precipitation P , the MAM season of dS/dt is underestimated while that of OND season is overestimated.

There is similarity in WRF-only and coupled WRF-Hydro associated sources of the estimated dS/dt as shown in Figure VI-8, Figure VI-9, and Figure VI-10. These three figures are summarized as illustrated in Figure VI-11. The AWB plus measured discharge approach yields the smallest coefficient of determination while the case of estimating dS/dt from soil moisture and underground water with the coupled WRF-Hydro gives slightly better coefficient of determination.

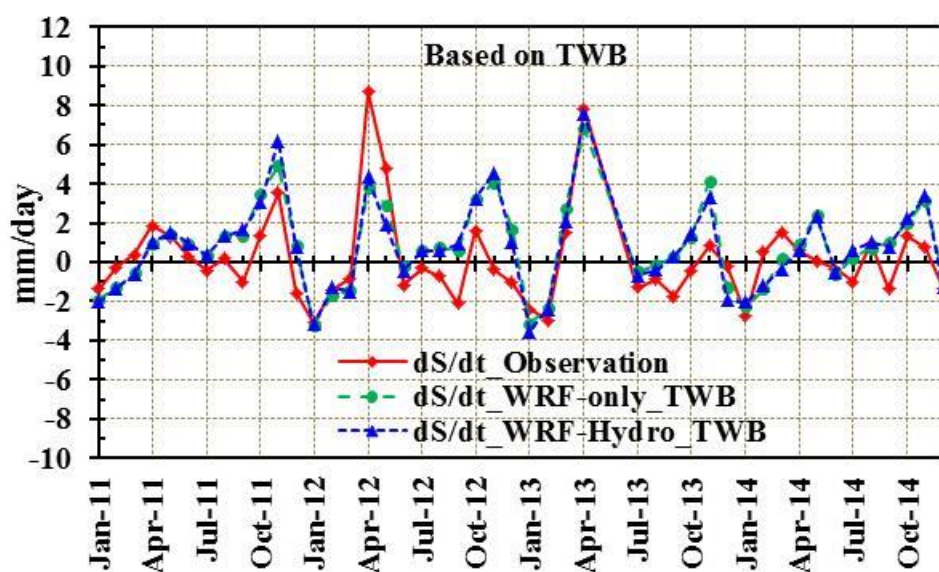


Figure VI-8: Monthly and interannual variation of estimated dS/dt (topleft) based on TWB components. The red line represent observations, blue line represent those from coupled WRF-Hydro simulations; green line are for WRF-only simulations

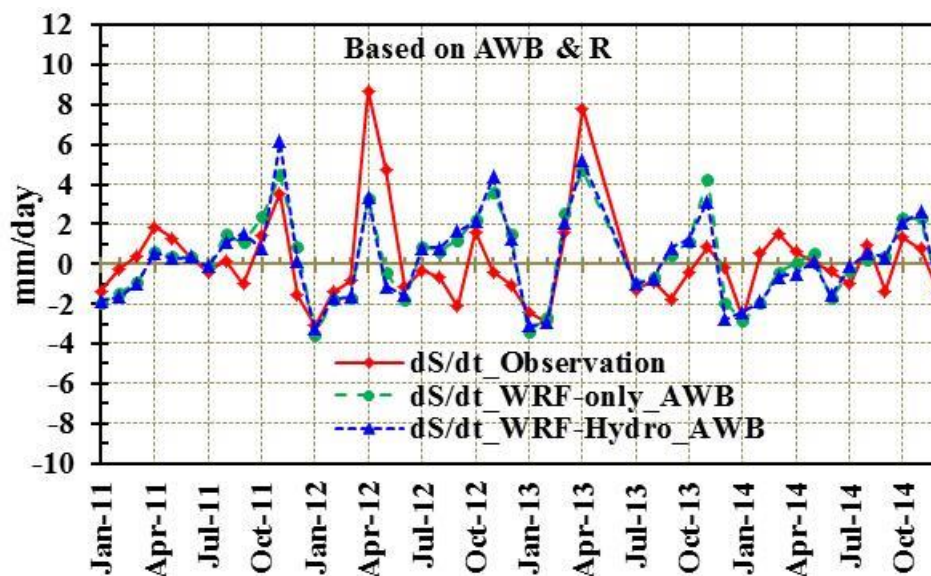


Figure VI-9: Monthly and interannual variation of estimated dS/dt based on AWB and measured discharge R . The red line represent observations, blue line represent those from coupled WRF-Hydro simulations; green line are for WRF-only simulations

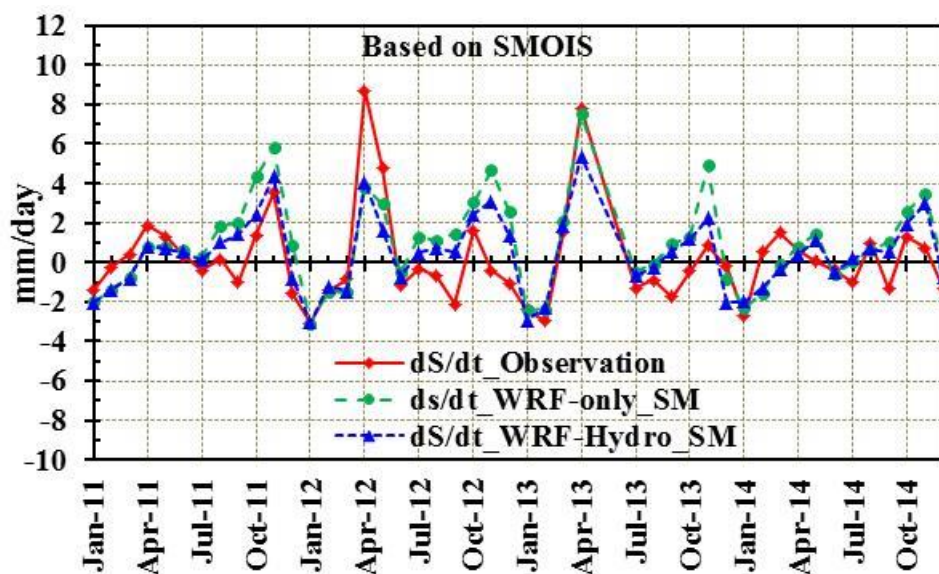


Figure VI-10: Monthly and interannual variation of estimated dS/dt based on simulated soil moisture and underground water. The red line represent observations, blue line represent those from coupled WRF-Hydro simulations; green line are for WRF-only simulations

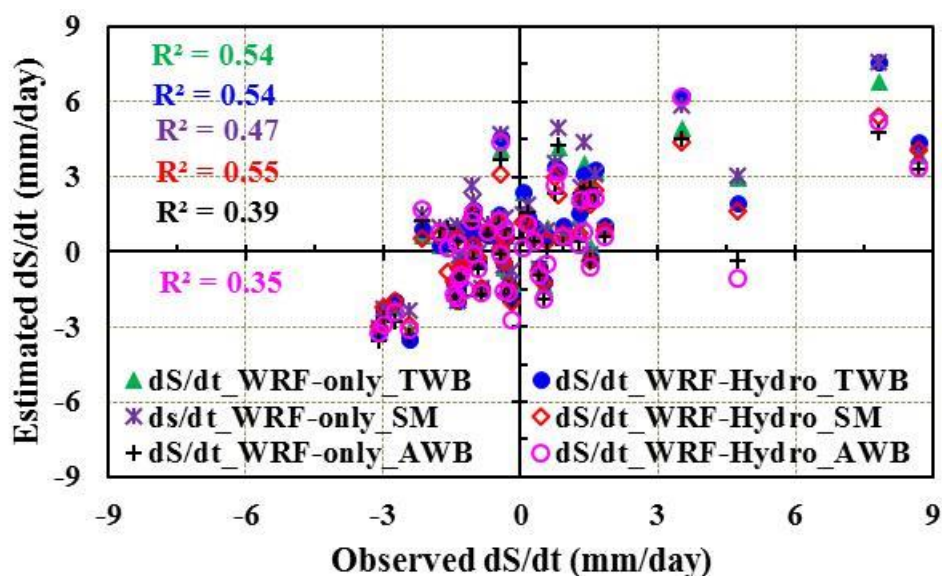


Figure VI-11: Scatter plot showing the monthly estimated dS/dt timeseries shown in Figure VI-8, Figure VI-9 and Figure VI-10. The different approaches of estimating dS/dt are compared to the “observed dS/dt”

Based on the individual years, it is seen that the mean annual averages of estimated dS/dt differ from one year to another. The individual annual averages and the 4-year mean don't tend towards zero. The smallest differences from observed dS/dt 4-year mean (i.e., 0.16 mm/ day) are between the AWB plus measured discharge with difference of the range between 0.07 and 0.10 mm/day. The highest difference is that between observed dS/dt and the soil moisture and underground method using the WRF-only model. This can be linked to slightly more simulated precipitation amounts of WRF-only compared to coupled WRF-Hydro.

VI.6 Summary and discussion

The analysis of the atmospheric water balance (AWB) components is presented in this chapter. Compared to TWB, the AWB components exhibit similar seasonal, annual and interannual variation in WRF-only and coupled WRF-Hydro. It is noted that the computation of the AWB components is rather complex to derive. For instance, the moisture vapor convergence C involves several other variables i.e., relative humidity, surface pressure, meridional and zonal wind velocities (Section II.7).

Evapotranspiration ET displays weaker variability throughout the period of study compared to C and precipitation P . The differences between WRF-only and coupled WRF-

Hydro AWB components are very small. The differences in P closely follow those in C . Further, P and C correlate strongly among the AWB components whether on monthly, seasonally or on average for the 4 years. This may suggest that C actually contributes more to P than either ET or any other external factors (Wei, Su and Yang, 2016).

As expected for AWB analysis, $dW/dt \approx 0$ and $C \approx P - ET$. The Mathioya-Sagana subcatchment (MSS) and its surrounding is characterized with more periods of atmospheric convergence, i.e. $P > ET$ than periods of divergence i.e., $P < ET$. Such high values of $P - ET$ are due to the role that C plays in increasing the atmospheric humidity hence an enhancement of moisture static energy and atmospheric instability factors which promote convection in the area leading to more precipitation (e.g., Wei *et al.*, 2016).

The imbalance between C and runoff R is quantified between the models with an assumption that both the terrestrial and atmospheric water tendencies terms i.e, dS/dt and dW/dt tend towards zero on average for the quadrennial. With such an assumption the coupled WRF-Hydro exhibit a lower imbalance compared to WRF-only. However, results in this thesis show that the 4-year average for dS/dt does not tend to zero. The component dS/dt is an important TWB component and for the closure of the water balance then must be combined with R at least for the scale utilized in this study. The relationship $dS/dt + R = C$ holds reasonably well in both WRF-only and the coupled WRF-Hydro in both evolution and magnitude.

The estimation of dS/dt is other than as a residual of P , ET and R is also obtained firstly as a sum of simulated soil moisture and underground runoff and secondly by the AWB method together with measured discharge at the Tana Rukanga's RGS 4BE10. The three independent approaches give results of dS/dt that compares reasonably well with each other.

The intensity of the water cycle has been quantified in terms of recycling ratio and precipitation efficiency. On the monthly scale, the magnitude of the recycling ratio was small, ranging from 0.0 to 0.04, while that of precipitation efficiency ranged between 0.0 and 0.07. This indicates that precipitation in this region during this period mainly originates from water vapor inflow at the lateral boundaries of the domain, so that potential land-precipitation feedback mechanisms have only small impacts in this region at this scale.

VII Conclusions and outlook

VII.1 Conclusions

The major conclusions from this PhD study are explained in terms of performance of the WRF regional circulation model (RCM), the application of the uncoupled and coupled WRF-Hydro model, and the characterization of regional atmospheric-terrestrial water balance.

VII.1.1 Performance of the WRF RCM

By taking advantage of the variety of parameterization options in the WRF model, the results from this study show that the choice of the land use data between USGS and MODIS that are available in WRF model together with increasing horizontal resolution from 50 km and 25 km may significantly impact simulated precipitation, but not so in temperature. On the other hand, the high resolution satellite precipitation data of TRMM and CHIRPS are a good proxy for the in-situ observations in the data-scarce region of Kenya and East Africa which are characterized by complex terrain.

VII.1.2 Application of WRF-Hydro

The uncoupled WRF-Hydro is applied for the first time over a subcatchment in the Tana River basin (TRB). The successful results of calibrations of the uncoupled WRF-Hydro gave motivation in also the application of the coupled WRF-Hydro. The WRF-Hydro modeling system is thus considered as a promising tool in predicting the hydro-meteorological situation of the basin.

This study for the first time, has characterized the atmospheric-terrestrial water balance components based on the coupled WRF-Hydro modeling system. The influence of the topography in the region of TRB is seen in most of the simulated water balance components. The coupled WRF-Hydro thus serves as a tool in quantifying the regional atmospheric-terrestrial water balance. The analysis of terrestrial and atmospheric water balance components shows that in comparison to the WRF stand-alone, coupled WRF-Hydro slightly reduces precipitation, evapotranspiration and the soil water storage, but increases runoff. The precipitation recycling and efficiency measures, which define the land-atmospheric interactions, are very close and small in both cases. This suggests that most of precipitation in the region comes from moisture advection from the outside

of our analysis domain, so that potential land-precipitation feedback mechanisms have a reduced impact in this region.

VII.2 Outlook

Taking the present configurations as a prerequisite, it is suggested that future work involving the WRF RCM should be based on more parameterization ensembles which will be ideal for long-term climate simulations in this region. Such studies will provide informed research findings for the proper management of the water and the agricultural sectors.

The results in this thesis show differences in the simulated discharge performance between coupled WRF-Hydro and uncoupled WRF-Hydro inconsistency with previous studies. It is suggested that in further applications of these modeling systems, more parameters should be calibrated like those associated with slope, soil and vegetation which are likely to impact simulated runoff and infiltration hence streamflow. It is proposed to consider a shorter period and carry both the stepwise manual calibration and an automated calibration, taking into consideration the computational costs.

Further work, with the application of the present approach of the water balance equations, the derived observations from stations, gridded satellite products and the estimated water balance variables will be critical in other basins in the region of East Africa. In future it is planned to extend the analysis to a new larger area, as it may be more appropriate to test the impact of local recycling at larger scales; hence improving the understanding of land-atmosphere feedback mechanisms. In the long run, such studies may lead to suggestions of better management practices of the scarce water resources over East Africa, and in particular Kenya.

Bibliography

Agwata, J. F. (2005) 'Water Resources Utilization , Conflicts and Interventions in the Tana Basin of Kenya', *Fwu*, 3(Topics of Integrated Watershed Management – Proceedings), pp. 13–23.

Anderson, J. R., Hardy, E. E., Roach, J. T., Witmer, R. E. and Peck, D. L. (1976) 'A Land Use And Land Cover Classification System For Use With Remote Sensor Data', *A revision of the land use classification system as presented in U.S. Geological Survey Circular 671*, 964, p. 41.

Anyah, R. O., Weaver, C. P., Miguez-Macho, G., Fan, Y. and Robock, A. (2008) 'Incorporating water table dynamics in climate modeling: 3. Simulated groundwater influence on coupled land-atmosphere variability', *Journal of Geophysical Research Atmospheres*, 113(7), pp. 1–15. doi: 10.1029/2007JD009087.

Anyah, R. and Semazzi, F. (2006) 'Climate variability over the Greater Horn of Africa based on NCAR AGCM ensemble', *Theoretical and Applied Climatology*, 86(1–4), pp. 39–62. doi: 10.1007/s00704-005-0203-7.

Anyah, R., Semazzz, F. and Xie, L. (2006) 'Simulated Physical Mechanisms Associated with Climate Variability over Lake Victoria Basin in East Africa', *Victoria*, pp. 3588–3609. doi: 10.1175/MWR3266.1.

Arnault, J., Wagner, S., Rummeler, T., Fersch, B., Bliefernicht, J., Andresen, S. and Kunstmann, H. (2016) 'Role of runoff-infiltration partitioning and resolved overland flow on land-atmosphere feedbacks: A case-study with the WRF-Hydro coupled modeling system for West Africa', *Journal of Hydrometeorology*, 17, pp. 1489-1516. doi: 10.1175/JHM-D-15-0089.1.

Asharaf, S., Dobler, A. and Ahrens, B. (2012) 'Soil Moisture–Precipitation Feedback Processes in the Indian Summer Monsoon Season', *Journal of Hydrometeorology*, 13(1989), pp. 1461–1474. doi: 10.1175/JHM-D-12-06.1.

Bronstert, A., Carrera, J., Kabat, P. and Lütkeemeier, S. (eds) (2005) *Coupled Models for the Hydrological Cycle*. Berlin: Springer-Verlag.

Chen, F. and Dudhia, J. (2001) 'Coupling an Advanced Land Surface–Hydrology Model with the Penn State–NCAR MM5 Modeling System. Part I: Model Implementation and

Sensitivity', *Monthly Weather Review*, 129(4), pp. 569–585. doi: 10.1175/1520-0493(2001)129<0569:CAALSH>2.0.CO;2.

Chou, M.-D. and Suarez, M. J. (1999) 'A solar radiation parameterization for atmospheric studies.', *NASA Technical Report 104606*, 15(June), p. 40.

Cook, K. H. and Vizy, E. K. (2012) 'Impact of climate change on mid-twenty-first century growing seasons in Africa', *Climate Dynamics*, 39(12), pp. 2937–2955. doi: 10.1007/s00382-012-1324-1.

Dee, D. P., Uppala, S. M., Simmons, A. J., Berrisford, P., Poli, P., Kobayashi, S., Andrae, U., Balmaseda, M. A., Balsamo, G., Bauer, P., Bechtold, P., Beljaars, A. C. M., van de Berg, L., Bidlot, J., Bormann, N., Delsol, C., Dragani, R., Fuentes, M., Geer, A. J., Haimberger, L., Healy, S. B., Hersbach, H., Hölm, E. V., Isaksen, L., Källberg, P., Köhler, M., Matricardi, M., McNally, A. P., Monge-Sanz, B. M., Morcrette, J. J., Park, B. K., Peubey, C., de Rosnay, P., Tavolato, C., Thepaut, J. N. and Vitart, F. (2011) 'The ERA-Interim reanalysis: Configuration and performance of the data assimilation system', *Quarterly Journal of the Royal Meteorological Society*, 137(656), pp. 553–597. doi: 10.1002/qj.828.

Draper, C. and Mills, G. (2008) 'The Atmospheric Water Balance over the Semiarid Murray-Darling River Basin', *Journal of Hydrometeorology*, 9(3), pp. 521–534, June 2008. doi: 10.1175/2007JHM889.1.

Eltahir, E. A. B. and Bras, R. L. (1996) 'Precipitation recycling', *Reviews of Geophysics*, 34, pp. 367–378.

Endris, H. S., Omondi, P., Jain, S., Lennard, C., Hewitson, B., Chang'a, L., Awange, J. L., Dosio, A., Ketiem, P., Nikulin, G., Panitz, H. J., Büchner, M., Stordal, F. and Tazalika, L. (2013) 'Assessment of the performance of CORDEX regional climate models in simulating East African rainfall', *Journal of Climate*, 26(21), pp. 8453–8475. doi: 10.1175/JCLI-D-12-00708.1.

Fersch, B. (2011) 'Large scale water balance estimation from downscaled atmospheric moisture budgets and evaluation with global climatological data sets and the GRACE spaceborne gravimetry' *PhD thesis*. University of Augsburg.

Findell, K. L. and Eltahir, E. A. B. (2003) 'Atmospheric Controls on Soil Moisture–

Boundary Layer Interactions. Part I: Framework Development', *Journal of Hydrometeorology*, 4(3), pp. 552–569. doi: 10.1175/1525-7541(2003)004<0552:ACOSML>2.0.CO;2.

Friedl, M. ., McIver, D. ., Hodges, J. C. ., Zhang, X. ., Muchoney, D., Strahler, A. ., Woodcock, C. ., Gopal, S., Schneider, A., Cooper, A., Baccini, A., Gao, F. and Schaaf, C. (2002) 'Global land cover mapping from MODIS: algorithms and early results', *Remote Sensing of Environment*, 83(1–2), pp. 287–302. doi: 10.1016/S0034-4257(02)00078-0.

Ge, J., Qi, J., Lofgren, B. M., Moore, N., Torbick, N. and Olson, J. M. (2007) 'Impacts of land use/cover classification accuracy on regional climate simulations', *Journal of Geophysical Research Atmospheres*, 112(5), pp. 1–12. doi: 10.1029/2006JD007404.

Givati, A., Gochis, D., Rummier, T. and Kunstmann, H. (2016) 'Comparing One-Way and Two-Way Coupled Hydrometeorological Forecasting Systems for Flood Forecasting in the Mediterranean Region', *Hydrology*, 3(2), p. 19. doi: 10.3390/hydrology3020019.

Gochis, D. and Chen, F. (2003) 'Hydrological Enhancements to the Community Noah Land Surface Model', *NCAR Scientific Technical Report*, p. 77. doi: 10.1017/CBO9781107415324.004.

Gochis, D., Yu, W. and Yates, D. (2015) 'The WRF-Hydro model technical description and User's guide, version 3.0. NCAR Technical Document. 120 pages', (May). Available at: http://www.ral.ucar.edu/projects/wrf_hydro/.

Grell, G. A. and Freitas, S. R. (2014) 'A scale and aerosol aware stochastic convective parameterization for weather and air quality modeling', *Atmospheric Chemistry and Physics*, 14(10), pp. 5233–5250. doi: 10.5194/acp-14-5233-2014.

Hong, S.-Y., Noh, Y. and Dudhia, J. (2006) 'A new vertical diffusion package with an explicit treatment of entrainment processes.', *Monthly Weather Review*, 134(9), pp. 2318–2341. doi: 10.1175/MWR3199.1.

Huffman, G. J., Bolvin, D. T., Nelkin, E. J., Wolff, D. B., Adler, R. F., Gu, G., Hong, Y., Bowman, K. P. and Stocker, E. F. (2007) 'The TRMM Multisatellite Precipitation Analysis (TMPA): Quasi-Global, Multiyear, Combined-Sensor Precipitation Estimates at

Fine Scales', *Journal of Hydrometeorology*, 8(1), pp. 38–55. doi: 10.1175/JHM560.1.

Indeje, M., Semazzi, F. H. M. and Ogallo, L. J. (2000) 'Enso Signals in East African Rainfall Seasons', 46, pp. 19–46.

Janjic, Z., Emanuel, K. and M., Z.-R. (2000) 'Comments on "Development and Evaluation of a Convection Scheme for Use in Climate Models"', *Journal of the Atmospheric Sciences*, 57(21), pp. 3686–3686. doi: 10.1175/1520-0469(2000)057<3686:CODAEO>2.0.CO;2.

Janjić, Z. I. (1994) 'The Step-Mountain Eta Coordinate Model: Further Developments of the Convection, Viscous Sublayer, and Turbulence Closure Schemes', *Monthly Weather Review*, pp. 927–945. doi: 10.1175/1520-0493(1994)122<0927:TSMECM>2.0.CO;2.

Julien, P. Y., Saghafian, B. and Ogden, F. L. (1995) 'Raster-Based Hydrologic Modeling of Spatially-Variied Surface Runoff', 31(3), pp. 523–536. doi: 10.1111/j.1752-1688.1995.tb04039.x.

Jury, M., Rautenbach, H., Tadross, M. and Philipp, A. (2007) 'Evaluating spatial scales of climate variability in sub-Saharan Africa', 177, pp. 169–177. doi: 10.1007/s00704-006-0251-7.

Kain, J. S. (2004) 'The Kain–Fritsch Convective Parameterization: An Update', *Journal of Applied Meteorology*, 43(1), pp. 170–181. doi: 10.1175/1520-0450(2004)043<0170:TKCPAU>2.0.CO;2.

Kerandi, N. M., Arnault, J., Laux, P., Wagner, S., Kitheka, J., and Kunstmann, H. (2017) 'Joint atmospheric-terrestrial water balances for East Africa: A WRF-Hydro case study for the upper Tana River basin', *Theoretical and Applied Climatology*, doi: 10.1007/s00704-017-2058-8.

Kerandi, N. M., Laux, P., Arnault, J. and Kunstmann, H. (2016) 'Performance of the WRF model to simulate the seasonal and interannual variability of hydrometeorological variables in East Africa: a case study for the Tana River basin in Kenya', *Theoretical and Applied Climatology*, doi: 10.1007/s00704-016-1890-y.

Kitheka, J. U., Obiero, M. and Nthenge, P. (2005) 'River discharge, sediment transport and exchange in the Tana Estuary, Kenya', *Estuarine, Coastal and Shelf Science*,

63(3), pp. 455–468. doi: 10.1016/j.ecss.2004.11.011.

Knoop, L., Sambalino, F. and Steenbergen, F. V. (2012) Securing water and land in the Tana basin: *a resource book for water managers and practitioners*.

Koster, R. D., Dirmeyer, P. A., Guo, Z., Bonan, G., Chan, E., Cox, P., Gordon, C. T., Kanae, S., Kowalczyk, E., Lawrence, D., Liu, P., Lu, C.-H., Malyshev, S., McAvaney, B., Mitchell, K., Mocko, D., Oki, T., Oleson, K., Pitman, A., Sud, Y. C., Taylor, C. M., Verseghy, D., Vasic, R., Xue, Y. and Yamada, T. (2004) 'Regions of Strong Coupling Between Soil Moisture and Precipitation', *Science*, 305(5687), pp. 1138–1140. doi: 10.1126/science.1100217.

Kunstmann, H. and Jung, G. (2007) 'Influence of soil-moisture and land use change on precipitation in the Volta Basin of West Africa', *International Journal of River Basin Management*, 5(1), pp. 9–16. doi: 10.1080/15715124.2007.9635301.

Kunstmann, H. and Stadler, C. (2005) 'High resolution distributed atmospheric-hydrological modelling for Alpine catchments', *Journal of Hydrology*, 314(1–4), pp. 105–124. doi: 10.1016/j.jhydrol.2005.03.033.

Liang, X.-Z., Choi, H. I., Kunkel, K. E., Dai, Y., Joseph, E., Wang, J. X. L. and Kumar, P. (2005) 'Surface Boundary Conditions for Mesoscale Regional Climate Models', *Earth Interactions*, 9(18), pp. 1–28. doi: 10.1175/EI151.1.

Lin, Y.-L., Farley, R. D. and Orville, H. D. (1983) 'Bulk Parameterization of the Snow Field in a Cloud Model', *Journal of Climate and Applied Meteorology*, pp. 1065–1092. doi: 10.1175/1520-0450(1983)022<1065:BPOTSF>2.0.CO;2.

Lutz, K., Jacobeit, J., Philipp, A., Seubert, S., Kunstmann, H. and Laux, P. (2012) 'Comparison and evaluation of statistical downscaling techniques for station-based precipitation in the Middle East', *International Journal of Climatology*, 32(10), pp. 1579–1595. doi: 10.1002/joc.2381.

Marengo, J. A. (2005) 'Characteristics and spatio-temporal variability of the Amazon river basin water budget', *Climate Dynamics*, 24(1), pp. 11–22. doi: 10.1007/s00382-004-0461-6.

Maxwell, R. M., Lundquist, J. K., Mirocha, J. D., Smith, S. G., Woodward, C. S. and Tompson, A. F. B. (2011) 'Development of a Coupled Groundwater–Atmosphere

Model', *Monthly Weather Review*, 139(2005), pp. 96–116. doi: 10.1175/2010MWR3392.1.

McSweeney, C., New, M., Lizcano, G. and Lu, X. (2010) 'The UNDP climate change country profiles', *Bulletin of the American Meteorological Society*, 91(2), pp. 157–166. doi: 10.1175/2009BAMS2826.1.

Miralles, D. G., Holmes, T. R. H., Jeu, R. A. M. De, Gash, J. H., Meesters, A. G. C. A. and Dolman, A. J. (2011) 'Global land-surface evaporation estimated from satellite-based observations', (2), pp. 453–469. doi: 10.5194/hess-15-453-2011.

Moriasi, D. N., Arnold, J. G., Van Liew, M. W., Binger, R. L., Harmel, R. D. and Veith, T. L. (2007) 'Model evaluation guidelines for systematic quantification of accuracy in watershed simulations', *Transactions of the ASABE*, 50(3), pp. 885–900. doi: 10.13031/2013.23153.

Music, B. and Caya, D. (2007) 'Evaluation of the Hydrological Cycle over the Mississippi River Basin as Simulated by the Canadian Regional Climate Model (CRCM)', *Journal of Hydrometeorology*, 8(5), pp. 969–988. doi: 10.1175/JHM627.1.

Nakaegawa, T. and Wachana, C. (2012) 'First impact assessment of hydrological cycle in the Tana River Basin, Kenya, under a changing climate in the late 21st Century', *Hydrological Research Letters*, 6, pp. 29–34. doi: 10.3178/hrl.6.29.

Nicholson, S. E. (1996) 'A review of climate dynamics and climate variability in Eastern Africa.', in Johnson, T. C. and Odada, E. O. (eds) *The limnology, climatology and paleoclimatology of East African lakes*. Amsterdam, p. 665.

Nicholson, S. E. (2014) 'The predictability of rainfall over the Greater Horn of Africa. Part I. Prediction of seasonal rainfall.', *Journal of Hydrometeorology*, p. 140117143344004. doi: 10.1175/JHM-D-13-062.1.

Ogalo, L. J. (1988) 'Relationships between seasonal rainfall in East Africa and the Southern Oscillation', *Journal of Climatology*, 8(1), pp. 31–43. doi: 10.1002/joc.3370080104.

Oki, T., Musiak, K., Matsuyama, H. and Masuda, K. (1995) 'Global atmospheric water balance and runoff from large river basins', *Hydrological Processes*, 9(January 1994), pp. 655–678. doi: 10.1002/hyp.3360090513.

Oludhe, C., Sankarasubramanian, A., Sinha, T., Devineni, N. and Lall, U. (2013) 'The role of multimodel climate forecasts in improving water and energy management over the tana river basin, Kenya', *Journal of Applied Meteorology and Climatology*, 52(11), pp. 2460–2475. doi: 10.1175/JAMC-D-12-0300.1.

Peixoto, J. P. and Oort, A. H. (1992) *Physics of Climate*. New York: American Institute of Physics.

Pleim, J. E. (2007) 'A combined local and nonlocal closure model for the atmospheric boundary layer. Part I: Model description and testing', *Journal of Applied Meteorology and Climatology*, 46(9), pp. 1383–1395. doi: 10.1175/JAM2539.1.

Pohl, B., Crétat, J. and Camberlin, P. (2011) 'Testing WRF capability in simulating the atmospheric water cycle over Equatorial East Africa', *Climate Dynamics*, 37(7–8), pp. 1357–1379. doi: 10.1007/s00382-011-1024-2.

Riddle, E. E. and Cook, K. H. (2008) 'Abrupt rainfall transitions over the Greater Horn of Africa: Observations and regional model simulations', *Journal of Geophysical Research Atmospheres*, 113(15), pp. 1–14. doi: 10.1029/2007JD009202.

Roberts, J. and Snelgrove, K. (2015) 'Atmospheric and Terrestrial Water Balances of Labrador's Churchill River Basin, as Simulated by the North American Regional Climate Change Assessment Program', *Atmosphere-Ocean*, 53(3), pp. 304–318. doi: 10.1080/07055900.2015.1029870.

Rosero, E., Yang, Z.-L., Gulden, L. E., Niu, G.-Y. and Gochis, D. J. (2009) 'Evaluating Enhanced Hydrological Representations in Noah LSM over Transition Zones: Implications for Model Development', *Journal of Hydrometeorology*, 10(3), pp. 600–622. doi: 10.1175/2009JHM1029.1.

Schär, C., Lüthi, D., Beyerle, U. and Heise, E. (1999) 'The soil-precipitation feedback: A process study with a regional climate model', *Journal of Climate*, 12(2–3), pp. 722–741. doi: 10.1175/1520-0442(1999)012<0722:TSPFAP>2.0.CO;2.

Schreck, C. J. and Semazzi, F. H. M. (2004) 'Variability of the recent climate of eastern Africa', *International Journal of Climatology*, 24(6), pp. 681–701. doi: 10.1002/joc.1019.

Segele, Z. T., Leslie, L. M. and Lamb, P. J. (2009) 'Evaluation and adaptation of a regional climate model for the Horn of Africa: rainfall climatology and interannual

variability', *International Journal of Climatology*, 29, p. 47–65. doi: 10.1002/joc.1681.

Senatore, A., Mendicino, G., Gochis, D. J., Yu, W., Yates, D. N. and Kunstmann, H. (2015) 'Fully coupled atmosphere-hydrology simulations for the central Mediterranean: Impact of enhanced hydrological parameterization for short and long time scales', *Journal of Advances in Modeling Earth Systems*, pp. 1–23. doi: 10.1002/2015MS000510.

Senevitne, S. I., Viterbo, P., Lüthi, D. and Schär, C. (2004) 'Inferring Changes in Terrestrial Water Storage Using ERA-40 Reanalysis Data: The Mississippi River Basin', *Journal of Climate*, 17, pp. 2039–2057.

Shelton, M. L. (2009) *Hydroclimatology: Perspectives and applications*. University of California, Davis: Cambridge University Press.

Skamarock, W. C., Klemp, J. B., Dudhi, J., Gill, D. O., Barker, D. M., Duda, M. G., Huang, X.-Y., Wang, W. and Powers, J. G. (2008) 'A Description of the Advanced Research WRF Version 3', *Technical Report*, (June), p. 113. doi: 10.5065/D6DZ069T.

Small, E. E., Giorgi, F. and Sloan, L. C. (1999) 'Regional climate model simulation of precipitation in central Asia: Mean and interannual variability', *Journal of Geophysical Research*, 104(D6), p. 6563. doi: 10.1029/98JD02501.

Song, Y., Semazzi, F. H. M., Xie, L. and Ogallo, L. J. (2004) 'A coupled regional climate model for the Lake Victoria Basin of East Africa', *International Journal of Climatology*, 24(1), pp. 57–75. doi: 10.1002/joc.983.

Song, Y., Semazzi, F. and Xie, L. (2002) Development of a coupled regional climate simulation model for the Lake Victoria Basin, The East African Great Lakes: *Limnology, Palaeolimnology and Biodiversity*. Edited by E. Odada and G. Olago. Gordon and Breach.

Stensrud, D. J. (2007) 'Parameterization Schemes: Keys to Understanding Numerical Weather Prediction Models', (May), p. 480. doi: 10.1017/CBO9780511812590.

Sun, L., Semazzi, F. H. M., Giorgi, F. and Ogallo, L. (1999) 'Application of the NCAR regional climate model to eastern Africa: 1. Simulation of the short rains of 1988', *Journal of Geophysical Research*, 104(6), pp. 6529 - 6548. doi: 10.1029/1998JD200051.

Trenberth, K. E. (1999) 'Atmospheric moisture recycling: Role of advection and local evaporation', *Journal of Climate*, 12(5 II), pp. 1368–1381. doi: 10.1175/1520-0442(1999)012<1368:AMRROA>2.0.CO;2.

Vera, C., Gutowski, W., Mechoso, C. R., Goswami, B. N., Reason, C. C., Thorncroft, C. D., Marengo, J. A., Hewitson, B., Hendon, H., Jones, C. and Lionello, P. (2013) 'Climate Science for Serving Society: Research, Modeling and Prediction Priorities', in Asrar, R. G. and Hurrell, W. J. (eds). Dordrecht: Springer Netherlands, pp. 273–306. doi: 10.1007/978-94-007-6692-1_11.

Wagner, S., Fersch, B., Yuan, F., Yu, Z. and Kunstmann, H. (2016) 'Fully coupled atmospheric-hydrological modeling at regional and long-term scales: Development, application, and analysis of WRF-HMS', *Water Resources Research*, 52, pp. 1–20. doi: 10.1002/2015WR018185.

Warner, T. T. (2011) *Numerical Weather and Climate Prediction*. doi: 10.1017/CBO9780511763243.

Wei, J., Su, H. and Yang, Z. L. (2016) 'Impact of moisture flux convergence and soil moisture on precipitation: a case study for the southern United States with implications for the globe', *Climate Dynamics*. Springer Berlin Heidelberg, 46(1–2), pp. 467–481. doi: 10.1007/s00382-015-2593-2.

Yeh, P. J. F. and Famiglietti, J. S. (2008) 'Regional terrestrial water storage change and evapotranspiration from terrestrial and atmospheric water balance computations', *Journal of Geophysical Research Atmospheres*, 113(9), pp. 1–13. doi: 10.1029/2007JD009045.

Yucel, I., Onen, A., Yilmaz, K. K. and Gochis, D. J. (2015) 'Calibration and evaluation of a flood forecasting system: Utility of numerical weather prediction model, data assimilation and satellite-based rainfall', *Journal of Hydrology*. Elsevier B.V., 523, pp. 49–66. doi: 10.1016/j.jhydrol.2015.01.042.

Zabel, F. and Mauser, W. (2013) '2-way coupling the hydrological land surface model PROMET with the regional climate model MM5', *Hydrology and Earth System Sciences*, 17(5), pp. 1705–1714. doi: 10.5194/hess-17-1705-2013.

Appendix A: Meteorological forcing data

The following file shows an example of forcing data *netcdf* file header showing the variables, the variable formats and exact units of each that are used to drive the Noah LSM for the uncoupled WRF-Hydro. The global attributes of the file are also shown. For instance this file header shows that the simulation year is 2012, the simulation month is February (02), the simulation date is 22nd and the simulation hour is 06 hours.

```
netcdf \2012022206 {
dimensions:
    Time = UNLIMITED ; // (1 currently)
    south_north = 120 ;
    west_east = 120 ;
variables:
    float LWDOWN(Time, south_north, west_east) ;
        LWDOWN:units = "W m-2" ;
        LWDOWN:FieldType = 104 ;
        LWDOWN:MemoryOrder = "XY " ;
        LWDOWN:description = "DOWNWARD LONG WAVE FLUX AT
        GROUND SURFACE" ;
        LWDOWN:stagger = "" ;
    float PSFC(Time, south_north, west_east) ;
        PSFC:units = "Pa" ;
        PSFC:FieldType = 104 ;
        PSFC:MemoryOrder = "XY " ;
        PSFC:description = "SFC PRESSURE" ;
        PSFC:stagger = "" ;
    float Q2D(Time, south_north, west_east) ;
        Q2D:units = "kg kg-1" ;
        Q2D:FieldType = 104 ;
        Q2D:MemoryOrder = "XY " ;
        Q2D:description = "QV at 2 M" ;
        Q2D:stagger = "" ;
    float RAINRATE(Time, south_north, west_east) ;
        RAINRATE:long_name = "precipitation (mm)" ;
        RAINRATE:_FillValue = -9999.9f ;
        RAINRATE:comments = "Unknown1 variable comment" ;
        RAINRATE:grid_name = "grid-1" ;
        RAINRATE:level_description = "Earth surface" ;
        RAINRATE:time_statistic = "instantaneous" ;
    float SWDOWN(Time, south_north, west_east) ;
        SWDOWN:units = "W m-2" ;
        SWDOWN:FieldType = 104 ;
        SWDOWN:MemoryOrder = "XY " ;
        SWDOWN:description = "DOWNWARD SHORT WAVE FLUX AT
        GROUND SURFACE" ;
        SWDOWN:stagger = "" ;
    float T2D(Time, south_north, west_east) ;
        T2D:units = "K" ;
        T2D:FieldType = 104 ;
```

```
T2D:MemoryOrder = "XY " ;
T2D:description = "TEMP at 2 M" ;
T2D:stagger = "" ;
float U2D(Time, south_north, west_east) ;
U2D:units = "m s-1" ;
U2D:FieldType = 104 ;
U2D:MemoryOrder = "XY " ;
U2D:description = "U at 10 M" ;
U2D:stagger = "" ;
float V2D(Time, south_north, west_east) ;
V2D:units = "m s-1" ;
V2D:FieldType = 104 ;
V2D:MemoryOrder = "XY " ;
V2D:description = "V at 10 M" ;
V2D:stagger = "" ;

// global attributes:
:CDI = "Climate Data Interface version 1.5.4
      (http://code.zmaw.de/projects/cdi)" ;
:Conventions = "CF-1.4" ;
:TITLE = " OUTPUT FROM WRF V3.5.1 MODEL " ;
:START_DATE = "2012-01-01_00:00:00" ;
:SIMULATION_START_DATE = "2012-01-01_00:00:00" ;
:WEST-EAST_GRID_DIMENSION = 121 ;
:SOUTH-NORTH_GRID_DIMENSION = 121 ;
:BOTTOM-TOP_GRID_DIMENSION = 40 ;
:DX = 5000.f ;
:DY = 5000.f ;
:STOCH_FORCE_OPT = 0 ;
:GRIDTYPE = "C" ;
:DIFF_OPT = 1 ;
:KM_OPT = 4 ;
:DAMP_OPT = 3 ;
:DAMPCOEF = 0.2f ;
:KHDIF = 0.f ;
:KVDIF = 0.f ;
:MP_PHYSICS = 6 ;
:RA_LW_PHYSICS = 5 ;
:RA_SW_PHYSICS = 5 ;
:SF_SFCLAY_PHYSICS = 1 ;
:SF_SURFACE_PHYSICS = 2 ;
:BL_PBL_PHYSICS = 7 ;
:CU_PHYSICS = 1 ;
:SURFACE_INPUT_SOURCE = 1 ;
:SST_UPDATE = 1 ;
:GRID_FDDA = 0 ;
:GFDDA_INTERVAL_M = 0 ;
:GFDDA_END_H = 0 ;
:GRID_SFDDA = 0 ;
:SGFDDA_INTERVAL_M = 0 ;
:SGFDDA_END_H = 0 ;
:HYPSONOMETRIC_OPT = 2 ;
:SF_URBAN_PHYSICS = 0 ;
```

```
:SHCU_PHYSICS = 0 ;
:MFSHCONV = 0 ;
:FEEDBACK = 1 ;
:SMOOTH_OPTION = 0 ;
:SWRAD_SCAT = 1.f ;
:W_DAMPING = 0 ;
:DT = 20.f ;
:RADT = 10.f ;
:BLDT = 0.f ;
:CUDT = 5.f ;
:SWINT_OPT = 0 ;
:MOIST_ADV_OPT = 1 ;
:SCALAR_ADV_OPT = 1 ;
:TKE_ADV_OPT = 1 ;
:DIFF_6TH_OPT = 0 ;
:DIFF_6TH_FACTOR = 0.12f ;
:OBS_NUDGE_OPT = 0 ;
:BUCKET_MM = -1.f ;
:BUCKET_J = -1.f ;
:PREC_ACC_DT = 0.f ;
:SF_OCEAN_PHYSICS = 0 ;
:ISFTCFLX = 0 ;
:ISHALLOW = 0 ;
:DFI_OPT = 0 ;
:WEST-EAST_PATCH_START_UNSTAG = 1 ;
:WEST-EAST_PATCH_END_UNSTAG = 120 ;
:WEST-EAST_PATCH_START_STAG = 1 ;
:WEST-EAST_PATCH_END_STAG = 121 ;
:SOUTH-NORTH_PATCH_START_UNSTAG = 1 ;
:SOUTH-NORTH_PATCH_END_UNSTAG = 120 ;
:SOUTH-NORTH_PATCH_START_STAG = 1 ;
:SOUTH-NORTH_PATCH_END_STAG = 121 ;
:BOTTOM-TOP_PATCH_START_UNSTAG = 1 ;
:BOTTOM-TOP_PATCH_END_UNSTAG = 39 ;
:BOTTOM-TOP_PATCH_START_STAG = 1 ;
:BOTTOM-TOP_PATCH_END_STAG = 40 ;
:GRID_ID = 2 ;
:PARENT_ID = 1 ;
:I_PARENT_START = 56 ;
:J_PARENT_START = 45 ;
:PARENT_GRID_RATIO = 5 ;
:CEN_LAT = -0.3870544f ;
:CEN_LON = 37.23782f ;
:TRUELAT1 = 0.4f ;
:TRUELAT2 = 0.4f ;
:MOAD_CEN_LAT = 0.3999939f ;
:STAND_LON = 37.8f ;
:POLE_LAT = 90.f ;
:POLE_LON = 0.f ;
:GMT = 0.f ;
:JULYR = 2012 ;
:JULDAY = 1 ;
:MAP_PROJ = 3 ;
```

```
:MAP_PROJ_CHAR = "Mercator" ;  
:MMINLU = "MODIFIED_IGBP_MODIS_NOAH" ;  
:NUM_LAND_CAT = 20 ;  
:ISWATER = 17 ;  
:ISLAKE = -1 ;  
:ISICE = 15 ;  
:ISURBAN = 13 ;  
:ISOILWATER = 14 ;  
:NCO = "4.0.5" ;  
:CDO = "Climate Data Operators version 1.5.4  
      (http://code.zmaw.de/projects/cdo)" ;
```

Appendix B: Statement of the objective criteria and other statistical measures

An illustration of the objective criteria or the statistical measures made use of in this PhD study is presented here.

RMSE-observations standard deviation ratio (RSR)

This is calculated as the ratio of the RMSE and standard deviation of observations as shown in the following equation (Moriasi *et al.*, 2007)

$$RSR = \frac{RMSE}{STDEV_{obs}} = \frac{\sqrt{\sum_{i=1}^n (Y_i^{obs} - Y_i^{sim})^2}}{\sqrt{\sum_{i=1}^n (Y_i^{obs} - Y^{mean})^2}} \quad B-1$$

Where Y_i^{obs} is the i th observation for the constituent being evaluated, Y_i^{sim} is the i th simulated value for the constituent being evaluated, Y^{mean} is the mean of observed data of the constituent being evaluated, and n is the total number of observations.

A value of 0 indicates a perfect model simulation. Large positive values indicate poor model performance. Lower RSR means lower RMSE indicates a better model simulation performance

Nash-Sutcliffe efficiency (NSE)

The Nash-Sutcliffe efficiency (NSE) (Nash and Sutcliffe, 1970) is calculated as:

$$NSE = 1 - \frac{\sum_{i=1}^n (Y_i^{obs} - Y_i^{sim})^2}{\sum_{i=1}^n (Y_i^{obs} - Y^{mean})^2} \quad B-2$$

NSE ranges between $-\infty$ and 1.0 (1 shows a perfect fit). Values between 0.0 and 1.0 are generally viewed as acceptable levels of performance, whereas values ≤ 0.0 indicate that the mean of observed time series is a better predictor than the simulated time series and this is an unacceptable performance.

Percent bias (PBIAS)

The Percent bias (PBIAS) gives the average tendency of the simulated data to be larger or smaller than their observed counterparts (Gupta, Sorooshian and Yapo, 1999) is defined to as:

$$PBIAS = \left[\frac{\sum_{i=1}^n (Y_i^{sim} - Y_i^{obs}) * (100)}{\sum_{i=1}^n (Y_i^{obs})} \right] \quad B-3$$

Its optimal value is 0.0, with low-magnitude values indicating accurate model simulations. Positive values indicate model overestimation bias while negative values indicate model underestimation (Gupta, Sorooshian and Yapo, 1999).

Skill score (SS)

The skill score is similar to NSE in that the closer to one the better the model prediction. It interprets model predictability using residual error and observed variability in the data. Skill score equal or less than zero means that the model error is larger than the variability in the data.

$$SS = 1 - \frac{RMSE}{STDEV_{obs}} = 1 - \frac{\left[\sqrt{\sum_{i=1}^n (Y_i^{obs} - Y_i^{sim})^2} \right]}{\left[\sqrt{\sum_{i=1}^n (Y_i^{obs} - Y_{mean})^2} \right]} \quad B-4$$

Coefficient of variation (CV)

It is defined to as:

$$CV = \frac{RMSE}{mean} \times 100 \% = \frac{\left[\sqrt{\sum_{i=1}^n (Y_i^{obs} - Y_i^{sim})^2} \right]}{Y_{mean}} \times 100 \% \quad B-5$$

The CV of a model aims to describe the model fit in terms of the relative sizes of the squared residues and outcome values. The lower the CV, the smaller the residues is relative to the predicted value. This is suggestive of a good model fit.

It is noted that the RMSE of two models both measure the magnitude of the residues, but cannot be compared to each other in a meaningful way to determine which model

provides better prediction of an outcome. The model RMSE and the mean of the predicted variable are expressed in same units; their ratio cancels out the units.

The *CV* and coefficient of determination, *R-squared* are indicative of a model fit, but define model fit in two different ways. *CV* evaluates the relative closeness of the predictions to the actual values while *R-squared* evaluates how much of the variability in the actual values is explained by the model.

Appendix C: Computation of the water balance components

A brief highlight on the processing of the simulated water balance components is presented in this section. We focus on the change in atmospheric water storage or precipitable water in the atmosphere dW/dt , the vertically integrated water vapor flux C , evapotranspiration ET and precipitation P .

The model output results are computed for the rectangular boundaries of the model domain. In this dissertation the defined boundaries lies between $0^{\circ}10'$ and $0^{\circ}48'S$ and $36^{\circ}36'$ and $37^{\circ}18'E$ and encompasses the Mathioya- Sagana subcatchment (MSS).

The following constants hold true for the computations of various variables accordingly:

Latent heat of vaporization $L_{v(water)} \approx 2.501 \times 10^6 J/kg$

Gravitational constant $g \approx 9 m/s$

Ideal gas constant for dry air $R_d \approx 287.4 \frac{J}{kg/K}$

Ideal gas constant for water vapor $R_v \approx 461.6 \frac{J}{kg/K}$

Heat capacity of dry air at constant pressure $C_p \approx 1004.4 \frac{J}{kg/K}$

Density of water $\rho_{water} \approx 1000 kg/m^3$

Accumulated precipitation P

The accumulated precipitation is computed from the sum of the accumulated total cumulus and total grid scale precipitation which are spatially averaged over the target domain circumscribing MSS. Daily sums are aggregated to monthly sums. All values determined are in millimeters (mm).

Accumulated evapotranspiration ET

The quantity of water vapour transpiring from area A during time Δt per unit of surface area ΔA can be defined as Δq_v measured in kg/m^2 .

The quantity of liquid water evaporating from or at the surface, $\Delta \theta$ per unit time Δt can be expressed in mm/s . However ,

$$\Delta q_v = \rho_{water} \times \Delta\theta / 1000 \left(\frac{kg}{m^3} \times m \right) = \Delta\theta \text{ kg/m}^2 \quad \text{C-1}$$

This shows numerically $\Delta q_v = \Delta\theta$

The latent heat of water evaporation per unit surface area ΔLH is given as:

$$\Delta LH = L_{v(water)} \times \Delta q_v \left(\frac{J}{kg} \times \frac{kg}{m^2} \right) \quad \text{C-2}$$

ΔLH is equivalent to the accumulated upward latent heat flux at the surface, ACLHF, and is measured in J/m^2 .

$$\begin{aligned} \text{It can be seen that } \Delta\theta &= \frac{1000}{\rho_{water}} \Delta q_v \\ &= \frac{1000}{\rho_{water}} \times \frac{\Delta LH}{L_{v(water)}} = \frac{1000}{\rho_{water}} \times \frac{ACLHF}{L_{v(water)}} \end{aligned}$$

Therefore,

$$\Delta\theta = \frac{ACLHF}{L_{v(water)}} \text{ in millimeters (mm)} \quad \text{C-3}$$

This is the evapotranspiration in millimeters (mm)

NB: kg/m^2 is equivalent to mm because $\rho_{water} = 1000 \text{ kg/m}^3$.

Vertically integrated water vapor flux C

Peixoto and Oort (1992) define the amount of water vapor in a unit area column of air within the earth's surface p_s and the top of the atmosphere p_t as its limits as:

$$W = \int_{p_s}^{p_t} q \frac{dp}{g} \quad \text{C-4}$$

W (kg/m² or mm) is the precipitable water in the atmosphere i.e., amount of liquid water that would result if all the water vapor in the atmosphere were condensed, q is the specific humidity (g/g), p is the pressure (Pa).

Integrating the horizontal transport of water vapor with respect to pressure give the vertically integrated vapor flux \vec{Q} (kg/m/s),

$$\vec{Q} = \int_{p_s}^{p_t} q \vec{V} \frac{dp}{g} = Q_u \vec{i} + Q_v \vec{j} \quad \text{C-5}$$

The meridional Q_v (north-south) and zonal Q_u (east-west) components of \vec{Q} are:

$$Q_u = - \int_{p_s}^{p_t} q \vec{u} \frac{dp}{g}; \quad Q_v = - \int_{p_s}^{p_t} q \vec{v} \frac{dp}{g} \quad \text{C-6}$$

Where \vec{u} and \vec{v} are the zonal and meridional wind velocity (in m/s) respectively.

$-\nabla \cdot \vec{Q}$ is the convergence (or negative divergence) of the vertical integral of horizontal moisture flux (in kg/m²/s or mm/s) which is the mean convergence of lateral atmospheric vapor flux of the inflow and outflow of water vapor flux of the domain.